Vibrational Entropy Differences in Materials

Thesis by
Laura Jeanne Nagel

In Partial Fulfillment of the Requirements
for the Degree of
Doctor of Philosophy

California Institute of Technology
Pasadena, California

1997
(Submitted June 18, 1996)

To my husband, John

Acknowledgments

I would like to begin by acknowledging the love and support I have received from my family, both by blood and by marriage, without which I could never have made it this far.

Many of the experiments performed for this thesis would not have been possible (or at least would have been a lot more difficult!) without the kind assistance of others. Lawrence Anthony provided me with a working experimental apparatus for low-temperature calorimetry and was immensely helpful while I was learning how to use it. He also wrote the programs which I use for processing my calorimetry data. Lesley Preister and Irene Wong very capably performed much of the sample preparation and characterization, thus allowing me to devote my time to the experiments. Carol Garland graciously assisted Lesley, Irene, and me with polishing the samples for optical microscopy and microprobe analysis. Without my collaborators at Oak Ridge National Laboratory, Lee Robertson and Steve Spooner, the work with neutron scattering and diffraction would not have been possible. Lee was always incredibly cheerful, considering the fact that we usually ended up starting our experiments at 3 a.m. Dale Conner made compression testing both possible and enjoyable. Mark Walter and Karina Montilla assisted with the frustrating sound velocity measurements on Ni_3V.

I do not have words adequate to describe how much I have enjoyed working with my advisor, Professor Brent Fultz. I deeply value the supportive work environment present in the Fultz group and count myself very lucky to have joined this group and taken on my particular research

topic. I would like to thank past and present members of the Fultz group for their willingness to help me learn new techniques and discuss my research results. They include Tab Stephens, Liubo Hong, Lawrence Anthony, Channing Ahn, Chuck Witham, Adrian Hightower, Bob Bowman, B. V. Ratnakumar, Peter Bogdanoff and Heather Frase. I have also been very fortunate in my office-mates: first, Marissa LaMadrid, and for the past year, Heather Frase.

I would also like to give my warmest thanks to other members of the Materials Science department: Maggie Taylor, Richard Dandliker, and Ralf Busch, who have been wonderful allies in both the classroom and the laboratory. I would also like to acknowledge the financial support for my research from the Department of Energy.

Finally, I would like to thank my husband, John, who has been by my side all the way through graduate school. His love and support have made the whole thing worthwhile.

Abstract

An investigation has been made into the differences in vibrational entropy between two states of a material. These vibrational entropy differences have been measured experimentally by low-temperature calorimetry for several alloy systems. The results from the calorimetry experiments have been compared with phonon densities of states (DOS) for the two states of the material obtained from inelastic neutron scattering data. The systems which have been examined are Fe_3Al, Ni_3Al, Cu_3Au, Ni_3V, Co_3V, and nanophase Fe.

The difference in vibrational entropy between chemically disordered and $D0_3$-ordered Fe_3Al was measured by calorimetry to be (0.10 ± 0.03) k_B/atom at high temperatures, with the ordered alloy having the lower vibrational entropy. Analysis of the vibrational modes of the ordered and disordered alloys with a Born-von Kármán model showed that the lower vibrational entropy of the ordered alloy originates from high-frequency optical modes involving large-amplitude vibrations of the aluminum-rich sublattice.

Inelastic neutron scattering measurements were performed on powdered Ni_3Al. The alloy was prepared in two states of chemical order: 1) with equilibrium $L1_2$ order, and 2) an fcc solid solution prepared by high-energy ball milling. The main difference in the phonon DOS of the ordered and disordered alloys occurs near 39 meV, the energy of a peak arising from optical modes in the ordered alloy. These high-frequency optical modes involve primarily the vibrations of the aluminum-rich sublattice. The difference in vibrational entropy of disordered and ordered Ni_3Al is $S_{vib}^{dis} - S_{vib}^{ord} = (+0.2 \pm 0.1)$ k_B/atom at high temperatures.

The difference in heat capacity of chemically disordered and $L1_2$-ordered Cu_3Au was measured by calorimetry from 70 K - 300 K. By comparing these measured results to a harmonic heat capacity calculated with a Born–von Kármán model, we estimate the difference in vibrational entropy between disordered and ordered Cu_3Au to be (0.14 ± 0.05) k_B/atom at high temperatures.

Samples of Ni_3V were prepared with two microstructures: 1) with equilibrium $D0_{22}$ order, and 2) with partial disorder (having a large $D0_{22}$ chemical order parameter, but without the tetragonality of the unit cell). We measured the difference in their heat capacities from 60 K to 325 K and inelastic neutron scattering spectra at four values of Q at 11 K and at 300 K. We describe a microstructural contribution to the anharmonic heat capacity that originates with the anisotropy of the $D0_{22}$ structure. We estimate the difference in vibrational entropy between partially-disordered and ordered Ni_3V to be $S^{pdis} - S^{ord} = (+0.037 \pm 0.015)$ k_B/atom at high temperature. The elastic energy stored in the microstructure is about 60 J/mole at low temperatures.

The difference in vibrational entropy between fcc disordered and hexagonal ordered Co_3V was measured by calorimetry to be (0.11 ± 0.03) k_B/atom at high temperatures, with the ordered alloy having the lower vibrational entropy. Neutron diffraction data revealed that the observed L12 region of the phase diagram does not exist, but is a state that can be obtained in quenched alloys.

Neutron energy loss spectra were measured for two states of nanophase Fe: 1) as-milled, with a characteristic nanocrystallite size of 12 nm, and 2) annealed, with a characteristic crystallite size of 28 nm. The longitudinal peak in the phonon DOS of the nanophase Fe was broadened compared to that of

the annealed material. We attribute this broadening to short phonon lifetimes in nanocrystals. The nanophase material also showed an enhanced density of states at low energies below 15 meV, which may indicate the presence of inter-crystallite vibrations. These differences in phonon DOS should have only a small effect on the difference in vibrational entropy of nanocrystalline and larger-grained Fe.

The vibrational entropy differences that have been measured are large enough in comparison to 0.56 k_B/atom, the maximum possible difference in configurational entropy for a 3:1 atomic ratio, to make a significant contribution to the alloy thermodynamics.

List of Publications

1. "Vibrational Entropy and Microstructural Effects on the Thermodynamics of Partially-disordered and Ordered Ni_3V," L. J. Nagel, B. Fultz, J. L. Robertson, S. Spooner, submitted for publication.

2. "Differences in Vibrational Entropy of Disordered and Ordered Cu_3Au," L. J. Nagel, L. Anthony, B. Fultz, Phil. Mag. Lett. **72**, 421 (1995).

3. "Phonon Densities of State and Vibrational Entropies of Ordered and Disordered Ni_3Al," B. Fultz, L. Anthony, L. J. Nagel, R. M. Nicklow, S. Spooner, Phys. Rev. B **52** 3315 (1995).

4. "Phonon Density of States of Nanocrystalline Fe Prepared by High Energy Ball Milling," B. Fultz, J. L. Robertson, T. A. Stephens, L. J. Nagel, S. Spooner, accepted for publication by J. Appl. Phys.

5. "Vibrational Entropy Differences in Intermetallic Compounds from Phonon Densities of States," L. Anthony, L. J. Nagel, B. Fultz, in Solid-Solid Phase Transformations, W. C. Johnson, J. Howe, D. E. Laughlin, and W. A. Soffa, eds. (TMS: Warrendale, PA, 1994), p. 467-472.

6. "The Magnitude and Origin of the Difference in Vibrational Entropy between Ordered and Disordered Fe_3Al," L. Anthony, L. J. Nagel, J. K. Okamoto, B. Fultz, Phys. Rev. Lett. **73**, 3034 (1994).

7. "An Experimental Study of the Difference in Vibrational Entropy between Ordered and Disordered Fe_3Al," L. J. Nagel, L. Anthony, J. K. Okamoto, B. Fultz, submitted for publication.

Contents

List of Figures

Chapter One Introduction

The purpose of my thesis work has been to examine the entropy change involved in phase transformations. An important and well-understood contribution to the entropy change is the "configurational entropy," which enumerates the number of ways that atoms can be arranged on the crystal lattice, given an overall state of order for the alloy [1-3]. Heat is evolved or absorbed as the atoms change their configuration on the lattice, because these configurational changes alter the chemical bonding in the alloy.

Heat can also be absorbed directly into the vibrational modes of the crystal, however, without moving the atoms between lattice sites. It seems reasonable that alloys in different (but constant) configurational states could differ in their "vibrational entropy." In spite of some general theoretical work [4-8], vibrational entropy has attracted little attention. Recently, however, the difference in vibrational entropy between ordered and disordered Ni_3Al was measured, and found to be about 0.3 k_B/atom [9]. This is of comparable magnitude to the maximum possible difference in configurational entropy for a 3:1 atomic ratio (0.56 k_B/atom), so vibrational entropy can be thermodynamically important in such transformations.

Vibrational entropy has also been studied in materials which undergo martensitic transformations [10]. Because the atomic configurations before and after a martensitic transformation are equivalent, there is no difference in configurational entropy between the two states. Thus, the difference in entropy for the transformation must be composed of the differences in vibrational and electronic entropy. Differences in vibrational entropy have also been measured in martensitic transformations in Cu-based shape-memory alloys, in which the energetically unfavorable bcc structure is stabilized by its large vibrational entropy [11]. As a continuation of the work by Anthony and Okamoto on Ni_3Al [9], I decided to examine the relative importance of vibrational entropy in several alloy systems in order to achieve a better understanding of the thermodynamics involved in a disorder-order transformation.

Although several of the components of my thesis work have been studied by others, the connection had not been made with the importance of vibrational entropy to transformations in materials. As early as 1924 Fritz Lange had measured carefully the difference in specific heat between the white and gray phases of tin [12]. This work was noted by F. Seitz in 1940 in his discussions of heat capacity in *The Modern Theory of Solids* [13]. One system whose lattice dynamics has received a great deal of attention is Cu_3Au. An electrical resistivity study by Bowen [14] in 1954 reported a large increase in Debye temperature, θ, from 175 K to 197 K upon ordering. With a Debye model, this can be converted into a difference in vibrational entropy at high temperatures as:

$$\Delta S_{vib} \equiv S^{dis} - S^{ord} \approx 3\, k_B \ln\left(\frac{\theta_{ord}}{\theta_{dis}}\right) , \qquad 1.1$$

from which we obtain a ΔS_{vib} of 0.355 k_B/atom. This large value of ΔS_{vib} is comparable to the entire entropy of the order-disorder transformation in Cu_3Au, which is about 0.40 k_B/atom [15]. After Bowen's result, however, Flinn, McManus and Rayne [16] performed careful measurements of elastic constants for ordered and disordered Cu_3Au, and obtained Debye temperatures of 283.8 K for the ordered alloy, and 281.6 K for the disordered alloy, so, with Equation 1.1, ΔS_{vib} would be a mere 0.023 k_B/atom. In 1957, Rayne [17] measured Debye temperatures for ordered and disordered Cu_3Au through calorimetry and found 285 K for the ordered alloy, and 278 K for the disordered alloy, so, with Equation 1.1, ΔS_{vib} would be 0.07 k_B/atom. Thus, results found in the literature for the vibrational entropy of Cu_3Au range from insignificant to overwhelming. Since Bowen's large difference in Debye temperatures was obtained by an indirect method of electrical resistivity (and since his data were of low quality), it seems that his results were discounted in further discussions of the thermodynamics of Cu_3Au.

1.1 Order-Disorder

Many materials with even-ratio stoichiometries undergo an ordering transition as they are cooled from high temperatures. As the atoms lose thermal energy, it becomes energetically favorable for them to rest on preferred sites instead of random sites. The degree to which this is true is quantified by the long-range order parameter, L, which is equal to one when an alloy is perfectly ordered, and zero when it is completely disordered. The mean field approximation for the free energy of an equiatomic binary A-B alloy can be extended to include vibrational entropy with the Einstein model [9]. Doing so requires different vibrational frequencies for A-A, B-B, and A-B pairs of atoms, denoted ω_{AA}, ω_{BB}, and ω_{AB}, and we must account for how an increase in the long-range order parameter causes the replacement of A-A and B-B pairs with A-B pairs. Minimizing the free energy with respect to the long-range order parameter provides the following relationship at high temperatures:

$$L = \frac{2k_BT}{z(V_{AA} + V_{BB} - 2V_{AB})} \ln\left[\frac{1+L}{1-L}\left(\frac{\omega_{AB}^2}{\omega_{AA}\omega_{BB}}\right)^{\frac{3}{2}}\right] \quad . \qquad 1.2$$

This is the well-known Bragg-Williams results, with the addition of a frequency factor. Here z is the lattice coordination number, and the chemical energy for preference of like pairs of atoms, $V_{AA} + V_{BB} - 2V_{AB}$, is positive for alloys that develop order. For an ordering alloy, we expect the A-B bonds to be stiffer than the A-A and B-B bonds (i.e., $\omega_{AB}^2 > \omega_{AA}\omega_{BB}$). Although it is reasonably easy to include a vibrational component in a model, until now there has been little experimental evidence to prove the importance of vibrational entropy in disorder-order transformations.

1.2 Thermodynamics

Having argued for the existence of differences in vibrational entropy between two states of order in a material, now how can it be measured? The first approach begins with the Debye model for heat capacity (presented in some detail in Section 2.2). Figure 1.1.a shows Debye heat capacity curves for two values of the Debye temperature, θ_D. By definition, we know that the vibrational entropy, S_{vib}, is given by

$$S_{vib}(T) = \int_0^T \frac{C_P}{T'} dT' \quad . \qquad 1.3$$

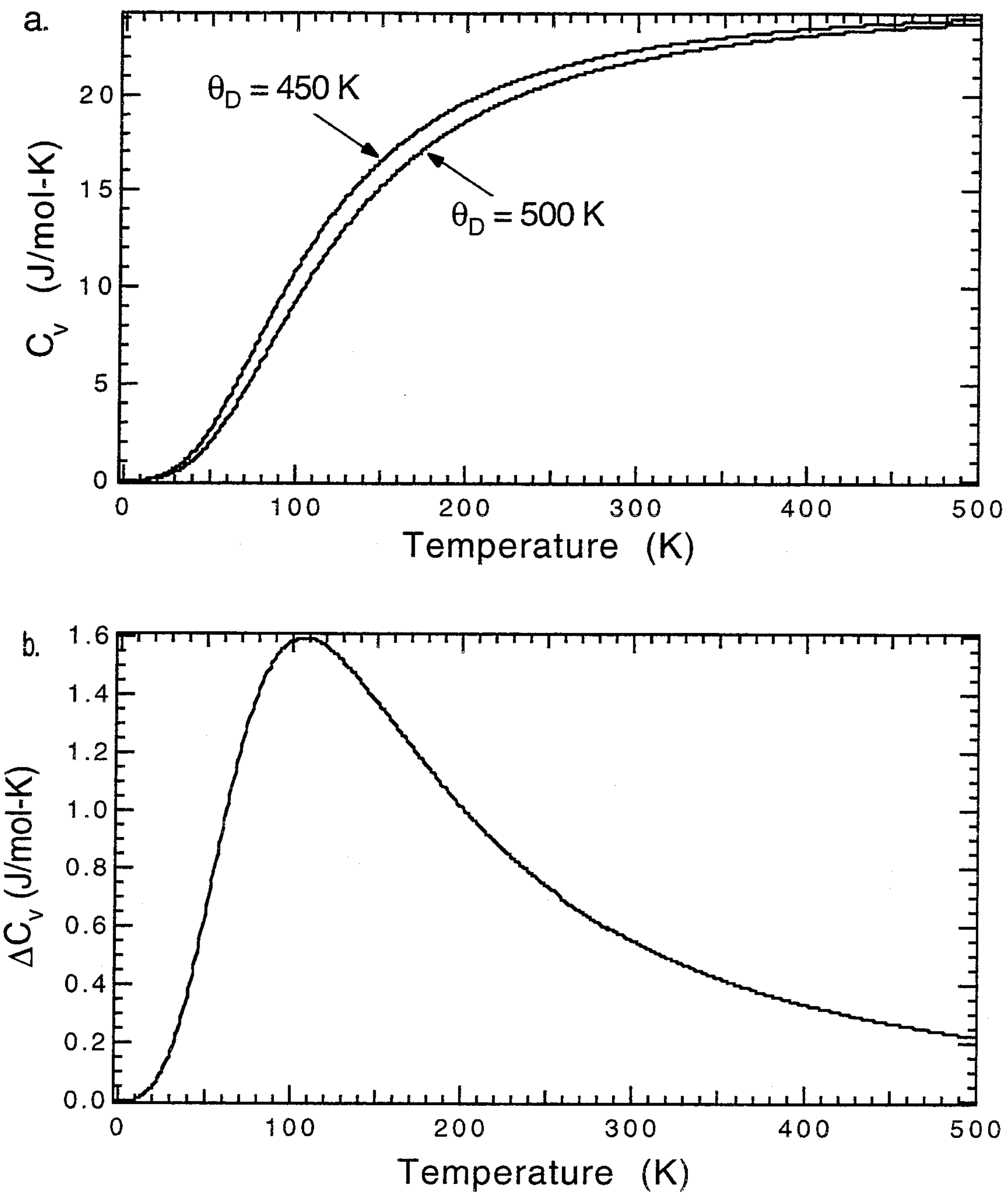

Figure 1.1 a. Two Debye heat capacities for $\theta_D = 450, 500$K. b. The difference in heat capacity between the two curves in a.

If we take the difference between the two Debye heat capacities, as shown in Figure 1.1.b, we can then obtain the difference in vibrational entropy from

$$\Delta S_{vib}(T) = \int_0^T \frac{\Delta C_P}{T'} dT' \quad . \qquad 1.4$$

Thus if we can accurately measure the difference in heat capacity between two states of the material, we can obtain the difference in vibrational entropy between the two states of the material. The experimental method is described in Section 3.3.1.

1.3 Density of States–Harmonic Model

Another approach to obtaining the difference in heat capacity between the two states of the material is to obtain the phonon densities of states (DOS) for both the ordered and disordered states of the material. The difference in the phonon density of states of the two materials, $g^D(\varepsilon) - g^O(\varepsilon)$, where ε is the phonon energy, is often the physical origin for differences in $\Delta C_p(T)$. For Fe_3Al and Cu_3Au, we employed a Born–von Kármán model to calculate the phonon densities of states (DOS) using force constants found in the literature [18-21]. Given the phonon DOS curves $g^D(\nu)$ and $g^O(\nu)$, the difference in lattice heat capacity was obtained from:

$$\Delta C_V(T) = 3Nk_B \int_0^\infty \left(g^D(\nu) - g^O(\nu)\right) \left(\frac{h\nu}{k_BT}\right)^2 \frac{\exp\left(\frac{h\nu}{k_BT}\right)}{\left(\exp\left(\frac{h\nu}{k_BT}\right) - 1\right)^2} d\nu \quad . \qquad 1.5$$

The phonon DOS of a material can sometimes be measured by inelastic neutron scattering. We have attempted to measure the phonon DOS for

Ni_3V and Co_3V by a more direct inelastic neutron scattering experiment, recording energy loss spectra at various values of momentum transfer, Q, to measure incoherent inelastic scattering and coherent inelastic scattering. The alloy Ni_3V proved convenient for this study, since the incoherent scattering cross sections of Ni and V are nearly identical, and the lattice dynamics of fcc Ni are well known.

1.4 Density of States–Anharmonic Model

We calculate the heat capacity at constant pressure, $C_p(T)$, as follows. The phonon energy in the lattice, E_{ph}, is:

$$E_{ph} = 3 \int_0^\infty g(\varepsilon)\,\varepsilon \left(\frac{1}{2} + \frac{1}{e^{\varepsilon/kT} - 1}\right) d\varepsilon \qquad . \qquad 1.6$$

The heat capacity at constant pressure, $C_p(T)$, depends on the temperature-dependence of E_{ph} through both the change in the phonon occupancy factor of each mode, and the change in the phonon DOS itself. At low temperatures:

$$C_p(T) = \left.\frac{\partial E_{ph}}{\partial T}\right)_p = 3 \int_0^\infty g_{T0}(\varepsilon) \frac{\varepsilon^2}{kT^2} \frac{e^{\varepsilon/kT}}{(e^{\varepsilon/kT} - 1)^2} d\varepsilon \qquad 1.7$$

$$+ 3 \int_0^\infty \frac{\partial g}{\partial T}\, \varepsilon \left(\frac{1}{2} + \frac{1}{e^{\varepsilon/kT} - 1}\right) d\varepsilon$$

where $g_{T0}(\varepsilon)$ is the phonon DOS at T = 0. We recognize the first term in Equation 1.7 (c.f. Equation 1.5) as $C_V(T)$, equal to $C_p(T)$ when the phonon DOS is unchanged with temperature so that $\frac{\partial g}{\partial T} = 0$. A problem for the analysis of our data is that we do not know $\frac{\partial g}{\partial T}$ over a broad range in temperature. One approach is to use the Grüneisen approximation for the temperature-dependence of $g(\varepsilon)$. Over a small temperature range the Grüneisen approximation provides:

$$\frac{\partial g}{\partial T} = 3\gamma\alpha\left[g(\varepsilon) + \frac{\partial g}{\partial \varepsilon}\varepsilon\right] \quad , \qquad 1.8$$

where γ is the Grüneisen constant and α is the linear coefficient of thermal expansion. Substituting Equation 1.8 into Equation 1.7 and integrating by parts, we obtain:

$$C_p(T) = C_V(T) + 3\gamma\alpha\left(\int_0^T C_V(T')dT' - \frac{1}{2}<\varepsilon>_{g_{T_0}}\right) , \qquad 1.9$$

where $C_V(T)$ is the heat capacity at constant volume:

$$C_V(T) = 3\int_0^\infty g_{T0}(\varepsilon)\frac{\varepsilon^2}{kT^2}\frac{e^{\varepsilon/kT}}{(e^{\varepsilon/kT}-1)^2}d\varepsilon \quad , \qquad 1.10$$

and where $<\varepsilon>_{g_{T_0}}$ in Equation 1.9 is the average energy of the phonon DOS (the first moment of $g_{T0}(\varepsilon)$). The last term in Equation 1.9 originates from the change in the zero point energy with changes in the phonon DOS. Apart from this last term, with $\gamma = \frac{3\,B\,V\,\alpha}{C_V}$ it is satisfying to show that Equation 1.9 is equivalent to the result from classical thermodynamics:

$$C_p(T) = C_V(T) + 9\,B\,V\,\alpha^2 T \quad , \qquad 1.11$$

where B is the bulk modulus and V is the specific volume.

References

[1] See, for example: F. Ducastelle, Order and Phase Stability in Alloys, (North Holland: Amsterdam, 1991).

[2] L. Onsager, Phys. Rev. **65**, 117 (1944).

[3] R. Kikuchi, Phys. Rev. **81**, 1988 (1951).

[4] C. Booth and J. S. Rowlinson, Trans. Faraday Soc. **51**, 463 (1955).

[5] P. J. Wojtowciz and J. G. Kirkwood, J. Chem. Phys. **33**, 1299 (1960).

[6] H. Bakker, Philos. Mag. A **45**, 213 (1982).

[7] J. A. D. Matthew, R. E. Jones, and V. M. Dwyer, J. Phys. F: Metal Phys. **13**, 581 (1983).

[8] H. Bakker and C. Tuijn, J. Phys. C **19**, 5585 (1986).

[9] L. Anthony, J. K. Okamoto, and B. Fultz, Phys. Rev. Lett. **70**, 1128 (1993).

[10] J. W. Cahn, Progress in Mat. Sci. **36**, 149 (1992).

[11] A. Planes, L. Mañosa, D. Ríos-Jara, and J. Ortín, Phys. Rev. B **45**, 45 (1992).

[12] F. Lange, Zeit. Phys. Chem. **110**, 343 (1924).

[13] F. Seitz, The Modern Theory of Solids, (McGraw-Hill: New York, 1940), p. 483.

[14] D. B. Bowen, Acta Met. **2**, 573 (1954).

[15] R. Hultgren, P. D. Desai, D. T. Hawkins, M. Gleiser, and K. K. Kelley, Selected Values of the Thermodynamic Properties of Binary Alloys, (ASM: Metals Park, Ohio, 1973), p. 258.

[16] P. A. Flinn, G. M. McManus, and J. A. Rayne, J. Phys. Chem. Solids **15**, 189 (1960).

[17] J. A. Rayne, Phys. Rev. **108**, 649 (1957).

[18] C. Van Dijk, Phys. Lett. A **34**, 255 (1970).

[19] I. M. Robertson, Solid State Commun. **53**, 901 (1985).

[20] I. M. Robertson, J. Phys.: Condens. Matter **3**, 8181 (1991).

[21] S. Katano, M. Iizumi, and Y. Noda, J. Phys. F: Met. Phys. **18**, 2195 (1988).

Chapter Two Theory of Vibrations in Solids

2.1 Introduction

An understanding of the theory of vibrations in solids is necessary to interpret the experimental data we have obtained from calorimetry and neutron scattering. The heat capacity results measured by low-temperature calorimetry can be understood in terms of the Debye model of a solid, while the Born-von Kármán model is a useful way to describe motions of atoms in a crystal as depicted by neutron scattering. These models enable us to visualize what is happening on both atomic and macroscopic levels in the material. We hope that, in turn, our experimental work will lead to a better understanding of lattice dynamics in real crystals.

2.2 Debye Model

This discussion of the Debye model is adapted from Kittel's *Introduction to Solid State Physics, Sixth Edition* [1]. In the Debye approximation the velocity of sound is taken as constant for each polarization type, as it would be for a classical elastic continuum. The dispersion relation is written as

$$\omega = vk \qquad 2.1$$

with v the constant velocity of sound. The density of states becomes

$$D(\omega) = \frac{Vk^2}{2\pi^2}\frac{dk}{d\omega} = \frac{V\omega^2}{2\pi^2 v^3} \ . \qquad 2.2$$

If there are N primitive cells in the specimen, the total number of acoustic phonon modes is N. A cutoff frequency ω_D is determined to be

$$\omega_D^3 = \frac{6\pi^2 v^3 N}{V} \qquad . \qquad 2.3$$

To this frequency there corresponds a cutoff wavevector in **k** space:

$$k_D = \frac{\omega_D}{v} = \left(\frac{6\pi^2 N}{V}\right)^{\frac{1}{3}} \qquad . \qquad 2.4$$

In the Debye model we do not allow modes of wavevector larger than k_D. The number of modes with $k \leq k_D$ exhausts the number of degrees of freedom of a monatomic lattice.

The thermal energy is the average of the vibrational energy, $\hbar\omega$, weighted by the density of states and the Bose-Einstein occupancy per state:

$$U = \int d\omega \ D(\omega) \langle n(\omega) \rangle h\omega \ = \int_0^{\omega_D} d\omega \left(\frac{V\omega^2}{2\pi^2 v^3}\right) \frac{\bar{h}\omega}{\exp\left(\frac{\bar{h}\omega}{k_B T}\right) - 1} \qquad , \qquad 2.5$$

for each polarization type. For brevity we assume that the phonon velocity is independent of the polarization, so that we may multiply by the factor 3 to obtain

$$U = \frac{3V\hbar}{2\pi^2 v^3}\int_0^{\omega_D} d\omega\left(\frac{\omega^3}{e^{\frac{\hbar\omega}{\tau}} - 1}\right) = \frac{3Vk_B^4T^4}{2\pi^2 v^3\hbar^3}\int_0^{x_D} dx\left(\frac{x^3}{e^x - 1}\right), \tag{2.6}$$

where $x = \frac{\hbar\omega}{\tau} = \frac{\hbar\omega}{k_BT}$ and $x_D = = \frac{\hbar\omega_D}{k_BT} = \frac{\theta_D}{T}$. This defines the Debye temperature θ_D in terms of ω_D defined by Equation 2.3. We may express θ_D as

$$\theta_D = \frac{\hbar v}{k_B}\left(\frac{6\pi^2 N}{V}\right)^{\frac{1}{3}} , \tag{2.7}$$

so that the total phonon energy is

$$U = 9Nk_BT\left(\frac{T}{\theta_D}\right)^3\int_0^{x_D}\frac{x^3dx}{e^x - 1} , \tag{2.8.}$$

where N is the number of atoms in the specimen. The heat capacity is found most easily by differentiating the middle expression of Equation 2.6 with respect to temperature. Then

$$C_v = 9Nk_B\left(\frac{T}{\theta_D}\right)^3\int_0^{x_D}\frac{x^4e^xdx}{(e^x - 1)^2} . \tag{2.9}$$

At very low temperatures we may approximate Equation 2.8 by letting the upper limit go to infinity. We have

$$\int_0^{\infty} \frac{x^3 dx}{e^x - 1} = \int_0^{\infty} dx\, x^3 \sum_{s=1}^{\infty} \exp(-sx) = 6 \sum_1^{\infty} \frac{1}{s^4} = \frac{\pi^4}{15} \quad , \qquad 2.10$$

where the sum is found in standard tables. Thus $U = \frac{3\pi^4 N k_B T^4}{5\theta_D^3}$ for $T << \theta_D$, and

$$C_v = \frac{12\pi^4}{5} N k_B \left(\frac{T}{\theta_D}\right)^3 \quad , \qquad 2.11$$

which is the Debye T^3 approximation.

2.3 Born-von Kármán Model

2.3.1 Adiabatic Approximation

The Born-von Kármán formalism is a convenient way to discuss how to analyze small amplitude motions of atoms in crystals. I will start by describing the crystal potential function, Φ, which describes the binding of atoms, as presented by Venkataraman in *Dynamics of Perfect Crystals* [2]. Born and Oppenheimer showed that describing dynamics using a potential function is possible providing the adiabatic approximation is made. Let the Hamiltonian of the crystal be given by:

$$H = \sum_i \frac{p_i^2}{2m_i} + \sum_j \frac{p_j^2}{2m_j} + V_1(R) + V_2(r) + V_3(r, R) \quad . \qquad 2.12$$

The first two terms represent the kinetic energies of the nuclei and of the electrons; $V_1(R)$ represents the potential energy of the nuclei, $V_2(r)$, that of the electrons, and $V_3(r, R)$, the energy of electron-nuclear interactions. The adiabatic approximations consists of assuming that the eigenfunction $\Psi(r, R)$ can be approximated by

$$\Psi_{n\lambda}(r, R) = \phi_{n\lambda}(R)\psi_n(r, R) . \qquad 2.13$$

$\psi_n(r, R)$ is the solution to the Schrödinger equation for the electronic system;

$$[\sum_j \frac{p_j^2}{2m} + V_2(r) + V_3(r, R)]\psi_n(r, R) = E_n(R)\psi_n(r, R) ; \qquad 2.14$$

$\phi_{n\lambda}(R)$ is an eigenfunction of the nuclear Hamiltonian and is obtained by solving the equation

$$[\sum_i \frac{p_i^2}{2m}+E_n(R)+V_1(R)]\phi_{n\lambda}(R)=[\sum_i \frac{p_i^2}{2m}+\Phi_n(R)]\phi_{n\lambda}(R)=E_n(R)\phi_{n\lambda}(R). \qquad 2.15$$

Effectively, the adiabatic approximation says that electronic and nuclear motions may be considered separately. There is an effective potential

$$\Phi_n(R) = E_n(R) + V_1(R) \qquad 2.16$$

which governs nuclear motions when the electronic system is in its *n*th state.

Under what conditions is it appropriate to use the adiabatic assumption? Venkataraman tells us that the answer is implicit in Equation 2.15, the spirit of which is that as the nuclei move the electronic system continually readjusts itself according to Equation 2.14 without changing its quantum number. In the process, the electronic system contributes an energy $E_n(R)$ to the crystal potential $\Phi_n(R)$. This is possible only when the nuclei move very slowly compared to the electrons so that the latter can make continuous readjustments so as to remain in the same (electronic) state [2]. In other words, for the approximation to hold, the frequencies of nuclear motion must be much smaller than the characteristic electronic transition frequencies. This is always the case for insulators because the electronic transition frequencies are high. This is not the case for metals; however, the approximation still holds because of the Pauli principle. Only a few electrons near the Fermi level can undergo real transitions; the adiabatic assumption is thus good for most of the electrons, making the concept of a Φ_0 function acceptable for metals also [2].

2.3.2 Equations of Nuclear Motion

The advantage of the adiabatic approximation is that once Φ_0 has been constructed, the restoring forces contributed by it to nuclear displacements can be expressed in mechanical terms. In this section, the formulation and solution of the equations of nuclear motion will be presented. We will assume that the crystal is perfect, infinite, free from stresses, and at 0 K; zero point effects will be ignored. Let n be the number of atoms in the primitive cell. We will define the equilibrium position of the kth atom in the lth cell by

$$\mathbf{x}\begin{pmatrix} l \\ k \end{pmatrix} = \mathbf{x}(l) + \mathbf{x}(k) \ , \qquad 2.17$$

where

$$\mathbf{x}(l) = l_1\mathbf{a}_1 + l_2\mathbf{a}_2 + l_3\mathbf{a}_3 \quad , \qquad 2.18$$

l_1, l_2, l_3 being integers, and $\mathbf{a}_1$, $\mathbf{a}_2$, $\mathbf{a}_3$ are the basis vectors of the crystal lattice. By convention these vectors are chosen to coincide with three edges of the primitive cell sharing a corner. Given the lattice, we may define a reciprocal lattice by

$$\mathbf{G}(h) = h_1\mathbf{b}_1 + h_2\mathbf{b}_2 + h_3\mathbf{b}_3 \qquad , \qquad 2.19$$

where h_1, h_2, h_3 are integers, and $\mathbf{b}_1$, $\mathbf{b}_2$, $\mathbf{b}_3$ are the basis vectors of the reciprocal lattice, related to $\mathbf{a}_1$, $\mathbf{a}_2$, $\mathbf{a}_3$ through

$$\mathbf{a}_i.\mathbf{b}_j = 2\pi\delta_{ij} \qquad , \qquad (i,j = 1, 2, 3); \qquad 2.20$$

where δ_{ij} is the Kronecker delta.

Now we will introduce a distortion to the crystal. The atom position can be described by

$$\mathbf{r}\begin{pmatrix} l \\ k \end{pmatrix} = \mathbf{x}\begin{pmatrix} l \\ k \end{pmatrix} + \mathbf{u}\begin{pmatrix} l \\ k \end{pmatrix} \quad , \qquad 2.21$$

where **u** denotes a small displacement. The kinetic energy is then given by

$$\mathrm{T} = \frac{1}{2} \sum_{l} \sum_{k} \sum_{\alpha} m_k \dot{u}_{\alpha}^{2} \binom{l}{k} \quad , \qquad 2.22$$

where m_k is the mass of the atom in the kth sublattice. The l summation is over all the primitive cells; k runs from 1 to n; α is the Cartesian component index.

We will assume that the electronic system is in its lowest state and will drop the electronic subscript on Φ_0. Since the displacements are assumed to be small, Φ may be expressed in a Taylor series as follows:

$$\Phi = \Phi^{(0)} + \Phi^{(1)} + \Phi^{(2)} + \Phi^{(3)} + \ldots, \qquad 2.23$$

where

$$\Phi^{(0)} = \Phi\left(\left\{\mathbf{x}\binom{l}{k}\right\}\right) , \qquad 2.24.a$$

$$\Phi^{(1)} = \sum_{lk\alpha} \frac{\partial \Phi}{\partial u_{\alpha}\binom{l}{k}}\Bigg|_{0} u_{\alpha}\binom{l}{k} = \sum_{lk\alpha} \phi_{\alpha}\binom{l}{k} u_{\alpha}\binom{l}{k} \quad , \qquad 2.24.b$$

$$\begin{aligned} \Phi^{(2)} &= \frac{1}{2} \sum_{lk\alpha} \sum_{l'k'\beta} \frac{\partial^2 \Phi}{\partial u_{\alpha}\binom{l}{k} \partial u_{\beta}\binom{l'}{k'}}\Bigg|_{0} u_{\alpha}\binom{l}{k} u_{\beta}\binom{l'}{k'} \\ &= \frac{1}{2} \sum_{lk\alpha} \sum_{l'k'\beta} \phi_{\alpha\beta}\begin{pmatrix} l & l' \\ k & k' \end{pmatrix} u_{\alpha}\binom{l}{k} u_{\beta}\binom{l'}{k'} , \qquad 2.24.c \end{aligned}$$

$$\Phi^{(3)} = \frac{1}{6}\sum_{lk\alpha}\sum_{l'k'\beta}\sum_{l''k''\gamma} \frac{\partial^3\Phi}{\partial u_\alpha\begin{pmatrix} l\\ k\end{pmatrix}\partial u_\beta\begin{pmatrix} l'\\ k'\end{pmatrix}\partial u_\gamma\begin{pmatrix} l''\\ k''\end{pmatrix}}\Bigg|_0 u_\alpha\begin{pmatrix} l\\ k\end{pmatrix} u_\beta\begin{pmatrix} l'\\ k'\end{pmatrix} u_\gamma\begin{pmatrix} l''\\ k''\end{pmatrix}$$

$$= \frac{1}{6}\sum_{lk\alpha}\sum_{l'k'\beta}\sum_{l''k''\gamma} \phi_{\alpha\beta\gamma}\begin{pmatrix} l & l' & l''\\ k & k' & k''\end{pmatrix} u_\alpha\begin{pmatrix} l\\ k\end{pmatrix} u_\beta\begin{pmatrix} l'\\ k'\end{pmatrix} u_\gamma\begin{pmatrix} l''\\ k''\end{pmatrix} \quad . \qquad 2.24.d$$

We will restrict the power series expansion to the second-order term. This is referred to as the harmonic approximation, which is meaningful only if the root-mean-squared displacements due to zero-point motion are small compared to interatomic distances. This is probably true for most solids.

In the equilibrium configuration, the force on every atom must vanish. This immediately leads to the result

$$\phi_\alpha\begin{pmatrix} l\\ k\end{pmatrix} = 0 \text{ for every } \alpha, k, l, \qquad 2.25$$

thus $\Phi^{(1)} = 0$. Thus in the harmonic approximation,

$$\Phi = \Phi^{(0)} + \Phi^{(2)}$$

$$\Phi = \Phi^{(0)} + \frac{1}{2}\sum_{lk\alpha}\sum_{l'k'\beta} \phi_{\alpha\beta}\begin{pmatrix} l & l'\\ k & k'\end{pmatrix} u_\alpha\begin{pmatrix} l\\ k\end{pmatrix} u_\beta\begin{pmatrix} l'\\ k'\end{pmatrix} \quad . \qquad 2.26$$

The coefficients $\phi_{\alpha\beta}\begin{pmatrix} l & l'\\ k & k'\end{pmatrix}$ may be interpreted as force constants.

The next step is to formulate the dynamical problem starting from the harmonic Hamiltonian

$$\mathrm{H} = \mathrm{T} + \Phi$$

$$\Phi = \sum_{\alpha} \frac{p_{\alpha}^{2}\begin{pmatrix} l \\ k \end{pmatrix}}{2m_k} \Phi^{(0)} + \frac{1}{2} \sum_{lk\alpha} \sum_{l'k'\beta} \phi_{\alpha\beta}\begin{pmatrix} l & l' \\ k & k' \end{pmatrix} u_{\alpha}\begin{pmatrix} l \\ k \end{pmatrix} u_{\beta}\begin{pmatrix} l' \\ k' \end{pmatrix} \quad , \qquad 2.27$$

where $p_{\alpha}\begin{pmatrix} l \\ k \end{pmatrix}$ is the momentum conjugate to $u_{\alpha}\begin{pmatrix} l \\ k \end{pmatrix}$. Using Hamilton's equations, we obtain directly from 2.27 the following equation of motion:

$$-\dot{p}_{\alpha}\begin{pmatrix} l \\ k \end{pmatrix} = -m_k \ddot{u}_{\alpha}\begin{pmatrix} l \\ k \end{pmatrix} = \sum_{l'k'\beta} \phi_{\alpha\beta}\begin{pmatrix} l & l' \\ k & k' \end{pmatrix} \quad , \qquad 2.28.$$

for $\alpha = x, y, z$; $k = 1,\ldots,n$; and l over the entire crystal. From 2.28 it is clear that $\phi_{\alpha\beta}\begin{pmatrix} l & l' \\ k & k' \end{pmatrix}$ is the negative of the force exerted on atom $\begin{pmatrix} l \\ k \end{pmatrix}$ in the α direction due to unit displacement of the atom $\begin{pmatrix} l' \\ k' \end{pmatrix}$ in the β direction. The quantity $-\Phi\alpha\beta$ is referred to as the force constant; it is traditionally symbolized by a spring obeying Hooke's law.

2.3.3 Solution of the Equations of Motion

Crystal periodicity suggests that the solutions must be such that the displacements of corresponding atoms in different cells be equivalent, apart from a possible phase factor. Accordingly we seek wavelike solutions of the type

$$u_\alpha\begin{pmatrix} l \\ k \end{pmatrix} = \frac{1}{\sqrt{m_k}} U_\alpha(k\,|\,\mathbf{q}) \exp\{i[\mathbf{q}\cdot\mathbf{x}(l) - \omega(\mathbf{q})t]\} \quad . \qquad 2.29$$

Here **q** is the wave vector and $\omega(\mathbf{q})$ the angular frequency associated with the wave. In trying a complex solution of the type 2.29, we understand that when all the independent solutions are superposed the displacements must be real [2].

Now if we substitute Equation 2.29 into the equations of motion, we obtain the following $3n$ simultaneous equations:

$$\omega^2(\mathbf{q}) U_\alpha(k\,|\,\mathbf{q}) = D_{\alpha\beta}\begin{pmatrix} \mathbf{q} \\ kk' \end{pmatrix} U_\beta(k'\,|\,\mathbf{q}) \quad , \qquad \alpha = \mathrm{x}, \mathrm{y}, \mathrm{z};\ k = 1,\ldots,n, \qquad 2.30$$

where

$$D_{\alpha\beta}\begin{pmatrix} \mathbf{q} \\ kk' \end{pmatrix} = \frac{1}{\sqrt{m_k m_{k'}}} \sum_{l'} \phi_{\alpha\beta}\begin{pmatrix} l & l' \\ k & k' \end{pmatrix} \exp\{i\mathbf{q}\cdot[\mathbf{x}(l') - \mathbf{x}(l)]\} \quad , \qquad 2.31$$

which can be expressed as

$$D_{\alpha\beta}\begin{pmatrix} \mathbf{q} \\ kk' \end{pmatrix} = \frac{1}{\sqrt{m_k m_{k'}}} \sum_{\bar{l}} \phi_{\alpha\beta}\begin{pmatrix} 0 & \bar{l} \\ k & k' \end{pmatrix} \exp\{i\mathbf{q}\cdot\mathbf{x}(\bar{l})\} \qquad 2.32$$

using crystal symmetry [2]. Equation 2.31 may be expressed in matrix notation as

$$\omega^2(\mathbf{q})\mathbf{U}(\mathbf{q}) = \mathbf{D}(\mathbf{q})\mathbf{U}(\mathbf{q}), \qquad 2.33$$

where $\mathbf{D}(\mathbf{q})$ is a $3n$-dimensional square matrix and $\mathbf{U}(\mathbf{q})$ is a $3n$-component column matrix:

$$\mathbf{D}(\mathbf{q}) = \begin{pmatrix} \mathbf{D}\begin{pmatrix} \mathbf{q} \\ 11 \end{pmatrix} & \cdots & \mathbf{D}\begin{pmatrix} \mathbf{q} \\ 1n \end{pmatrix} \\ \cdots & \cdots & \cdots \\ \mathbf{D}\begin{pmatrix} \mathbf{q} \\ n1 \end{pmatrix} & \cdots & \mathbf{D}\begin{pmatrix} \mathbf{q} \\ nn \end{pmatrix} \end{pmatrix}, \qquad 2.34.a$$

$$\mathbf{D}\begin{pmatrix} \mathbf{q} \\ kk' \end{pmatrix} = \begin{pmatrix} D_{xx}\begin{pmatrix} \mathbf{q} \\ kk' \end{pmatrix} & D_{xy}\begin{pmatrix} \mathbf{q} \\ kk' \end{pmatrix} & D_{xz}\begin{pmatrix} \mathbf{q} \\ kk' \end{pmatrix} \\ D_{yx}\begin{pmatrix} \mathbf{q} \\ kk' \end{pmatrix} & D_{yy}\begin{pmatrix} \mathbf{q} \\ kk' \end{pmatrix} & D_{yz}\begin{pmatrix} \mathbf{q} \\ kk' \end{pmatrix} \\ D_{zx}\begin{pmatrix} \mathbf{q} \\ kk' \end{pmatrix} & D_{zy}\begin{pmatrix} \mathbf{q} \\ kk' \end{pmatrix} & D_{zz}\begin{pmatrix} \mathbf{q} \\ kk' \end{pmatrix} \end{pmatrix}, \qquad 2.34.b$$

$$\mathbf{U}(\mathbf{q}) = \begin{pmatrix} U_x(k = 1 \mid \mathbf{q}) \\ U_y(k = 1 \mid \mathbf{q}) \\ \cdots \\ U_z(k = n \mid \mathbf{q}) \end{pmatrix} \qquad 2.34.c$$

$\mathbf{D}(\mathbf{q})$ is often termed the dynamical matrix. From Equation 2.33 it is clear that the problem of determining the frequencies appropriate to waves of wave vector **q** is essentially one of solving the eigenvalue problem. The eigenvalues are obtained by solving the characteristic equation

$$|| \mathbf{D}(\mathbf{q}) - \omega^2(\mathbf{q}) \mathbf{1}_{3n} || = 0 \qquad 2.35$$

which results when we insist that Equation 2.33 must yield nontrivial solutions for the wave amplitudes. Solving Equation 2.35 yields $3n$ eigenvalues which we label $\omega_j^2(\mathbf{q})$, ($j = 1, 2, \ldots, 3n$). Not all of these need be distinct; depending on the symmetry of the crystal and the value of **q**, some may be degenerate.

The dynamical matrix, $\mathbf{D}(\mathbf{q})$, (3 × 3 for the disordered state, 12 × 12 for the ordered state) was diagonalized for approximately 5 million different values of **k** for the disordered alloy, and approximately 10 million values for the ordered alloy in order to obtain the phonon densities of states, $g(\nu)$, for both the ordered and disordered alloys. The program (written by Lawrence Anthony) chooses a value of **q** and checks to see that this value falls within the first Brillouin zone. If it does, then the program diagonalizes $\mathbf{D}(\mathbf{q})$ and solves for its eigenvalues, thus creating the phonon density of states, $g(\nu)$. These DOS curves were then used to calculate heat capacities. Each normal mode was given a phonon occupation set by Bose-Einstein statistics. The heat capacity of the disordered and ordered materials is the heat capacity per mode integrated over the corresponding phonon DOS.

References

[1] C. Kittel, Introduction to Solid State Physics, Sixth Edition, (John Wiley & Sons: New York, 1986), Chapter 5.

[2] G. Venkataraman, L. A. Feldkamp, and V. C. Sahni, Dynamics of Perfect Crystals, (MIT Press: Cambridge, Mass., 1975), Chapter 2.

Chapter Three Sample Preparation and Experimental Methods

3.1 Methods of Sample Preparation

The materials I have studied during my thesis work have varied widely in composition and properties, and have thus required different methods of preparation and characterization. In this chapter, I will list and describe these methods; in the individual chapters, I will describe my sample materials and their particular methods of preparation and characterization.

3.1.1 Mechanical Alloying

Mechanical alloying is a technique commonly used to achieve a disordered and/or nanophase material. The system we used is a Spex 8000 mixer/mill. Elemental powders (or small chunks) of high purity are placed inside a hardened steel vial along with several stainless steel balls. The vial is then sealed in an inert atmosphere and placed inside the Spex 8000, which violently shakes the vial. Collisions between the balls and the walls of the vial crush the elemental powders, resulting in an alloy with small grain size. Typical ball-to-powder weight ratios range from 2:1 to 5:1. A solvent, such as hexane or ethanol, may be added to the vial to insure complete alloying.

3.1.2 Arc-melting

Arc-melting was used to produce ingots of approximately ten grams in mass. The samples are prepared by placing elemental pieces of metal in the desired mass ratio in an Edmund Bühler D-7400 chamber, in which a 3 psi over pressure of Ar is maintained. The Cu hearth is water cooled. A Ti getter is melted before the sample is melted in order to remove any oxygen from the chamber. The sample is then melted, inverted, and melted again to ensure homogeneity. This method produces a reasonably clean, homogenous button ingot without significant loss of mass during processing.

3.1.3 Induction Melting

Another method for melting elemental metal pieces to form an alloy is induction melting. The sample is placed in a water-cooled Ag or Cu boat, which is placed inside a Cu coil carrying a large radio-frequency current. Eddy currents are produced in the material and cause it to melt. A Ti getter is also used to clean the atmosphere, which can be evacuated or operated under an Ar over pressure. After melting, the sample can be inverted and melted again to ensure homogeneity. This method produces a reasonably clean, homogenous elongated ingot without significant loss of mass during processing.

3.1.4 Filing

The filing system (built by Mohit Jain [1]) consists of a wheel with a twelve inch file attached to the outside edge of the wheel. As the wheel turns, the file is pulled back and forth over the top of the sample, which is clamped in a vise. This action produces a powder from the solid ingot. This powder may be disordered by the filing process; however, some systems may require additional mechanical treatment in order to become fully disordered.

3.1.5 Thermal Treatment

Thermal treatments were used on all samples to obtain the desired state of order, grain size, or degree of homogenization. Samples were sealed in evacuated glass ampoules (quartz or Pyrex, depending on the temperature) and annealed in a Lindberg furnace. Disordered samples could be made ordered by annealing at a temperature below the ordering temperature for a long enough time to allow diffusion to move the atoms to their thermodynamically preferred orientations. Small ingots or chunks could be made disordered by quenching the samples from a temperature above the ordering temperature into iced brine, thus freezing in the disordered state. This method will work for systems which are relatively easy to disorder, such as Cu_3Au.

3.2 Sample Characterization

Once the samples were prepared, it was necessary to characterize their state of order, grain size, and chemical composition. This was done using the methods discussed below.

3.2.1 X-ray Diffraction

X-ray diffractometry was performed with an Inel CPS–120 diffractometer using Co Kα radiation. The wide angle position-sensitive detector used in this system is capable of providing very fast, accurate diffraction patterns, which provide information about the crystal structure, lattice parameter, and grain size of the material.

I used a computer program called Lazy Pulverix [2] to calculate theoretical x-ray and neutron powder diffraction patterns for some of my materials. The diffraction patterns are calculated using the lattice parameters, space-group symbol, and the coordinates and chemical symbols of the atoms in the unit cell. The calculation includes atom form factors, Lorentz-polarization factors, and geometrical features of a Bragg-Brentano powder diffractometer. The calculated diffraction pattern includes information on two-theta angle and relative peak intensities.

3.2.2 Quantitative Compositional Analysis

Chemical compositions and chemical homogeneities for some samples were measured with a JEOL Superprobe 733 electron microprobe. A Hewlett-Packard 5890 gas chromatograph equipped with a thermal conductivity detector was utilized in order to detect and quantify evolved hydrogen, oxygen, and nitrogen; these gases could affect both the calorimetry and neutron scattering results. Detectability limits with this system were 0.0032 wt.% for hydrogen, 0.078 wt.% for oxygen, and 0.22 wt.% for nitrogen.

3.3 Experimental Methods

3.3.1 Differential Scanning Calorimetry (DSC)

Low-temperature calorimetry was performed with a Perkin-Elmer DSC4 which had been modified by mounting the DSC4 head on an assembly which could be lowered into a liquid helium dewar. The control electronics and the software used with the regular DSC4 setup were not modified for these experiments. The DSC is a very sensitive type of calorimeter which operates by maintaining the same temperature in both samples pans and measuring the difference in heat flow necessary to maintain this temperature balance. Masses (from 40-300 mg) of the disordered and ordered alloys were matched to within 0.1 mg accuracy and placed in the two sample pans of the DSC4. To test reproducibility, we obtained several matched pairs of runs with liquid nitrogen as the cryogen for each set of samples; experiments were also performed with liquid helium as the cryogen. To counteract instrumental drift, runs comprised three pairs of scans over temperature intervals of 30 K, which typically overlapped by 10 K. Depending on the size and heat capacity of the samples, scan rates ranged from 5 to 40 K min^{-1}. Please see Appendix A for a detailed description of operational procedures.

The difference in vibrational entropy, $\Delta S_{vib} \equiv S^D - S^O$, between disordered (D) and ordered (O) samples was obtained from the measured difference in heat capacity at constant pressure, $\Delta C_p \equiv C_p^D - C_p^O$:

$$\Delta S_{vib}(T_1,T_2) = \int_{T_1}^{T_2} \frac{\Delta C_p}{T}\, dT \quad . \qquad 3.1$$

Ideally, $T_1 = 0$ K and T_2 is the temperature of interest, such as the critical temperature of the order-disorder transition. The range of our experimental data was from 80 K to 343 K. The upper limit of this range was chosen to suppress changes in the configurational entropy. Diffusional atom movements in most metals are negligible at these low temperatures. Were diffusion to occur, it would be largest at the highest temperatures of measurement, giving a strongly decreasing ΔC_p. Changes in the state of order could also modify the reproducibility of the three pairs of scans taken in each temperature interval, or the reproducibility of the different runs with the same samples. None of these problems were found, so we are confident that the measurements provided differences in the vibrational heat capacity, unencumbered by changes in the configurational entropy with its evolution of heat.

3.3.2 Neutron Scattering

Because neutrons interact with atomic nuclei in a material, rather than electron clouds, they provide information which may not be obtained by other methods, such as x-ray. Thermal neutrons have a wavelength distribution peaked around 1.6 Å, well-suited for studying variations in atomic density on a microscopic scale. Furthermore, thermal neutrons, by definition, have energies comparable to those of thermally induced fluctuations in solids (about 1/40 eV), making them the natural choice for studying the thermally important dynamics of solids by inelastic scattering. By contrast, x-rays or electrons with wavelengths around 1 Å have energies around 12 keV and 3.5 eV, respectively [3].

Also, neutrons can be advantageous for diffraction studies of the state of order of a material because of their ability to differentiate between atoms of similar masses. For example, x-rays are unable to distinguish between atoms with similar form factors such as Ni and V in Ni_3V; therefore, with x-ray diffraction you see only the fundamental diffractions and not the superlattice diffractions. However, because of the difference in neutron scattering cross-sections between Ni and V, very strong superlattice diffractions are observed with neutrons. This is also true for Co and V in Co_3V. Not only does the neutron scattering amplitude show no regular or rapid increase with atomic number, but it also shows no variation with the angle θ. The isotropic nature of the scattering is due to the fact that the dimensions of the nucleus, unlike those of the cloud of extranuclear electrons, are small in comparison with the wavelength of approximately 1 Å [4].

Yet another useful characteristic of neutrons is that they can penetrate thin layers of metal. Thus, samples may be enclosed in thin-walled sample holders (commonly aluminum or vanadium), and may also be placed inside special refrigerators or furnaces for in-situ measurements.

The important nuclear parameter for neutron diffraction is the "coherent scattering length," b [$\times 10^{-12}$ cm] [5]. The quantity $4\pi|b|^2$ is the direct equivalent of the form factor intensity $|f(\Delta\mathbf{k})|^2$ for x-ray scattering, and it is usually possible to predict neutron diffraction patterns from x-ray diffraction equations by simply substituting $4\pi|b|^2$ for $|f(\Delta\mathbf{k})|^2$. The neutron scattering form factor therefore has no significant dependence on Δk, and very high order diffractions can be measured at low temperatures. Debye-Waller factors will suppress higher order neutron diffraction peaks in the same way as for x-ray diffraction, however.

Neutrons are relatively heavy, at least compared to electrons, and have a low energy for a given momentum. A neutron with a 1 Å wavelength has an energy of about 0.082 eV, which is equivalent to a temperature of about 950 K. Debye temperatures of crystals are typically somewhat less than this, so neutrons with wavelengths appropriate for diffraction can interact strongly with crystal vibrations. Neutrons can gain and lose energy to the phonons in the crystal, and in doing so they will undergo a measurable change in their wavelength. Neutron inelastic scattering is the most important probe of phonons in a material, as described in section 3.3.2.1.

Neutron scattering is either elastic or inelastic, and coherent or incoherent. With x-rays and electrons, inelastic scattering is usually incoherent, by which we mean that the phase of the scattered wave is not predictably related to the phase of the incident wave. Such inelastic incoherent scattering is not useful for diffraction experiments. Neutron scattering can be both inelastic and coherent, however. If an individual phonon in the solid is considered as part of the scattering process, the neutron can lose (or gain) energy to the phonon, but the phase relationship between the incident and scattered neutron wave will be predictable.

Neutron scattering can also be elastic and incoherent at the same time. Elastic incoherent scattering may occur for a crystal of Ti, for example, for two reasons. First, the Ti contains a mixture of isotopes. The scattering process for each isotope is different, and the phase relationships for scattering between different isotopes are not easily predictable. Second, Ti contains some isotopes of having an atomic weight that is an odd number, and necessarily a nonzero nuclear spin. The scattering processes for different spin orientations of the same isotope are not the same. The coherence of scattering can be lost even when all atoms are of the same isotope, but the isotopes have different spin orientations.

3.3.2.1 Inelastic Neutron Scattering

In inelastic neutron scattering, "dynamical structure factors" have a utility that parallels the structure factors x-ray scattering (which are technically "coherent elastic structure factors") [5]. Dynamical structure factors involve sums over all atoms at the basis vectors $\{\mathbf{r}_k\}$ of the unit cell, weighted in by the scattering strengths of these atoms (σ_{inc} for incoherent scattering, and $4\pi b^2$ for coherent scattering, units are [barn$\equiv 10^{-24}$ cm^2]). However, the dynamical structure factor also includes a detailed consideration of how the neutron scattering event causes a transfer of momentum, **Q**, from the neutron to the crystal, and specifically how this **Q** couples to crystal vibrations. The momentum transfer is controlled experimentally by selecting the angles and energies of the incident and scattered neutron, and is predicted from Newtonian kinematics. Lattice dynamics are usually treated within a "Born - von Kármán model" (as described in Chapter Two), which places atom masses on springs connecting each atom to its various nearest neighbors. The vibrations in a crystal are solutions called "phonons." Each phonon is an independent wave that extends throughout the crystal, and is identified by a wavevector **q**, a frequency ν, and a "branch" γ, that refers to the type of phonon (e.g., acoustic, optical) and its polarization (e.g., longitudinal, transverse). Because the crystal has translational symmetry, each type of atom in the unit cell (at basis vector $\mathbf{r}_k$) will undergo the same vibrational motions as equivalent atoms in all other unit cells. Atom displacements at the different unit cells will occur at different times, however, and herein lies the difference between incoherent inelastic scattering and coherent elastic scattering. For incoherent inelastic scattering there is no consistent phase relationship between the scattering from an atom in one unit cell and an equivalent atom in another, and the relevant scattering cross section is σ_{inc} for incoherent scattering. For coherent inelastic scattering a phase relationship exists, and the strength of scattering depends on the coherent scattering length, b.

The dynamical structure factor for incoherent inelastic scattering is $G_{inc}(\nu,\mathbf{Q})$, which is measured at a particular energy loss, E=hν and momentum transfer, $\mathbf{Q}$. The amplitude of the scattering depends on the alignment between the momentum transfer, $\mathbf{Q}$, and the directions of motion or "polarization" of each atom in the unit cell. The polarization is described by a 3k-component vector, $\varepsilon^{\gamma}_{rk}(\mathbf{q})$, which has x-, y-, and z-components for each of the k atoms in the unit cell. This vector is given by $\varepsilon^{\gamma}_{rk}(\mathbf{q}) = u_x(\mathbf{r}_k \,|\, \mathbf{q})\hat{\mathbf{i}} + u_y(\mathbf{r}_k \,|\, \mathbf{q})\hat{\mathbf{j}} + u_z(\mathbf{r}_k \,|\, \mathbf{q})\hat{\mathbf{k}}$ in the notation of Equation 2.34.c. The dependence on alignment is the scalar product $\mathbf{Q}\cdot\varepsilon^{\gamma}_{rk}(\mathbf{q})$. The incoherent dynamical structure factor intensity is:

$$|G_{inc}(\nu,\mathbf{Q})|^2 = \sum_{rk} \frac{\sigma_{inc,rk}}{M_{rk}} \sum_{\gamma} \sum_{\mathbf{q}} |\mathbf{Q}\cdot\varepsilon^{\gamma}_{rk}(\mathbf{q})|^2 \, \delta(\nu - \nu_{\gamma}(\mathbf{q})) \, , \qquad 3.2$$

where the intensity is smaller for atoms with large mass, M_{rk}. The delta function assures the matching of energies of the phonon and the incident neutron; the crystal vibration cannot grow if there is a mismatch of frequencies of the neutron and phonon waves. Equation 3.2 can be evaluated for polycrystals. The crystallographic average of Equation 3.2 over the various orientations of **Q** is:

$$|G_{\mathrm{inc}}(\nu,Q)|^2 = Q^2 \sum_{rk} \frac{\sigma_{\mathrm{inc},rk}}{3M_{rk}} \sum_{\gamma} \sum_{\mathbf{q}} |\varepsilon_{rk}^{\gamma}(\mathbf{q})|^2 \, \delta(\nu - \nu_\gamma(\mathbf{q})) \ . \qquad 3.3$$

Equation 3.3 is closely related to the phonon density of states, $\rho(\nu)$ (included in Equation 3.3 as the distribution of the delta functions $\delta(\nu - \nu_\gamma(\mathbf{q}))$). It is sometimes possible to use incoherent inelastic neutron scattering to determine $\rho(\nu)$ for a material. In doing so, the measured data for neutron counts versus energy at a particular value of Q are first corrected for background, and then divided by the thermal phonon occupancy factor, $(n(\nu) - 1)/\nu$:

$$\frac{n(\nu)-1}{\nu} = \frac{1}{\nu\,[1-\exp(-h\nu/kT)]} \ , \qquad 3.4$$

which is related to the Bose-Einstein phonon occupancy factor. In ideal experiments, this corrected scattering spectrum will be the phonon density of states of the material. Unfortunately, three problems may vitiate the procedure. First, different species of atoms in the unit cell may have strongly different incoherent cross sections, σ_{inc}. In this case there will be much weaker scattering from phonons that emphasize motions of the atoms with small σ_{inc}. In general, correcting for this effect requires *a-priori* knowledge of the $\varepsilon_{rk}^{\gamma}(\mathbf{q})$, and hence the phonon DOS itself. Second, at high temperatures it may be possible for two phonons to be excited by one neutron. Double scattering can allow twice the energy loss of the neutron, and so will distort the measured energy loss spectrum. It is possible to correct for this multiphonon scattering in some cases, however, and multiphonon scattering is often negligible for small Q (< 5 Å^{-1}) at temperatures of 300 K and below. Third, there may be a significant contribution from coherent inelastic scattering that must be treated separately.

The dynamical structure factor for coherent inelastic scattering, $G_{coh}(\nu,\mathbf{Q})$, is:

$$G_{coh}(\nu,\mathbf{Q},\mathbf{q}) = \sum_{rk} \frac{1}{M_{rk}} \sum_{\gamma} \sum_{g} b_{rk}\, \mathbf{Q}\cdot\varepsilon_{rk}^{\gamma}(\mathbf{q})\, e^{i\mathbf{Q}\cdot\mathbf{r}k}\, \delta(\nu-\nu_{\gamma}(\mathbf{q}))\, \delta(\mathbf{Q}-\mathbf{q}-\mathbf{g}) \quad . \qquad 3.5$$

Notice the delta function in Equation 3.5 that does not appear in Equation 3.4. In addition to the requirement that the frequency of the phonon matches the frequency of the neutron, $\delta(\nu-\nu_{\gamma}(\mathbf{q}))$, coherent inelastic scattering also requires matching of the neutron and phonon wavevectors (modulo a reciprocal lattice vector), so there is the term $\delta(\mathbf{Q}-\mathbf{q}-\mathbf{g})$. The idea is that oscillations of the neutron wave must match the vibrational motions of all atoms along a phonon. This is a coherent scattering process, so the scattering amplitudes of the atoms and their motions must cooperate to scatter the neutron. The orientation of the momentum transfer along the vibrational direction of an atom is important (as in the previous case of incoherent scattering), hence the product $\mathbf{Q}\cdot\varepsilon_{rk}^{\gamma}(\mathbf{q})$. For coherent scattering it is also important that $\mathbf{Q}$ be in phase with atom motions over many unit cells. Hence the additional factor of $e^{i\mathbf{Q}\cdot\mathbf{r}k}$ in Equation 3.5.

Coherent inelastic scattering experiments are most effective when single crystals are available for study. The orientation of the crystalline axes with respect to **Q** gives control over the particular phonon, $\mathbf{q}_\gamma(\nu)$, that is excited. The frequency of the phonon can be measured by scanning the energy loss while maintaining a constant **Q**. Coherent inelastic scattering has been the most important method for measuring phonon dispersion curves, which are plots of $\mathbf{q}_\gamma(\nu)$ for the different branches, γ, of phonons in a crystalline solid. For polycrystalline solids, the coherent inelastic scattering is averaged over all orientations of the crystallites, and hence over all orientations of **q**. With a good understanding of the lattice dynamics of single crystals, it is possible to calculate the coherent inelastic scattering from polycrystals. Unfortunately, the inverse problem of going from coherent inelastic scattering data to phonon dispersion curves (or even to $g(\nu)$), is usually impossible.

3.3.2.2 Triple-axis Spectrometer

Figure 3.1 shows a schematic of the triple-axis spectrometer used in our experiments at the High-Flux Isotope Reactor (HFIR) at Oak Ridge National Laboratory (ORNL). From the collimated continuous neutron beam, a desired wavelength λ_0 is selected by a monochromator crystal by diffraction (angle $2\theta_M$). The sample can rotate around a vertical axis (angle Ψ) and the beam scattered by the angle Φ is analyzed by an analyzer crystal rotating around another vertical axis to seek neutrons of a wavelength satisfying the Bragg condition for a given Bragg reflection at a diffraction angle $2\theta_A$ [6]. A detector is placed at a corresponding angle to count these neutrons. As plane scattering geometry is used, we see that the instrument provides four variables ($2\theta_M$, Ψ, 2θ, $2\theta_A$) to satisfy three conditions imposed by the cross section expression. There are thus several ways to drive a triple-axis machine and to find phonons by appropriate scans in the scattering plane.

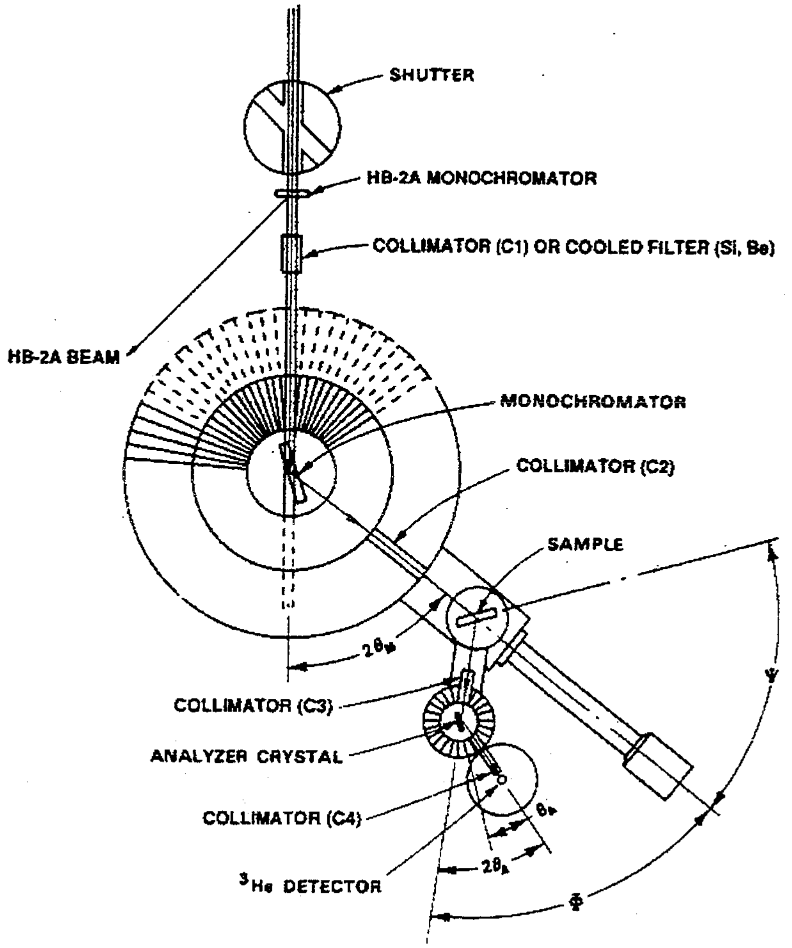

Figure 3.1 Schematic of the HB2 triple-axis spectrometer at the High Flux Isotope Reactor at Oak Ridge National Laboratory.

For our experiments, we operated the triple-axis spectrometer in fixed final energy and constant Q mode. The primary monochromator crystal angle, $2\theta_M$, was used to scan the incident energy, E_i, from 14.8 to 64.8 meV. The final energy, E_f, was maintained at 14.8 meV. The scattering angle, Φ, was driven to maintain constant Q for the chosen energy loss, E_i - E_f. Several filters were placed between the sample and the analyzer to remove $\lambda/2$ and $\lambda/3$ contamination from the neutron beam.

3.3.2.3 Neutron Diffraction

Neutron diffraction data were collected using the HB4 high-resolution powder diffractometer at the High-Flux Isotope Reactor at ORNL. This instrument has a Ge (115) monochromator which, when 2-theta = 87°, selects an incident neutron wavelength of 1.5 Å. The neutron wavelength was determined more precisely to be 1.4993(2) Å on the basis of unit cell refinements for the NIST Standard Reference Material Si 640b. Soller slit collimators of 12' and 20' are positioned before and after the monochromator crystal, respectively. An array of 32 equally spaced (2.7°) ^{3}He detectors, each with a 6' mylar foil collimator, can be step-scanned over a range of up to 40° for scattering angles between 11° and 135°.

The samples were placed in vanadium cans (9 mm inner diameter by 6 cm in length) for data collection at 295 K over the 2-theta range of 11° to 135° in steps of 0.05°. For these data collections, the detector array was scanned in two segments to overlap up to 8 detectors in the middle of the pattern. Overlapping detectors for a given step serves to average the counting efficiency and the 2-theta zero-point shift for each detector.

References

[1] Mohit Jain, Ph.D. thesis, Caltech, 1995.

[2] F. J. Rotella,*"User Manual for Rietveld Analysis of Time-of-Flight Neutron Powder Diffraction Data at IPNS,"* 1983. R. B. Von Dreele, J. D. Jorgensen, and C. G. Windsor, J. Appl. Crystallogr. **15**, 581 (1982).

[3] J. D. Axe and R. M. Nicklow, Phys. Today **38**, 27 (1985).

[4] G. E. Bacon, Neutron Diffraction, 2nd ed. (Clarendon Press: Oxford, 1962), Chapter 2.

[5] B. Fultz and J. Howe, Transmission Electron Microscopy and Diffractometry of Materials, to be submitted to McGraw-Hill: New York, Series in Pure and Applied Physics, 1996.

[6] G. Kostorz and S. W. Lovesey in Treatise on Materials Science and Technology Vol. 15 Neutron Scattering, G. Kostorz, ed. (Academic Press: New York, 1979) p. 52.

Chapter Four Fe$_3$Al

4.1 Introduction

The first system I chose to study was Fe$_3$Al. This material has a D0$_3$ ordered phase (see Figure 4.2) below 550°C; above this temperature, there is an fcc disordered solution, as is evident from the phase diagram for the Fe-Al system shown in Figure 4.1. James Okamoto studied the mean square relative displacements (MSRD) of the Fe and Al atoms in this alloy using an EXELFS technique [1]. I will include a discussion of how some of his results

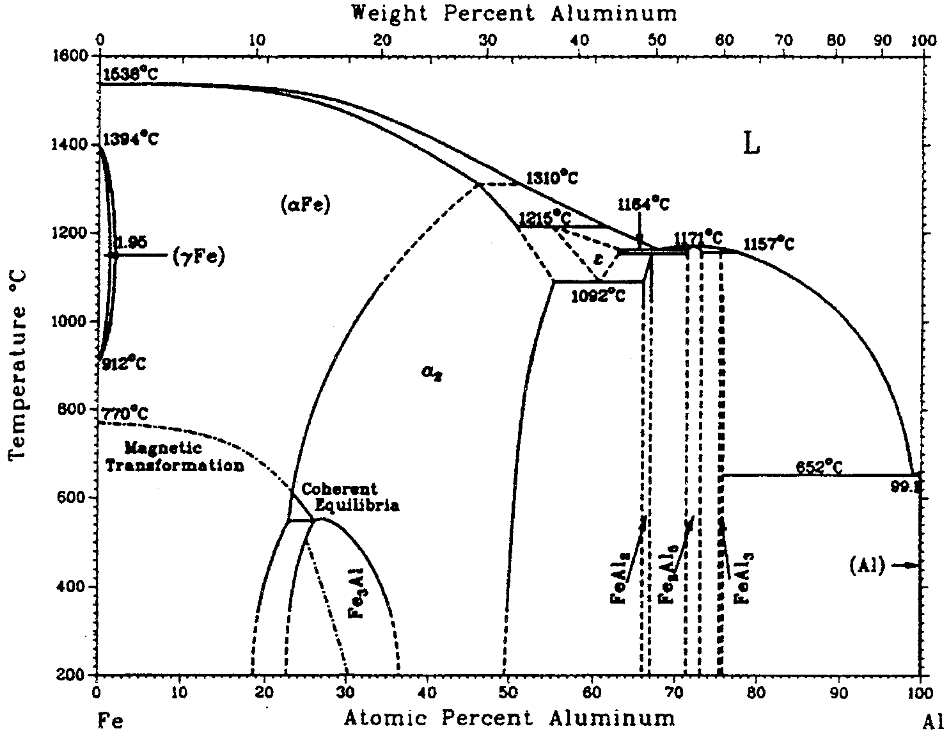

Figure 4.1 The phase diagram for the Fe-Al system. Taken from T. B. Massalski, editor-in-chief, Binary Alloy Phase Diagrams, 2nd ed. (Materials Park, Ohio: ASM International, 1990).

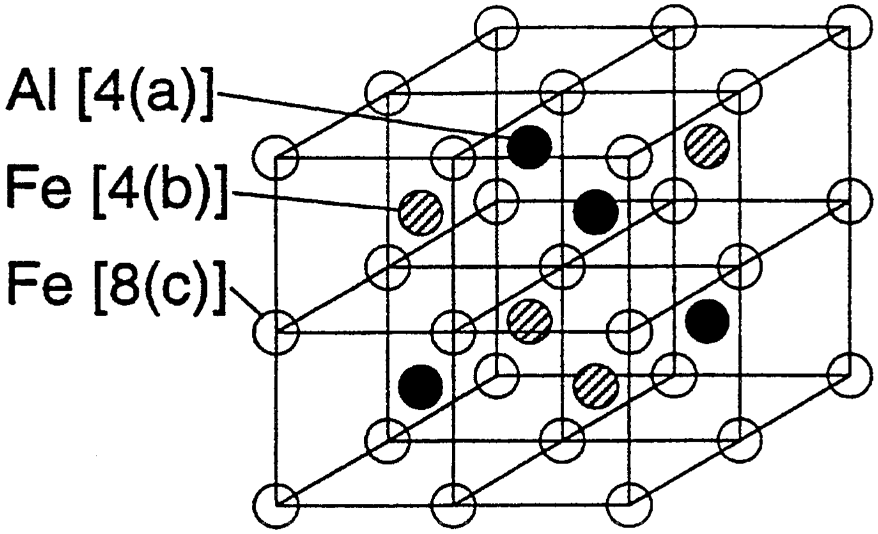

Figure 4.2 The D0$_3$ structure of Fe$_3$Al. Al atoms are black, the two different types of Fe atoms are gray and white.

relate to my work in this chapter. While the result I measured for the difference in vibrational entropy ((0.10 ± 0.03) k_B/atom) is not as large as was found by Lawrence Anthony for Ni$_3$Al, Fe$_3$Al offers an important advantage for understanding the origin of differences in vibrational entropy. Phonon dispersion relations from inelastic neutron scattering have been used to obtain Born-von Kármán force constants for both the ordered and disordered states of Fe$_3$Al [3-5]. From these force constants we obtained phonon densities of states (DOS), and used them to calculate the heat capacities and the vibrational entropies. We show that the smaller vibrational entropy of the ordered Fe$_3$Al is due largely to the development of high frequency optical modes involving the vibration of the aluminum-rich sublattice.

4.2 Sample Preparation

An alloy of Fe – 25 at.% Al was prepared from materials of 99.99% purity by arc-melting under an argon atmosphere. The composition and homogeneity of this same alloy had been characterized thoroughly in previous studies of chemical ordering transformations [6, 7]. For the present work, samples of disordered Fe_3Al were prepared by filing. X-ray powder diffractometry showed no superlattice diffractions from the as-filed powders. Mössbauer spectrometry, which is primarily sensitive to short-range order [8], showed that these filed powders were largely disordered solid solutions. A state of $D0_3$ chemical order was obtained in the samples by annealing them in evacuated borosilicate glass ampoules at 480 °C for 1 h. Strong x-ray superlattice diffractions were measured from the annealed powders, indicating a long-range order parameter of close to unity.

4.3 Experiment and Analysis

4.3.1 Calorimetry

I performed low-temperature heat capacity measurements using the system described in Section 3.3.1. Masses (about 40 mg) of the disordered and ordered alloys were matched to 10 μg accuracies and placed in the two sample pans of the DSC. Heat capacity measurements comprised pairs of runs, with the two samples interchanged in their sample pans between runs. The difference in heat capacities of the two samples was obtained from the difference of these two sets of runs. To test reproducibility, we obtained 5 matched pairs of runs with liquid nitrogen, and 2 matched pairs with liquid helium as the cryogen. To counteract instrumental drift, runs comprised three pairs of scans over small temperature intervals of 30 K, which typically overlapped by 10 K. Because of the relatively small masses of these samples, it was necessary to use a high scan rate, 40 K min^{-1}, in order to produce a good signal. Additional runs were performed with ordered Fe_3Al against a NIST sapphire calibration standard.

As was presented in Chapter Three, the difference in vibrational entropy can be obtained from the heat capacity data using the following equation:

$$\Delta S_{vib}(T_1,T_2) = \int_{T_1}^{T_2} \frac{\Delta C_p}{T} dT \quad . \tag{4.1}$$

Averaged results from the calorimetry measurements are presented in Figure 4.3. The sign of the data is positive, showing that the disordered state of Fe_3Al has the larger heat capacity. The data of Figure 4.3 were fit to a difference of two Debye functions with $\theta^{D}_{Debye} = 484$ K and $\theta^{O}_{Debye} = 500$ K to correct the integral of Equation 4.1 for the missing low and high temperature contributions. After correction, we obtain a difference in vibrational entropy, ΔS_{vib}, of (0.10 ± 0.03) k_B/atom at high temperatures. While smaller than the maximum possible configurational entropy of mixing (0.56 k_B/atom for the Fe_3Al stoichiometry), ΔS_{vib} is not negligible.

4.3.2 EXELFS

Local vibrational amplitudes of the Fe atoms and Al atoms with respect to their first-nearest neighbor atoms were measured with extended electron

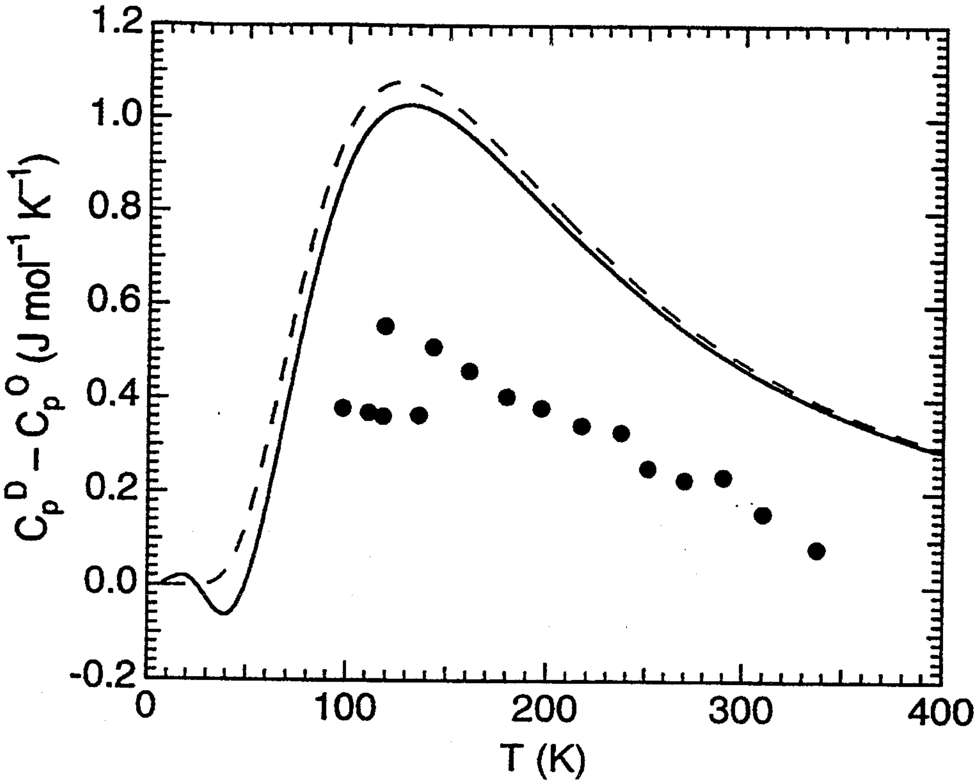

Figure 4.3 Points: measured differential heat capacity of ordered and disordered samples of Fe3Al, $\Delta C_P = C_P^D - C_P^O$, as a function of T. Curves were calculated using Equation 4.2, with the solid curve using the DOS from the main part of Figure 4.6, and the broken curve using the DOS from the inset.

energy loss fine structure spectrometry (EXELFS) [9, 10], performed at temperatures ranging from 100 K to 420 K. The Al K-edge and Fe $L_{2,3}$-edge electron energy-loss spectra were acquired with a Gatan 666 parallel-detection magnetic prism spectrometer attached to a Philips EM 430 transmission electron microscope. Processing of the spectra to obtain EXELFS oscillations and radial distribution functions (RDF's) followed procedures described elsewhere [2, 11, 12]. Figure 4.4 presents typical RDF's, uncorrected for phase shifts, from the Al K-edge EXELFS data from ordered Fe_3Al. The peak in the EXELFS data near 2 Å originates from interference from the first-nearest-neighbor (1nn) shell, and the inverse Fourier transform of this peak, selected by the window at the top of Figure 4.4, was used to obtain the Debye-Waller factor for the 1nn shell. All EXELFS experiments and data analysis were performed by James Okamoto and are described in his Ph.D. thesis and other publications [1, 2].

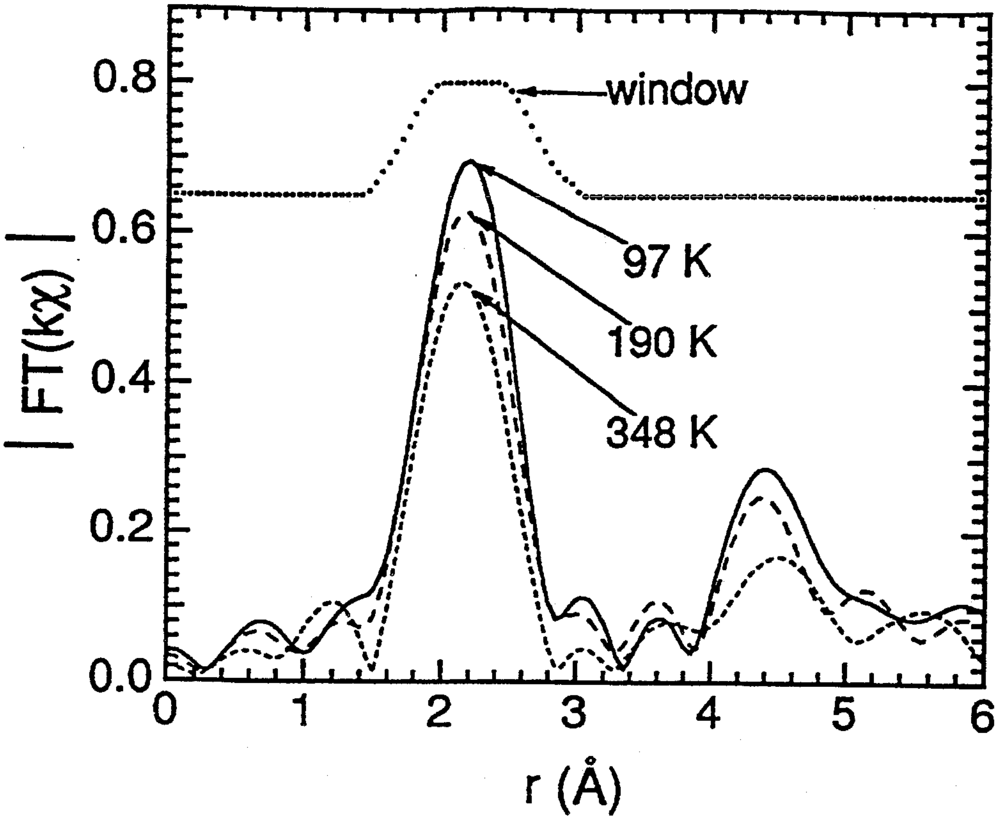

Figure 4.4 Fourier band-pass filtering of Al K-edge EXELFS data from ordered Fe3Al. Data in the range 5.0Å^{-1}<k<10.0Å^{-1} were Fourier transformed.

Analysis of the Al K-edge EXELFS was straightforward, but analysis of the Fe L_{23}-edge EXELFS was less so for several reasons [2, 9-12]. The L_1 edge jump overlaps with the L_{23} EXELFS signal. This problem is avoided by using only L_{23} EXELFS data beyond 6Å^{-1}, which is past the L_1 edge jump. (This choice also allows us to neglect the spin-orbit splitting of 13 eV between Fe L_3 and L_2 edges, because at energies well above the ionization threshold their EXELFS oscillations are virtually in phase [9].) We calculated differential electron scattering cross sections for the L_1 and L_{23} edges [10-13] using Hartree-Slater atomic wave functions [14] as initial states, and our final states were continuum states with a free electron density of states [11]. In the region of our data from 6 - 12 Å^{-1}, the differential cross section of the Fe L_1 edge was 5 times smaller than that of the Fe L_{23} edge. Moreover, transforming the L_1 EXELFS oscillations from energy-loss space to the k-space corresponding to

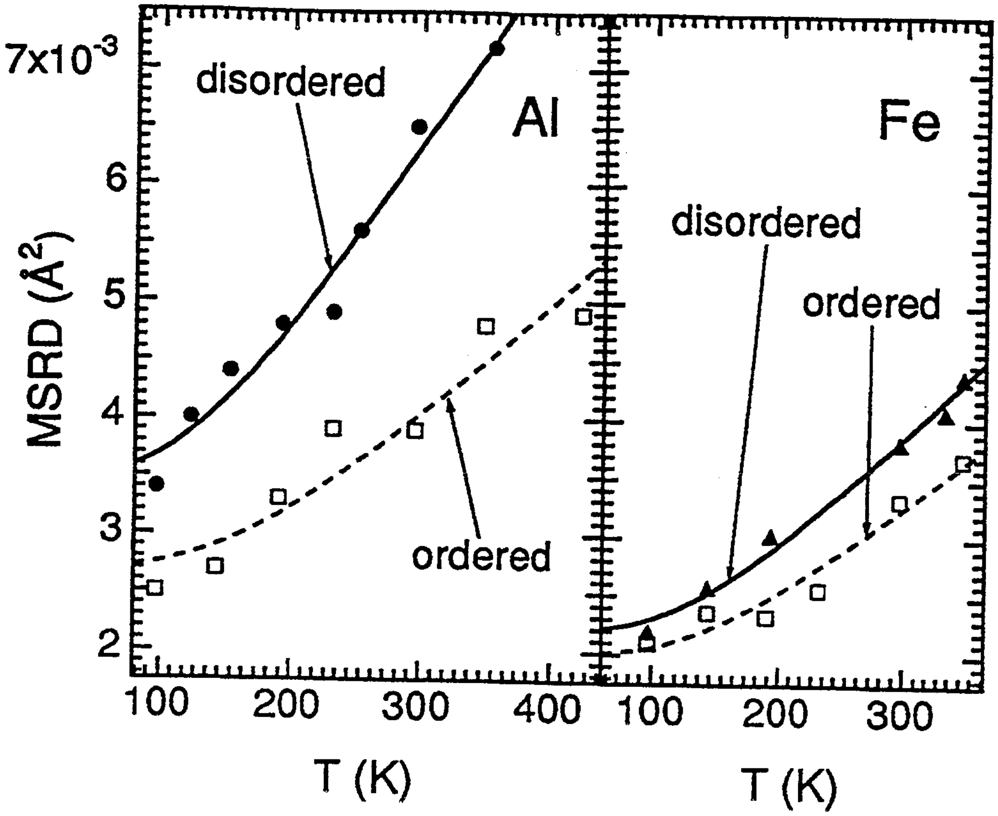

Figure 4.5 First nearest neighbor MSRD data and fits to the Einstein model for Al and Fe atoms in disordered and ordered Fe_3Al.

the L_{23} edge raises the frequencies of the L_1 EXELFS oscillations, making them incoherent. We also calculated differential scattering cross sections for the excitation of Fe 2p electrons into final states of s, p, d, or f character. It was found that in the EXELFS region, the electric dipole-allowed 2p to d transition dominates over the sum of all others by a factor of over 20. This makes possible the interpretation of the Fe L_{23} EXELFS with outgoing d waves.

By comparing the 1nn oscillations, changes in the mean-squared relative displacements (MSRD) measured from the Al K-edge (Al MSRD) and the Fe L_{23}-edge (Fe MSRD) were determined relative to the lowest-temperature datum. The MSRD data were fit to predictions of the Einstein model [15], with the lowest-temperature MSRD being free to vary. Einstein temperatures so obtained were 377 K (+28 K, -26 K) for Al atoms in disordered Fe_3Al, 490 K (+74 K, -54 K) for Al atoms in ordered Fe_3Al, 391 K (+18 K, -15 K) for Fe atoms in disordered Fe_3Al, and 431 K (+40 K, -31 K) for Fe atoms in ordered Fe_3Al. The MSRD data and their Einstein temperature fits are presented in Figure 4.5. There is a strong reduction in the Al MSRD in the ordered material, but a markedly smaller reduction in the Fe MSRD. We also observed that both the Al and the Fe MSRD in either ordered or disordered Fe_3Al are reduced with respect to the corresponding pure metal [10-12]. This is not expected from the trend of the elastic modulus of Fe–Al alloys, which decreases as aluminum is added to bcc iron [16, 17].

4.3.3 Phonon DOS Calculation

Van Dijk [3] and Robertson [4, 5] have used inelastic neutron scattering to measure phonon dispersion curves along high symmetry directions in ordered and disordered Fe_3Al. Using Robertson's force constants up to fifth

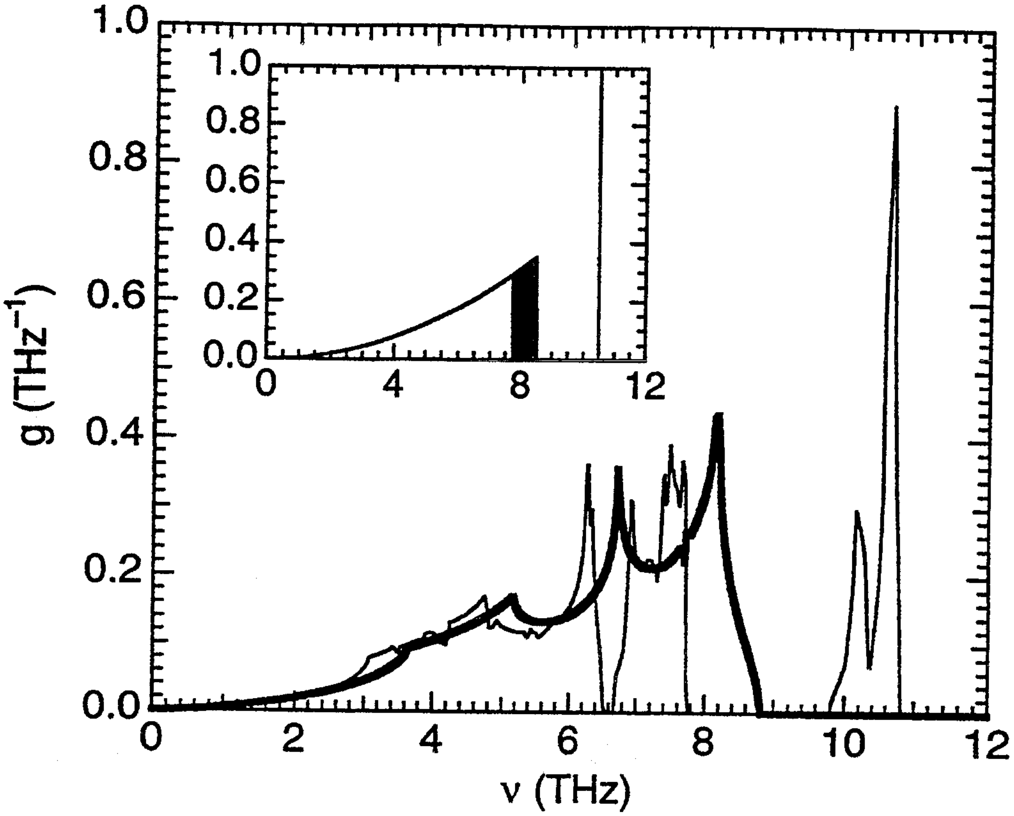

Figure 4.6 Main: Phonon DOS curves for ordered (thin curve) and disordered (thick curve) Fe_3Al, calculated using force constants from Robertson [5]. Inset: Simplified phonon DOS curves; disordered Fe_3Al curves comprise unshaded and shaded parts, ordered Fe_3Al curves comprise unshaded part and delta function at 10.5 THz.

neighbors (columns 1 and 3 of Table 4 in [5]), we calculated the phonon DOS for disordered and $D0_3$-ordered Fe_3Al. In these calculations the disordered state was represented as a bcc lattice with a basis of 1 atom having an average mass of the Fe and Al atoms (known as the virtual crystal model), and the bcc-based D0$_3$-ordered structure was represented as an fcc lattice with a 4-atom basis. The phonon dispersion curves for high symmetry directions were reproduced, and were in excellent agreement with those presented by Robertson [5]. The dynamical matrix, D(**q**), (3 × 3 for the disordered state, 12 × 12 for the ordered state) was diagonalized for approximately 5 million different values of **k** in the first Brillouin zone for the disordered alloy, and approximately 10 million values for the ordered alloy. The resulting phonon DOS curves for the disordered and ordered alloys, $g^D(\nu)$ and $g^O(\nu)$, are presented in Figure 4.6. The phonon DOS of the disordered alloy would have its sharp features broadened significantly, but this will not affect qualitatively the arguments that follow.

These DOS curves were then used to calculate heat capacities. Each normal mode was given a phonon occupation set by Bose-Einstein statistics. The heat capacity of the disordered and ordered materials is the heat capacity per mode integrated over the corresponding phonon DOS. The difference in heat capacity, $\Delta C_V(T) \equiv C_V^D - C_V^O$, is:

$$\Delta C_V(T) = 3Nk_B \int_0^\infty \left(g^D(\nu) - g^O(\nu)\right) \left(\frac{h\nu}{k_BT}\right)^2 \frac{\exp\left(\frac{h\nu}{k_BT}\right)}{\left(\exp\left(\frac{h\nu}{k_BT}\right) - 1\right)^2} d\nu \quad . \qquad 4.2$$

The calculation from Equation 4.2 is presented as a solid curve in Figure 4.3. There is qualitative agreement between the calculated and measured $\Delta C_V(T)$. The disparity could originate with several sources, including the different composition of Robertson's disordered sample [5]. Substituting Equation 4.2

for $\Delta C_V(T)$ into Equation 4.1 and integrating, we obtain a $\Delta S_{vib} = 0.186$ k_B/atom in the high temperature limit.

We perturbed the mass of the aluminum atoms in $D(\mathbf{q})$ and recalculated the phonon DOS curves. The highest frequency modes were most sensitive to changes in the aluminum mass, so we deduce that these modes originate with the vibration of the aluminum-rich sublattice in the $D0_3$ ordered structure, in agreement with Robertson [5]. Other ordered alloys also exhibit such high frequency modes [18-20], which seem to originate with stiffly-bonded, low-mass atoms. Furthermore, the Al atoms are the minority species in transition metal (T) aluminides of the T_3Al composition, so the Al atoms undergo the largest change in local chemical environment upon ordering. We therefore expect these high frequency modes to be strongly sensitive to the state of chemical order in the alloy.

The EXELFS MSRD measurements, which are dominated by backscattering from Fe neighbors, are most sensitive to high frequency vibrational modes. The larger Al MSRD (Figure 4.4) is consistent with the light Al atoms having larger vibrational amplitudes in these highest frequency modes. The high frequency modes of vibration of the aluminum-rich sublattice in the ordered structure will have a low phonon occupation. The Al MSRD of the aluminum atoms will therefore decrease upon ordering — more so than for the Fe MSRD. This trend is also seen in Figure 4.4. This same argument explains the large change in MSRD for aluminum atoms upon $L1_2$ ordering in Ni_3Al [2].

The most prominent change upon ordering in the phonon DOS curves are the gap around 9 THz for the ordered alloy, and its optical modes at 10 - 11 THz. We modeled these features with the simplified DOS curves presented as the inset in Figure 4.5. The model uses a Debye model for the disordered alloy with $\nu_{\text{Debye}} = 8.5$ THz. For the ordered alloy, we deleted the top 1/4 of the modes in the Debye model (from $(3/4)^{1/3}\,\nu_{\text{Debye}}$ to ν_{Debye} of the disordered alloy), and placed them in a single high frequency Einstein-like distribution at $\nu_{\text{Einstein}} = 10.5$ THz. The $\Delta C_V(T)$ for this model, calculated with Equation 4.2, is presented as a dashed curve in Figure 4.3, and the high temperature limit of its $\Delta S_{\text{vib}}(T)$ was 0.185 k_B/atom.

We believe that the vibrational entropy calculated from the phonon DOS curves is an overestimate because of problems with the virtual crystal approximation used in the modeling of the disordered alloy. In this approach, the disordered alloy is modeled as a homogeneous bcc alloy with an atomic weight of 48.63 (the compositionally-weighted average of Fe and Al atoms). In fact, however, the disordered alloy will have strong local inhomogeneities, and may well have local regions with transient vibrational energies around 10 THz. The existence of such high frequency vibrational processes in disordered alloys are best measured by inelastic incoherent scattering methods [21, 22], and these measurements provide a useful complement to more traditional interpretations of lattice dynamics in terms of phonon modes [23-25]. Such incoherent inelastic scattering measurements performed on ordered and disordered Ni_3Al (Chapter Five) showed that high frequency vibrational processes do exist in transition metal aluminides.

4.4 Conclusions

The difference in heat capacity between matched samples of disordered and D0$_3$-ordered Fe$_3$Al was measured by calorimetry. These data on $\Delta C_V(T)$ were used to obtain the difference in vibrational entropy between disordered and D0$_3$-ordered Fe$_3$Al, which was (0.10 ± 0.03) k_B/atom at high temperatures, with the ordered alloy having the lower vibrational entropy. Extended electron energy loss fine structure spectrometry (EXELFS) was used to measure the mean-squared-relative displacement (MSRD) between Fe atoms and their neighboring atoms, and between Al atoms and their neighbors. These EXELFS measurements were performed at various temperatures, so the effective Debye-Waller factor for the central atom and its first nearest neighbor shell could be determined. These data showed that upon ordering, the temperature dependence of the Al MSRD underwent a larger change than did the temperature dependence of the Fe MSRD. The Al atoms became more stiffly bound in the ordered alloy, whereas the Fe atoms underwent a much smaller and perhaps insignificant change.

Analysis of the vibrational modes of the ordered and disordered alloys was performed with a Born-von Kármán model, using force constants obtained from previous neutron scattering measurements of phonon dispersion curves. Phonon DOS curves for the ordered and disordered alloys were calculated, and the results provided a heat capacity difference between ordered and disordered Fe$_3$Al that was in qualitative agreement with the experimental results from calorimetry. The most significant difference in the phonon DOS of the ordered and disordered alloys was the prominent peak at 10.5 THz in the ordered alloy, corresponding to optical modes involving large-amplitude vibrations of the aluminum-rich sublattice. This shift of 1/4 of the phonon modes from about 8.5 THz to 10.5 THz was found to be the main source of the difference in vibrational entropy of ordered and disordered Fe_3Al, and is the likely reason why the EXELFS results showed that the Al atoms were bound more stiffly in the ordered alloy.

Although the results from calorimetry and the phonon DOS are in qualitative agreement, we believe that the discrepancy between the two methods results from problems with the virtual crystal approximation used in the modeling of the disordered alloy. The disordered alloy may well have local regions with transient vibrational energies around 10 THz, which would suppress the difference in vibrational entropy from what is expected with the virtual crystal model of the bcc phonon DOS.

4.5 Acknowledgments

We acknowledge the help and interest of Dr. C. C. Ahn, and conversations with G. Ackland, G. D. Barbulsky and G. Ceder. This work was supported by the U. S. Department of Energy under contract DE–FG03–86ER45270.

References

[1] J. K. Okamoto, Ph.D. thesis, Caltech, 1992.

[2] L. Anthony, J. K. Okamoto, and B. Fultz, Phys. Rev. Lett. **70**, 1128 (1993).

[3] C. Van Dijk, Phys. Lett. A **34**, 255 (1970).

[4] I. M. Robertson, Solid State Commun. **53**, 901 (1985).

[5] I. M. Robertson, J. Phys.: Condens. Matter **3**, 8181 (1991).

[6] Z. Q. Gao and B. Fultz, Philos. Mag. B **67**, 787 (1993).

[7] B. Fultz and Z.Q. Gao, Nucl. Instr. and Methods in Phys. Res. **B76**, 115 (1993).

[8] B. Fultz, "Chemical Systematics of Iron-57 Hyperfine Magnetic Field Distributions in Iron Alloys," Mössbauer Spectroscopy Applied to Magnetism and Materials Science, G. J. Long and F. Grandjean, eds., (Plenum Press: New York, 1993), Chapter 1.

[9] R. D. Leapman, L. A. Grunes, and P. L. Fejes, Phys. Rev. B **26**, 614 (1982).

[10] J. K. Okamoto, D. H. Pearson, C. C. Ahn, and B. Fultz, in Transmission Electron Energy Loss Spectrometry in Materials Science, edited by M.M. Disko, C.C. Ahn, and B. Fultz (The Minerals, Metals & Materials Society: Warrendale, PA, 1992), page 183.

[11] H. Shuman and P. Kruit, Rev. Sci. Instrum. **56**, 231 (1985).

[12] R. D. Leapman, P. Rez, and D. F. Mayers, J. Chem. Phys. **72**, 1232 (1980).

[13] G. Beni and P. M. Platzman, Phys. Rev. B **14**, 1514 (1976).

[14] J. Okamoto, C. Ahn, and B. Fultz, in Microbeam Analysis - 1990, J. R. Michael and P. Ingram, eds. (San Francisco Press, 1990) p. 56-58.

[15] H. J. Leamy, Acta Metall. **15**, 1839 (1976).

[16] H. J. Leamy, E. D. Gibson, and F. X. Kayser, Acta Metall. **15**, 1827 (1976).

[17] C. Stassis, F. X. Kayser, C.-K. Loong, and D. Arch, Phys. Rev. B **24**, 3048 (1981).

[18] M. Mostoller, R. M. Nicklow, D. M. Zehner, S.-C. Lui, J. M. Mundenar, and E. W. Plummer, Phys. Rev. B **40**, 2856 (1989).

[19] Y. Noda and Y. Endoh, J. Phys. Soc. Japan **12**, 4225 (1988).

[20] S. Katano, M. Iizumi, and Y. Noda, J. Phys. F: Met. Phys. **18**, 2195 (1988).

[21] B. Fultz, T. A. Stephens, W. Sturhahn, T. S. Toellner, E. E. Alp, X. Zhang, M. Ando, Y. Yoda, S. Kikuta, and M. Seto, Phys. Rev. Lett. **74**, 3832 (1995).

[22] B. Fultz, L. Anthony, L. J. Nagel, R. M. Nicklow, and S. Spooner, Phys. Rev. B **52**, 3315 (1995).

[23] L. Anthony, L. J. Nagel, J. K. Okamoto, and B. Fultz, Phys. Rev. Lett. **73**, 3034 (1994).

[24] L. Anthony, L. J. Nagel, and B. Fultz, in Solid-Solid Phase Transformations, W. C. Johnson, J. Howe, D. E. Laughlin, and W. A. Soffa, eds. (TMS: Warrendale, PA, 1994), p. 467-472.

[25] B. Fultz, L. Anthony, J. L. Robertson, R. M. Nicklow, S. Spooner, and M. Mostoller, Phys. Rev. B **52** 3280 (1995).

Chapter Five Ni_3Al

5.1 Introduction

The phase diagram for Ni_3Al is shown in Figure 5.1. Previous calorimetric measurements showed the difference in vibrational entropy of ordered and disordered Ni_3Al to be about 0.3 k_B/atom [1], which is a large fraction of the difference in configurational entropy ($\leq$ 0.57 k_B/atom). We hypothesize that the formation of a sublattice of stiffly-bonded, light aluminum atoms in the $L1_2$ structure of Ni_3Al (shown in Figure 5.2) causes the ordered state to have a lower vibrational entropy than the disordered state. Although a neutron inelastic scattering experiment has been performed

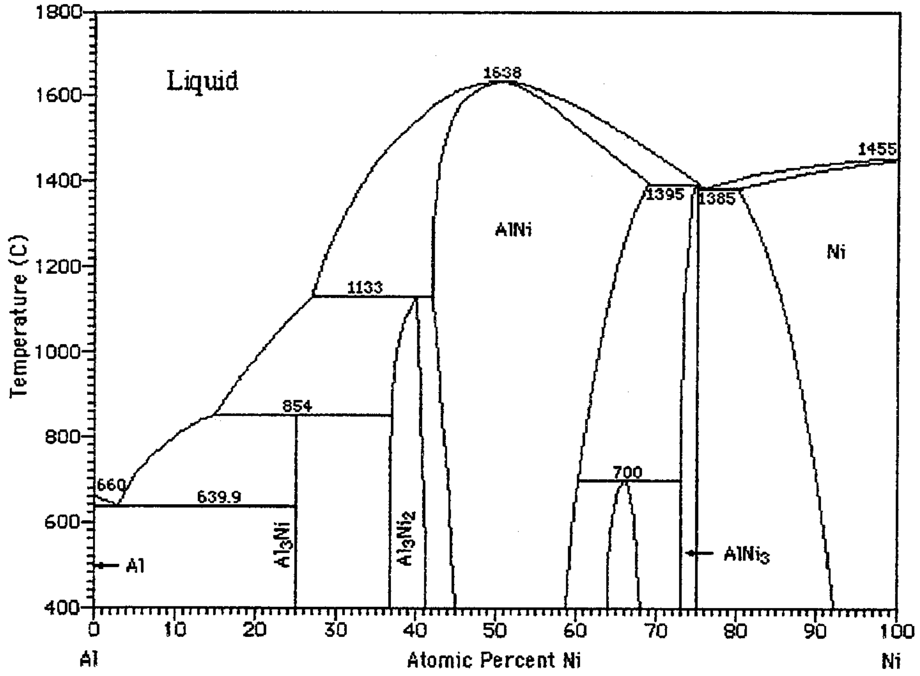

Figure 5.1 The phase diagram for the Al-Ni alloy system. From H. J. Okamoto, Phase Equilibria 1993 14(2) p. 257.

on a single crystal of Ni_3Al with $L1_2$ order [3], it is unfortunately impossible to prepare single crystal specimens of disordered fcc Ni_3Al. Measurements of neutron inelastic coherent scattering from single crystals therefore cannot be used to identify the differences in the types of phonons in ordered and disordered Ni_3Al. The present experiment was designed to provide some of this information by inelastic incoherent and coherent scattering from polycrystalline powders.

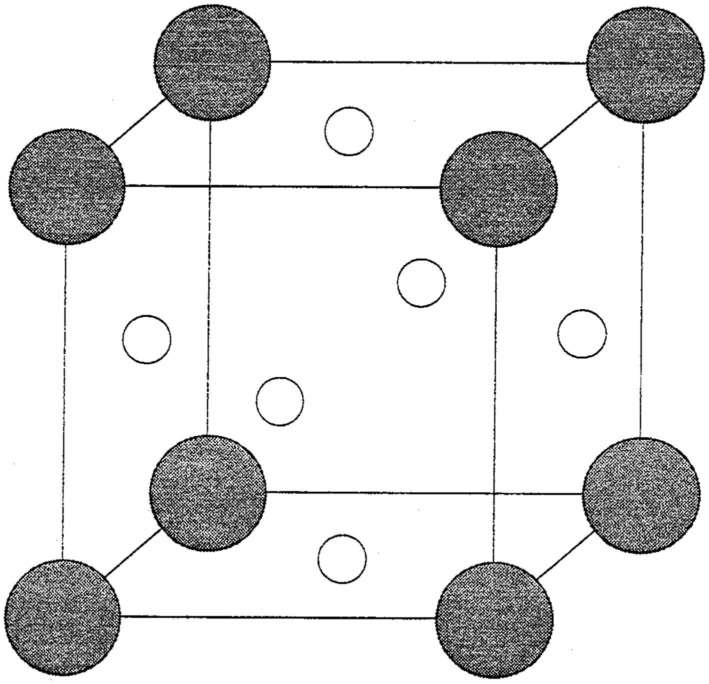

Figure 5.2. The $L1_2$ structure of Ni_3Al. The large gray circles represent Al atoms and the small white circles represent Ni atoms.

5.2 Samples and Experiment

Powders of Ni_3Al were made by mechanical alloying [4, 5]. Measured amounts of elemental nickel and aluminum powders were milled in a Spex 8000 mixer/mill with hardened steel vials and stainless steel balls and a ball-to-powder weight ratio of 2:1. With hexane added to the vial, nearly complete alloying occurred in 3 - 4 hours, and several batches of Ni_3Al powder were prepared by milling for 8 hours at room temperature. X-ray diffractometry was performed with an Inel CPS–120 diffractometer using Co Ka radiation. The total absence of the (100) and (110) superlattice diffractions in the as-milled material, also seen in its neutron diffraction pattern, showed that the as-milled powder was essentially without $L1_2$ long-range order (LRO). Figure 5.3 presents an x-ray diffraction pattern from the as-milled powder, and a pattern from the same powder after annealing at 450 °C for 10 hours, which was the annealing treatment used to produce $L1_2$ LRO in our samples [6-8].

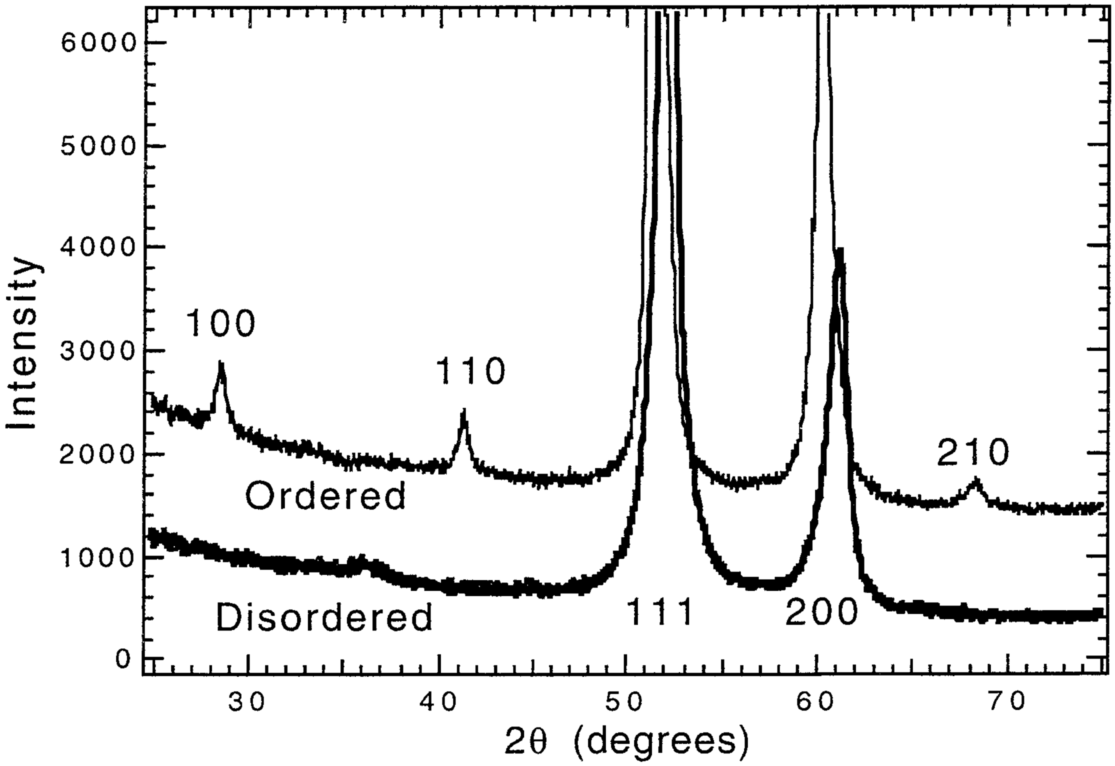

Figure 5.3 X-ray powder-diffraction patterns of the ordered and disordered Ni_3Al powders, in the region of the (100) and (110) superlattice diffractions.

Samples of the as-milled and the annealed powders, each about 50 grams, were placed in thin-walled aluminum cans and mounted on the goniometer of the HB3 triple axis spectrometer at the High Flux Isotope Reactor at the Oak Ridge National Laboratory. The spectrometer was operated in constant-Q mode with the fixed final energy, E_f, being 14.8 meV. The energy loss spectra were made by scanning the incident energy from 14.8 meV to 64.8 meV. The neutron flux from the monochromator was monitored with a fission detector, which was used to control the counting time for each data point. The incident beam on the pyrolytic graphite monochromator crystal was collimated with 40′ slits, and 40′ slits were also used between the monochromator and the sample. Pyrolytic graphite filters placed after the sample were used to remove the $\lambda/2$ contamination. The filtered beam passed through 80′ slits before the pyrolytic graphite analyzer crystal. Following the analyzer, 2° slits were used before the ^{3}He detector. With this arrangement, the energy resolution varied from about 2 meV at low energy transfer to 5 meV at 40 meV energy transfer. (In addition to these instrument parameters, several runs were performed with other instrument resolutions. Agreement between these different data sets was good.) Four values of Q were chosen for each specimen, ranging from 3.23 to 4.23 $Å^{-1}$.

5.3 Results

Energy loss spectra from the ordered and disordered Ni_3Al are presented in Figure 5.4. Individual runs were highly reproducible, as shown by the two independent (but nearly coincident) data sets from the ordered alloy with Q = 4 .23 $Å^{-1}$. Effects from the broad transverse band of phonon states are seen in all data sets from 12 to 28 meV, and some structure is visible

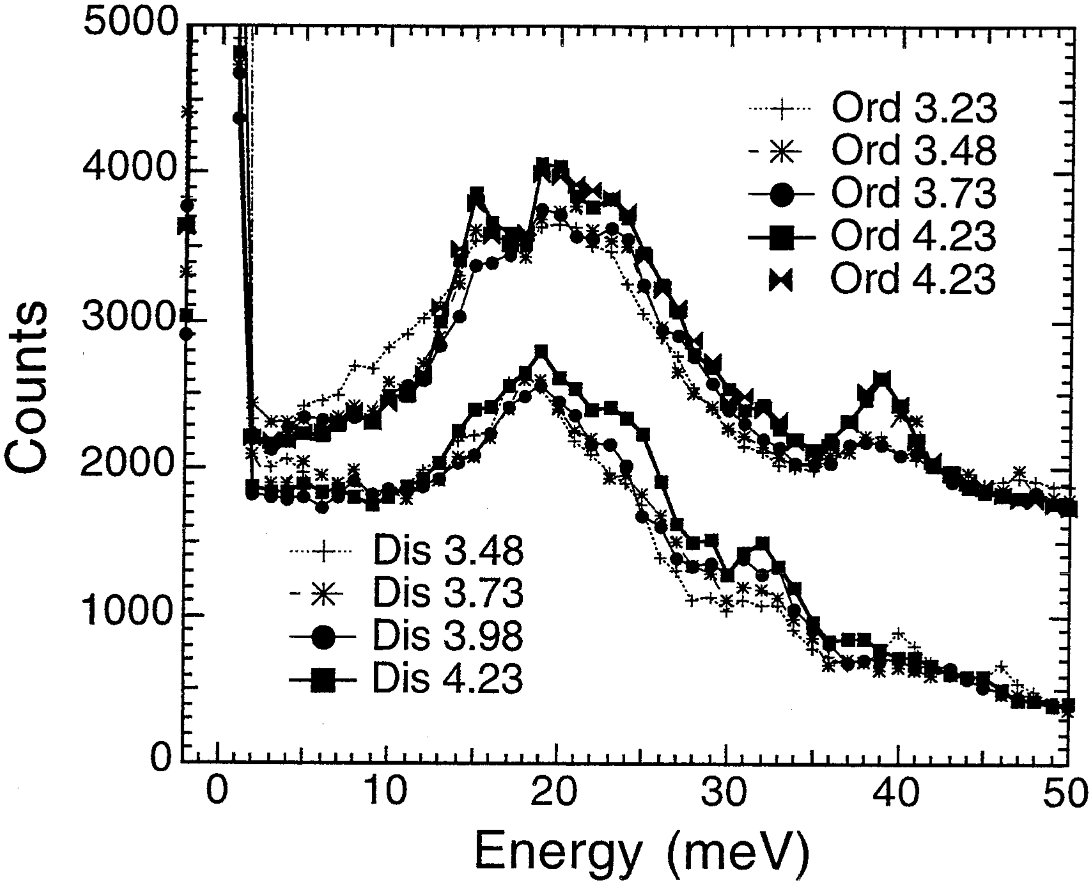

Figure 5.4 Raw neutron energy loss spectra for the ordered and disordered Ni3Al powders, obtained at four values of Q. Data for the ordered alloy are offset vertically by 1500 counts.

in this region. The energy loss spectra from the material with $L1_2$ order also shows a peak around 39 meV. This peak was found in the calculated phonon DOS obtained from the results of single crystal experiments by Stassis et al. [3]. Examination of the eigenvectors of the dynamical matrix (see Section 7.4.1) showed that it is attributable to optical modes dominated by the motions of the aluminum-rich sublattice. As discussed below, the intensity of this peak is suppressed in the present experiments, owing to the smaller scattering cross section of aluminum than that of nickel, and the relatively small vibrational amplitudes of the nickel atoms in these optical modes. No distinct peak at 39 meV is seen in the data from the disordered Ni_3Al, although some residual intensity is found around this energy. The peak at 33 meV for the disordered alloy is at approximately the same energy as the peak of the longitudinal modes for fcc nickel metal. Another distinct feature of the spectra from the disordered alloy is the stronger scattering intensity at energy losses below 10 meV or so.

5.4 Analysis of Phonon DOS

5.4.1 Calculated Phonon DOS

The analysis of the scattering data from the ordered powder was helped considerably by the availability of previous phonon dispersion measurements on single crystals of $L1_2$ Ni_3Al [3]. Although the force constants were published, we were unable to use them satisfactorily in a Born-von Kármán model. Independent fits [9] to the experimental phonon dispersion curves of Reference [3] provided the following set of force constants:

$$\{\phi_{xx}\begin{pmatrix} & 1 & \\ 1 & & 2\end{pmatrix} = 16.984,\ \phi_{xx}\begin{pmatrix} & 1 & \\ 2 & & 2\end{pmatrix} = 18.882,\ \phi_{zz}\begin{pmatrix} & 1 & \\ 1 & & 2\end{pmatrix} = -1.128,$$
$$\phi_{zz}\begin{pmatrix} & 1 & \\ 2 & & 2\end{pmatrix} = -0.376,\ \phi_{xy}\begin{pmatrix} & 1 & \\ 1 & & 2\end{pmatrix} = 18.112,\ \phi_{xy}\begin{pmatrix} & 1 & \\ 2 & & 2\end{pmatrix} = 19.258,$$
$$\phi_{xx}\begin{pmatrix} & 2 & \\ 1 & & 1\end{pmatrix} = 1.48,\ \phi_{xx}\begin{pmatrix} & 2 & \\ 2 & & 2\end{pmatrix} = -1.38,\ \phi_{yy}\begin{pmatrix} & 2 & \\ 1 & & 1\end{pmatrix} = 1.864,$$
$$\phi_{yy}\begin{pmatrix} & 2 & \\ 2 & & 2\end{pmatrix} = 0.645\}\ [\mathrm{N/m}].$$

The force constants are of the form $\phi_{ab}\begin{pmatrix} & l & \\ k & & k'\end{pmatrix}$, where a and b are the indices of the force constant tensor, l specifies the nearest-neighbor distance, and k and k′ indicate the sublattice pair, with Al atoms occupying sublattice 1 and Ni atoms occupying sublattice 2. Using these force constants, the dynamical matrix **D**(**q**) was diagonalized for approximately 10^6 values of **k** distributed uniformly over the first Brillouin zone. Histogram binning of the resulting eigenfrequencies provided the phonon DOS, presented at the top of Figure 5.5.a. The dynamical structure factors were calculated simultaneously. Truncating the force constants at second neighbor distances provides a reasonable, but imperfect fit to the phonon dispersion curves, and there are some differences between our phonon DOS and that of Stassis et al. [26]. The present force constants are nevertheless adequate for identifying trends in the scattering intensity versus Q.

5.4.2 Calculated Dynamical Structure Factors

Also shown at the top of Figure 5.5.a is the dynamical structure factor intensity for incoherent scattering of phonons of frequency ν, $|G_{inc}(\nu,\mathbf{Q})|^2$, obtained from the Born-von Kármán model as the following sum [10] (with a factor involving the projection of the momentum transfer **Q** on the polarization vector $\varepsilon^{\gamma}_{rk}(\mathbf{q})$ for the atom of mass M_{rk} at the position $\mathbf{r}_k$ of the phonon in the branch γ with wavevector **q**) :

$$|G_{inc}(\nu,\mathbf{Q})|^2 = \sum_{rk} \frac{\sigma_{inc,rk}}{M_{rk}} \sum_{\gamma} \sum_{\mathbf{q}} |\mathbf{Q}\cdot\varepsilon^{\gamma}_{rk}(\mathbf{q})|^2 \,\delta(\nu - \nu_{\gamma}(\mathbf{q})) \ . \qquad 5.1$$

For each atom, branch, and **q**, the crystallographic average of Equation 5.1 over the various directions of **Q** is: $\sigma_{inc,rk}\, Q^2 |\varepsilon r^{\gamma}_{k}(\mathbf{q})|^2 / 3Mr_k$. This contribution to $|G_{inc}(\nu,\mathbf{Q})|^2$ was binned during the phonon DOS calculation, as was the contribution to the partial phonon DOS, $|\varepsilon r^{\gamma}_{k}(\mathbf{q})|^2$. The peak at 39 meV is suppressed considerably in the dynamical structure factor intensity for incoherent scattering. The partial phonon DOS for the aluminum and nickel atoms (essentially Equation 5.1 with the $\mathbf{r}_k$=1 (Al) or $\mathbf{r}_k$=2 (Ni) terms only) showed that at the energies around 39 meV, the aluminum atoms have much larger vibrational amplitudes than do nickel atoms. However, the incoherent scattering from aluminum is negligible ($\sigma_{inc} < 0.01$ barn) compared to that of nickel ($\sigma_{inc} = 5.0$ barn) [10], so incoherent scattering around 39 meV is rather weak.

The dynamical structure factor intensity for coherent scattering, $|G_{coh}(\nu,\mathbf{Q})|^2$, was calculated as [10]:

$$|G_{coh}(\nu,\mathbf{Q})|^2 = \sum_{\mathbf{r}_k} \frac{1}{M_{\mathbf{r}_k}} \sum_{\gamma} \sum_{\tau} \sum_{\mathbf{q}} |b_{\mathbf{r}_k}\, \mathbf{Q}\cdot\varepsilon^{\gamma}_{\mathbf{r}_k}(\mathbf{q})\ e^{i\mathbf{Q}\cdot\mathbf{r}_k}|^2\, \delta(\nu-\nu_\gamma(\mathbf{q}))\, \delta(\mathbf{Q}-\mathbf{q}-\tau), \quad 5.2$$

where τ is a reciprocal lattice vector and $b_{\mathbf{r}_k}$ is the coherent scattering length. The crystallographic average of the inelastic coherent scattering required an evaluation of the dynamical structure factor intensity at explicit values of **Q** with respect to the crystallographic axes. For a given value of Q, the directions of **Q** were chosen with an isotropic probability distribution using a Monte Carlo sampling procedure.

Results for the total scattering, inelastic coherent plus inelastic incoherent, are presented at the bottom of Figure 5.5.a. Differences in the shape of the curves with different Q are caused by the inelastic coherent scattering, whose variation with Q depends in a complicated way on the phonon DOS and relationships between **Q** and the Brillouin zone boundary

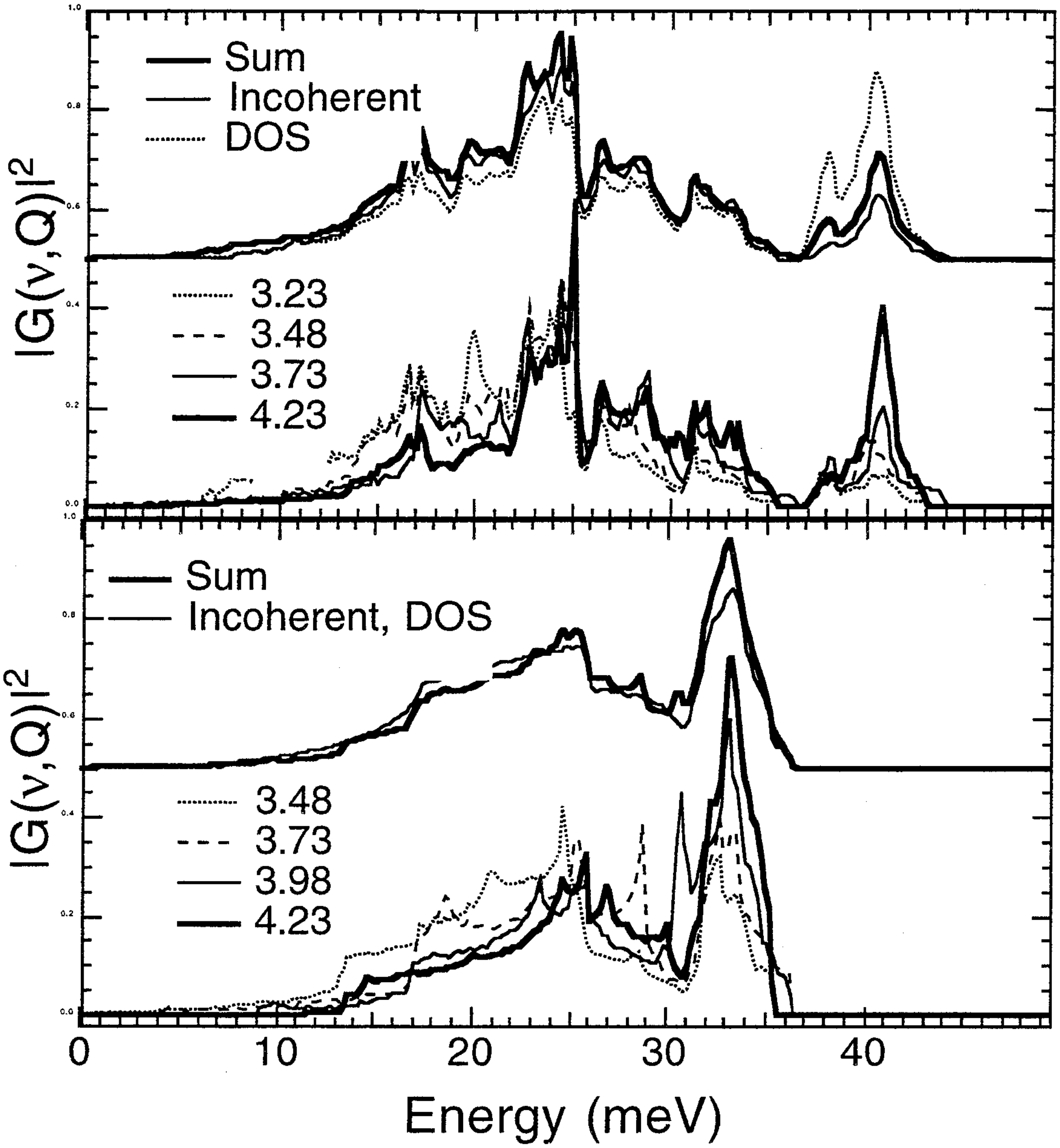

Figure 5.5. a. Calculations for L1$_2$ Ni$_3$Al. Top: phonon DOS, incoherent scattering spectrum, and average of all data at the bottom of a. Bottom: total inelastic scattering (incoherent plus angle-averaged coherent) for L1$_2$ Ni$_3$Al at various values of Q. b. Calculations for fcc Ni. Top: phonon DOS, incoherent scattering spectrum, and average of all data at the bottom of b. Bottom: total inelastic scattering (incoherent plus angle-averaged coherent) for fcc Ni at various values of Q.

[11]. Our calculations reproduce some of the detailed Q-dependence of the experimental data on ordered Ni3Al. For example, the strong scattering observed for $Q = 3.23$ Å^{-1} around 10 meV is reproduced well in the calculation. The general trend for the scattering at higher energies to increase with Q is also reproduced well.

The top of Figure 5.5.a also shows the average of the four calculated curves at the bottom of Figure 5.5.a, each normalized to unity. It differs from the phonon DOS curve primarily in its overemphasis of the low energy part of the spectrum, and underemphasis of the higher energy part of the spectrum. (This average is similar, but not identical, to the dynamical structure factor intensity for incoherent scattering.) Dividing the phonon DOS by this average provided a "dynamical structure factor correction function" with a shape much like a step function, having an amplitude of 0.69 for energies below 35 meV, and an amplitude of 1.94 for energies above 35 meV. For correction of the summed experimental data, the step in the dynamical structure factor correction function was smoothed by a gaussian function with a full width at half maximum of 4 meV, the expected experimental resolution.

The analysis for the disordered alloy is more problematic, since force constants are not available from previous work. We began by assuming that the phonon DOS of the disordered Ni3Al was the same as that of fcc Ni metal [12]. Starting with this phonon DOS of a typical fcc metal, we devised two methods for the analysis of the energy loss spectra from disordered Ni3Al. The top of Figure 5.5.b shows the phonon DOS of fcc nickel. (For a monatomic crystal, as assumed in the virtual crystal approximation, the phonon DOS has the same shape as the dynamical structure factor intensity for incoherent scattering.) Also shown in Figure 5.5.b are the total incoherent plus coherent structure factor intensities from fcc nickel at the different values of Q used in the experiment. The average of these total inelastic scattering intensities is presented at the top of Figure 5.5.b. We obtained a dynamical structure factor correction function for converting the inelastic scattering intensity into a phonon DOS, but it was not used for the analysis presented below. This correction function was roughly constant in energy, so in one approach for data analysis we assumed the correction factor to be unity. It certainly can be argued that the virtual crystal approximation is unreliable; the vibrational spectrum of the disordered crystal must be different from that of a monatomic fcc crystal. The experimental data do show that there is some intensity in the regions of the optical modes at 39 meV, presumably due to vibrations of aluminum atoms in local regions of partial order (light Al atoms vibrating in a cage of Ni atoms [2, 13]). So as a second method for analysis of the data from the disordered alloy, we converted the summed inelastic scattering intensity into an approximate phonon DOS by using the same dynamical structure factor correction function as was used for the ordered alloy (the step function with a jump at 35 meV). We do not know which method for data analysis is more appropriate, so in what follows we present both.

5.4.3 Temperature

Another step in obtaining the phonon DOS involved the correction for the phonon populations in the different modes. We calculated the inelastic incoherent scattering using the conventional multiphonon expansion [14-16].

The calculation was performed for room temperature with the phonon DOS curves presented at the tops of Figures 5.5.a and 5.5.b. The results showed that at the relatively low values of Q and temperature of the present experiments, the inelastic scattering is strongly dominated by one-phonon processes. Multiphonon corrections would have made little difference to the resultant phonon DOS, so these corrections were not performed. Also, our normalization of individual data sets, discussed below, eliminated the need to correct for the Debye-Waller factor suppression of the scattered intensity for larger values of Q. We do neglect differences in how the Debye-Waller factors for nickel and aluminum atoms change with Q, but these differences are not important because they are not large, and the scattering is dominated by the nickel atoms.

5.4.4 Data Analysis Procedure

The features of the calculated scattering (Sections 5.4.2 and 5.4.3) led us to the following procedure for obtaining an approximate phonon DOS from the experimental data of Figure 5.4. Our data analysis procedure has some similarities to methods used previously [15-19]. The individual data sets for both the ordered and disordered alloys were corrected by subtracting the same constant background from all data sets, which is a good approximation for data from the HB3 spectrometer. Each background-corrected spectrum was divided by the one-phonon correction factor, $(n(\nu) - 1)/\nu$ [10]:

$$\frac{n(\nu) - 1}{\nu} = \frac{1}{\nu\,[1 - \exp(-h\nu/kT)]} \qquad 5.3$$

Next, the individual spectra for the four values of Q for the disordered and ordered alloys were individually normalized to unity and then summed. Finally, the summed data for the ordered alloy were multiplied by the dynamical structure factor correction function, and this result was normalized to unity. The resulting approximate phonon DOS for the ordered alloy is presented in Figure 5.6. As mentioned in Section 5.4.2, we are uncertain if the disordered alloy can be treated as a virtual fcc crystal, or if we should use a correction factor as in the ordered alloy to weight more heavily the data at higher energies. We expect that these two assumptions provide reasonable upper and lower bounds on the actual phonon DOS, so both results are presented in Figure 5.6.

5.5 Discussion

5.5.1 Phonon DOS

The phonon DOS of the ordered alloy presented in Figure 5.6 is in reasonably good agreement with the phonon DOS reported by Stassis et al. [3]. For comparison with the phonon DOS at the top of Figure 5.5.a, we convolved the calculated data with a Gaussian function of width 4 meV. The overall agreement between the two curves ("$L1_2$ exp" and "$L1_2$ calc") is generally satisfactory. The peak at 39 meV in the calculated curve is a bit too large, however, having an integrated area of about 0.28, rather than the expected value of 1/4. Discrepancies in the matching of the calculated and experimental $g(\nu)$ curves of the ordered alloy originate in part with our method of analysis, but also with the simplicity of the force constants (up to second nearest neighbor only) used in the Born-von Kármán model.

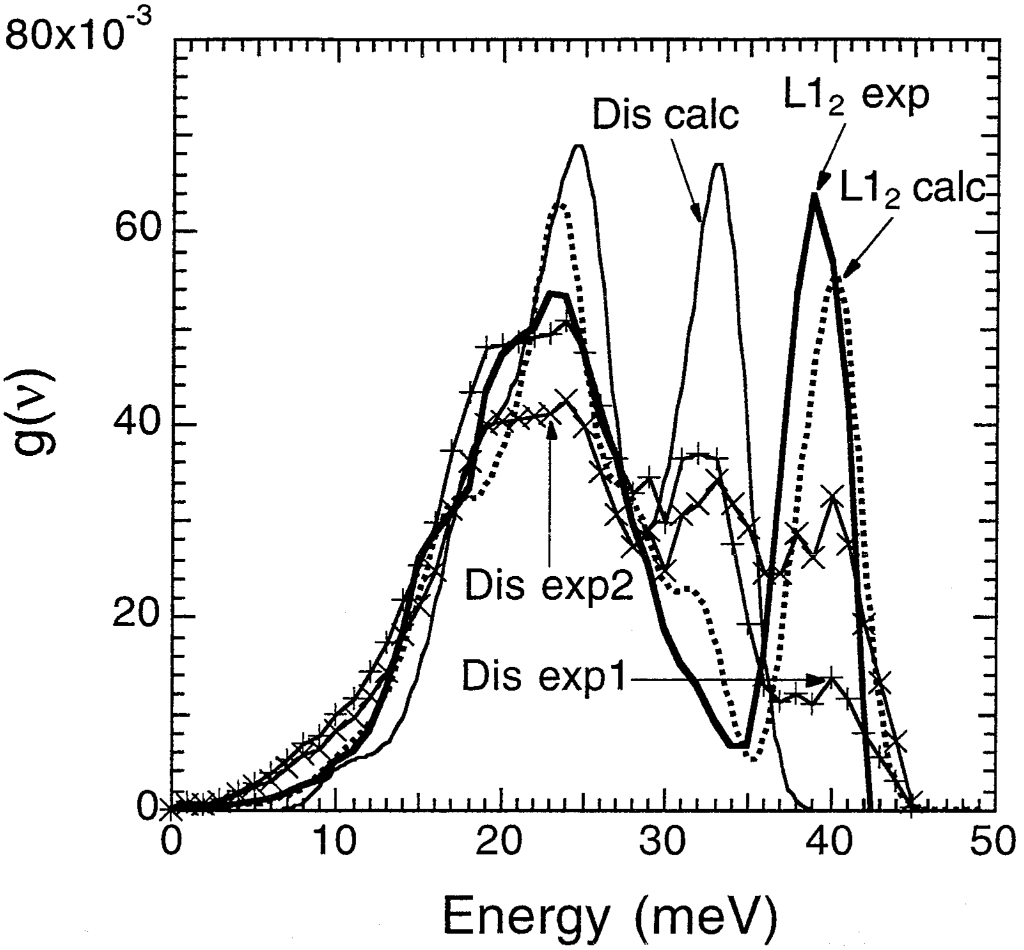

Figure 5.6 Phonon DOS obtained by processing the experimental data of Figure 5.4. The curve "L1_2 exp" was obtained from the data from the annealed powder with the L1_2 structure. The two curves "Dis exp1" and "Dis exp2" were obtained from the data from the as-milled powder, with two assumptions about the weighting of the observed intensity at high energies (see Section 5.4). The phonon DOS's at the tops of Figures 5.5.a and 5.5.b were convolved with a gaussian instrument function to provide the curves "L1_2 calc" and "Dis calc."

For the disordered alloy, the experimental g(v) curves show an enhanced intensity at energies around 10 meV. Some of this intensity could arise from the lifetime broadening of the phonon energies in the disordered alloy. It could also originate from the internal vibrations of the nanocrystallites produced by ball milling, hydrogen contamination of the specimen, or both. We do not expect these latter two problems to affect the phonon DOS of the disordered alloy at higher energies, however.

It is not surprising that there are significant differences in the experimental curves of the disordered Ni_3Al and the calculated phonon DOS curves of nickel, a monatomic fcc metal. The first difference is independent of our two methods of data analysis. In comparison to the calculated curve, the experimental $g(\nu)$ curves show a significantly weaker peak from longitudinal-mode phonons at 33 meV. Some of this loss of intensity could be associated with the lifetime broadening of the energy spectrum from the disordered alloy, but we believe the change in intensity is larger than expected for this mechanism. Another difference between the experimental and calculated phonon DOS of the disordered alloy is found around 39 meV. Because we do not know the different atom vibrations involved in this scattering, we cannot predict reliably the intensity around 39 meV. However, both our methods of data analysis provide some intensity in this energy range. This intensity is certainly suppressed considerably from its intensity in the ordered alloy, but it is non-negligible. Both methods of processing the data from the disordered alloy suggest the presence of a bimodal high energy structure with peaks around 33 and 39 meV. It is tempting to associate these peaks with the motions of nickel and aluminum atoms, respectively, but such a resolution cannot be justified rigorously.

5.5.2 Vibrational Entropy

At high temperatures, the difference in vibrational entropy of the disordered and ordered Ni_3Al, $\Delta S_{vib} \equiv S_{vib}^{dis} - S_{vib}^{ord}$, depends in a straightforward way on the difference in the phonon DOS of the two phases, $g^{dis}(\nu) - g^{ord}(\nu)$:

$$\Delta S_{vib} = -3k_B \int_0^\infty \left(g^{dis}(\nu) - g^{ord}(\nu)\right) \ln(\nu)\, d\nu \quad , \qquad 5.4$$

where the difference avoids problems with the dimensions of the argument of the logarithm. When the phonon DOS of the disordered alloy was obtained from the virtual crystal approximation without any dynamical structure factor correction, Equation 5.4 gave $\Delta S_{vib} = 0.30\ k_B$/atom. With the phonon DOS determined with the dynamical structure factor correction factor of the ordered alloy (i.e., with the assumption that the vibrations with energies above 35 meV involve primarily motions of aluminum atoms), $\Delta S_{vib} = 0.10\ k_B$/atom. For comparison, a value of ΔS_{vib} somewhat less than $0.3\ k_B$/atom was obtained by cryogenic calorimetry and by extended electron energy loss fine structure spectroscopy measurements on evaporated thin films of Ni_3Al [1].

Some of the contribution to ΔS_{vib} from Equation 5.4 is associated with the intensity of the phonon DOS of the disordered alloy at energies below 10 meV, but examination of the integrand $g^{dis}(\nu) \ln(\nu)$ showed that this was not the major effect. The difference between the vibrational entropies of the ordered and disordered alloys is caused primarily by differences in the energy spectrum at higher energies near 39 meV. Because the ordered alloy has a sublattice of aluminum atoms, the high-frequency vibrational modes involving primarily these light but stiffly-bonded atoms suppress the vibrational entropy of the ordered alloy. The present experiment shows that the vibrational spectrum of the disordered alloy has some intensity at the energies of the optical modes in the ordered alloy, but much less than for the ordered alloy. This effect of the optical modes is much the same as was proposed for Fe_3Al [2]. The present measurements suggest, however, that for the purpose of understanding the magnitude of vibrational entropy, it may be problematical to analyze the phonon DOS with a virtual crystal approximation. The lack of vibrational modes at high energies in the previous calculation for disordered bcc Fe_3Al may have been why the calculated phonon DOS curves for ordered and disordered Fe_3Al provided a DS_{vib} that was larger than was obtained from calorimetry [2].

5.6 Conclusions

We performed inelastic neutron scattering experiments on Ni_3Al in two states of chemical order: with $L1_2$ LRO and as a disordered fcc solid solution. For each sample, energy loss spectra were collected at four values of Q. A Born-von Kármán analysis was performed with force constants obtained from single crystal experiments, and the results from this analysis suggested a procedure for extracting an approximate phonon DOS from the energy loss spectra of the ordered alloy. The resulting phonon DOS was in good agreement with the phonon DOS obtained previously for $L1_2$ Ni_3Al. The spectra from the disordered alloy were also analyzed with this method, and by another method that assumed that the participation of the nickel and aluminum atoms in the scattering was independent of phonon energy.

The most significant difference in the phonon DOS of the ordered and disordered alloys was the prominent peak at 39 meV in the ordered alloy, corresponding to optical modes involving large-amplitude vibrations of the aluminum-rich sublattice. The intensity near 39 meV was much weaker in the disordered alloy, but not negligible. The corrected phonon DOS curves of the disordered and ordered alloys were used to calculate a difference in vibrational entropy which was $S_{vib}^{dis} - S_{vib}^{ord} = (+0.2 \pm 0.1)\ k_B/\text{atom}$, in reasonable agreement with previous measurements by calorimetry. The main contribution to this difference in vibrational entropy was the difference in the phonon spectrum around 39 meV, which is the energy of optical modes involving vibrational motions of primarily the aluminum-rich sublattice of the ordered alloy.

5.7 Acknowledgments

We thank B. Hennion [9] for fitting the phonon dispersion curves of Ni_3Al [3] with a Born-von Kármán model, and supplying us with a set of force constants. L. Preister performed much of the powder preparation. The Oak Ridge National Laboratory is managed for the Department of Energy by Martin Marietta Energy Systems, Oak Ridge, TN, under contract DE-AC05-84OR214000. This work was supported by the U. S. Department of Energy under contract DE–FG03–86ER45270.

References

[1] L. Anthony, J. K. Okamoto, and B. Fultz, Phys. Rev. Lett. **70**, 1128 (1993).

[2] L. Anthony, L. J. Nagel, J. K. Okamoto, and B. Fultz, Phys. Rev. Lett. **73**, 3034 (1994).

[3] C. Stassis, F. X. Kayser, C.-K. Loong, and D. Arch, Phys. Rev. B **24**, 3048 (1981).

[4] J. S. C. Jang and C. C. Koch, J. Mater. Res. **5**, 498 (1990).

[5] T. Nasu, C. C. Koch, A. M. Edwards, D. E. Sayers, J. Non-Crystalline Solids **150**, 491 (1992).

[6] S. R. Harris, D. H. Pearson, C. M. Garland, and B. Fultz, J. Mater. Res. **6**, 2019 (1991).

[7] A. R. Yavari, Acta Metall. Mater. **41**, 1391 (1993).

[8] M. D. Baró, S. Suriñach, J. Malagelada, M. T. Clavaguera-Mora, S. Gialanella, and R. W. Cahn, Acta Metall. Mater. **41**, 1065 (1993).

[9] B. Hennion, private communication.

[10] G. Kostorz and S. W. Lovesey in Treatise on Materials Science and Technology Vol. 15 Neutron Scattering, G. Kostorz, ed. (Academic Press: New York, 1979), 1.

[11] F. W. de Wette and A. Rahman, Phys. Rev. **176**, 784 (1968).

[12] K.-H. Hellwege (editor in chief), Landolt-Börnstein: Numerical Data and Functional Relationships in Science and Technology, (Springer-Verlag: Berlin, 1981), Volume III/13a.

[13] This concept is illustrated in P. Dean, Rev. Mod. Phys. **44**, 127 (1972).

[14] V. F. Sears, Phys. Rev. A **7**, 340 (1973).

[15] J.-B. Suck and H. Rudin in Glassy Metals II, H. Beck and H.-J. Güntherodt (Springer-Verlag: Berlin 1983), Chapter 7.

[16] D. D. Klug, E. Whalley, E. C. Svensson, J. H. Root, and V. F. Sears, Phys. Rev. B **44**, 841 (1991).

[17] J. Chevrier, J. B. Suck, M. Perroux, and J. J. Caponi, Phys. Rev. Lett. **61**, 554 (1988).

[18] C.-K. Loong, P. Vashishta, R. K. Kalia, W. Jin, M. H. Degani, D. G. Hinks, D. L. Price, J. D. Jorgensen, B. Dabrowski, A. W. Mitchell, D. R. Richards, and Y. Zheng, Phys. Rev. B **45**, 8052 (1992).

[19] J. Chevrier, J. B. Suck, J. C. Lasjanunias, M. Perroux, and J. J. Caponi, Phys. Rev. B **49**, 961 (1994).

Chapter Six Cu_3Au

6.1 Introduction

The fcc - $L1_2$ transformation in the alloy Cu_3Au (the $L1_2$ structure is shown in Figure 5.2) has been an archetype for metallurgical studies of order-disorder transformations, and the free energy and the phase diagram (shown in Figure 6.1) of Au-Cu have been topics for measurement and for model calculation. Such calculations have served as tests for the cluster variation method [1-4], for example. The influence of vibrational entropy on the thermodynamics of Au-Cu alloys has been largely neglected, however.

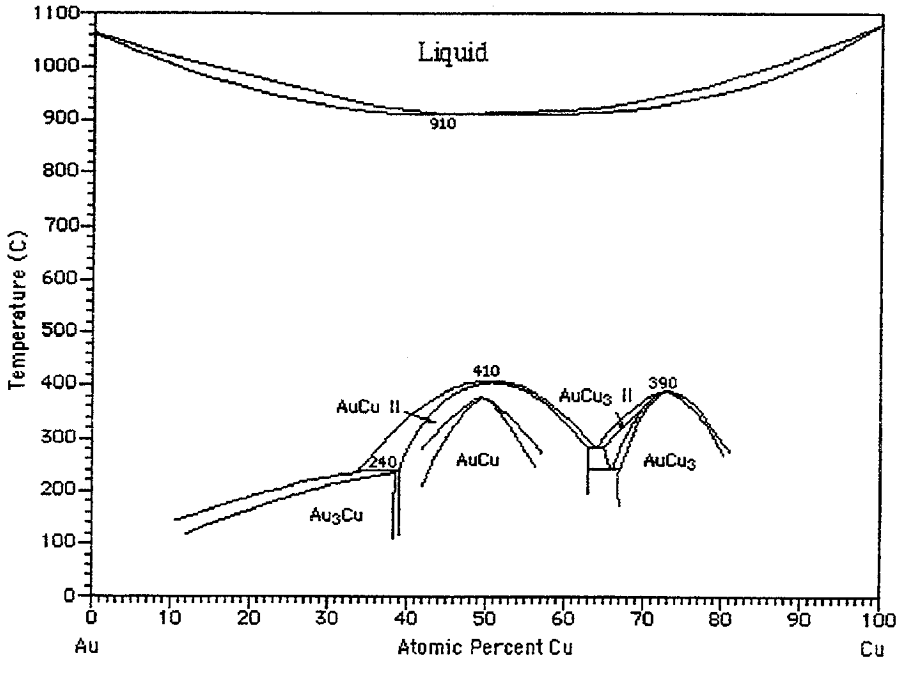

Figure 6.1 The phase diagram for the Au-Cu alloy system. From T. B. Massalski et al., Binary Alloy Phase Diagrams, 2nd ed., (Materials Park, OH: ASM Int., 1990).

The lattice dynamics of ordered and disordered Cu_3Au has a controversial early history. An electrical resistivity study by Bowen [5] reported a large increase in Debye temperature, θ, from 175 K to 197 K upon ordering. With a Debye model, this can be converted into a difference in vibrational entropy at high temperatures as:

$$\Delta S_{vib} \equiv S^{dis} - S^{ord} \approx 3\, k_B \ln\left(\frac{\theta_{ord}}{\theta_{dis}}\right) \quad , \qquad 6.1$$

from which we obtain a ΔS_{vib} of 0.355 k_B/atom. This large value of ΔS_{vib} is comparable to the entire entropy of the order-disorder transformation in Cu_3Au, which is about 0.40 k_B/atom [6]. After Bowen's result, however, Flinn, McManus and Rayne [7] performed careful measurements of elastic constants for ordered and disordered Cu_3Au, and obtained Debye temperatures of 283.8 K for the ordered alloy, and 281.6 K for the disordered alloy, so, with Equation 6.1, ΔS_{vib} would be a mere 0.023 k_B/atom. Debye-Waller factors for Cu_3Au were assessed carefully by Fox [8], using some arguments of Shirley and Fisher [9]. Surprisingly, the x-ray Debye-Waller factors [10-13] showed a much higher Debye temperature for disordered than ordered Cu_3Au: 279 K and 222 K, respectively. This leads to a large vibrational entropy difference, $\Delta S_{vib} = 3k_B \ln(222\text{ K}/279\text{ K}) = -0.69$ k_B/atom, with the vibrational entropy of the ordered alloy being larger. The errors of these x-ray Debye temperatures are large enough so that the difference in vibrational entropy could be zero, however.

Following coherent inelastic neutron scattering measurements by Hallman [14], phonon dispersion curves along high symmetry directions were measured for single crystals of both disordered and ordered Cu_3Au by Katano, Iizumi and Noda [15]. They fit their results to calculations with a Born–von Kármán model, and published a set of force constants for both states of order. More recently, Cleri and Rosato [16] calculated interatomic force constants with a tight binding method. They used their force constants in a Born–von Kármán model to obtain $\Delta S_{vib} = 0.12\ k_B/\text{atom}$.

Our differential calorimetry equipment provides its best data only for temperatures above 70 K. This is a problem for measurements on Cu_3Au, which has a relatively low Debye temperature. Nevertheless, in the present work we report measurements of $\Delta C_p(T)$ over a sufficient range in temperature so that other knowledge of lattice dynamics can be used to extrapolate ΔC_p to $T = 0$. Furthermore, measurements of $C_p(T)$ for disordered and ordered Cu_3Au to 20 K were reported by Hultgren, Desai, Hawkins, Gleiser and Kelley [17]. While these data are inadequate for the determination of $\Delta S_{vib}(T)$, they are helpful for the analysis of our data.

6.2 Samples and Experiment

Our Cu_3Au was the same material used in a previous study by Schwartz and Cohen [11]. After the material was rolled to one millimeter thickness, two 6.3 mm disks were punched from the sheet. The two samples were matched in mass, and disordered by sealing them in an evacuated quartz glass ampoule and quenching from 700 °C into an iced brine bath. To obtain $L1_2$ order, one sample was sealed in an evacuated borosilicate glass ampoule and annealed at 375 °C for three days, then the temperature was decreased by

30 °C every fourth day until the final holding temperature of 285 °C was reached. The sample was then cooled in the furnace. Strong x-ray superlattice diffractions were measured from the annealed sample, indicating a long-range order parameter of close to unity. Chemical compositions and chemical homogeneities were measured with a JEOL Superprobe 733 electron microprobe. The overall composition of the ingot was found to be close to stoichiometric, but there were compositional differences between the two samples of about 0.3 at. %.

Low-temperature heat capacity measurements employed a Perkin-Elmer DSC-4 differential scanning calorimeter (DSC) that had been modified by installing its sample head in a liquid helium dewar. Masses (about 300 mg) of the ordered and disordered alloys were matched to 0.1 mg accuracies and placed in the two sample pans of the DSC. Heat capacity measurements comprised pairs of runs, with the two samples interchanged in their sample pans between runs. The difference in heat capacities of the two samples was obtained from the difference of these two sets of runs. To test reproducibility, we obtained ten matched pairs of runs with liquid nitrogen, and three matched pairs with liquid helium as the cryogen. To counteract instrumental drift, runs comprised two pairs of scans over temperature intervals of 30 K, which typically overlap by 10 K. Scans were collected at 5, 10, and 20 K min^{-1}. Because the masses of Cu and Au are very different, the 0.3 at. % composition difference of the two samples caused the Cu-rich sample to have more atoms and a larger heat capacity. This problem was overcome by interchanging the heat treatments of the two specimens, and doing two sets of calorimetry measurements. Our final data were corrected for the mass difference of the two samples. A measurement was also performed with the ordered sample alone to confirm that its heat capacity was in reasonable agreement with the results of [17].

6.3 Results and Discussion

Averaged results from the calorimetry measurements are presented in Figure 6.2. The sign of the data is positive, showing that the disordered state of Cu3Au has the larger heat capacity. To provide the integral of Equation 3.1 with the missing low and high temperature contributions, the data of Figure 6.2. were fit to a difference of two Debye functions with θ_{ord} constrained to be 270 K, which is a good approximation to the data of [17]. The fit provided θ_{dis} = 259 K, so with Equation 3.1. we obtain ΔS_{vib} = 0.12 k_B/atom at high temperatures.

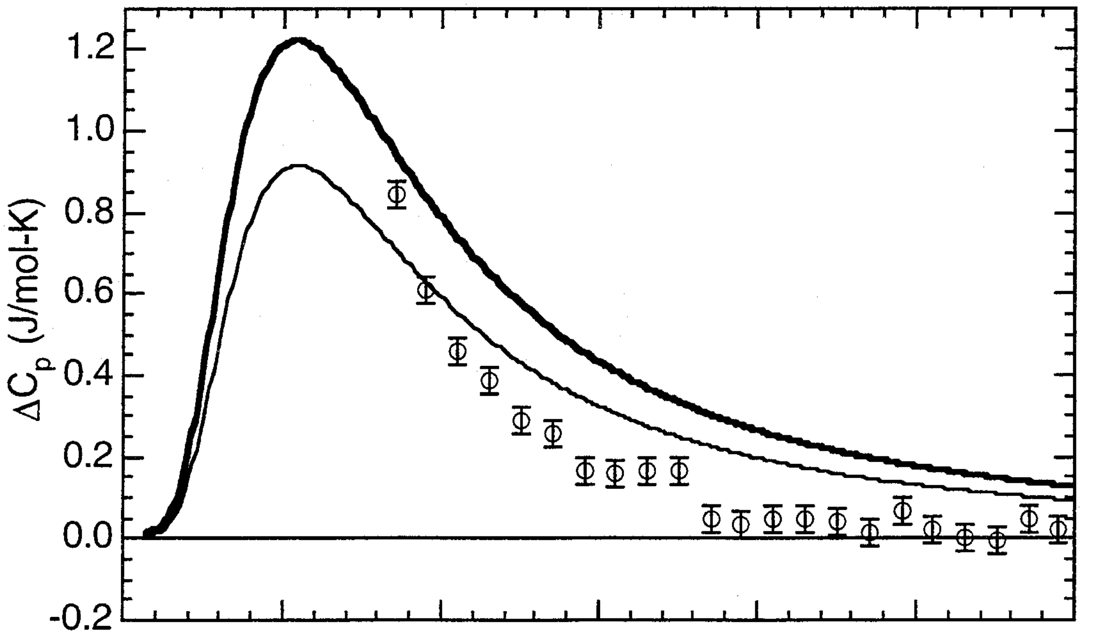

Figure 6.2 Difference between the heat capacities of disordered and ordered samples of Cu3Au–the circles are the experimental data and the lines are described in the text.

We employed a Born–von Kármán model to calculate the phonon densities of states (DOS) using the force constants of [15]. The dynamical matrix was diagonalized for about 10^6 values of $\mathbf{k}$ in the first Brillouin zone, and histogram binning of the eigenfrequencies was used to obtain the phonon DOS $g(\nu)$. These phonon DOS curves for the disordered and ordered alloys, $g^{dis}(\nu)$ and $g^{ord}(\nu)$, are presented in Figure 6.3. The difference in lattice heat capacity was obtained as:

$$\Delta C_V(T) = 3Nk_B \int_0^\infty \left(g^D(\nu) - g^O(\nu)\right) \left(\frac{h\nu}{k_BT}\right)^2 \frac{\exp\left(\frac{h\nu}{k_BT}\right)}{\left(\exp\left(\frac{h\nu}{k_BT}\right) - 1\right)^2} \, d\nu \quad . \quad 6.2$$

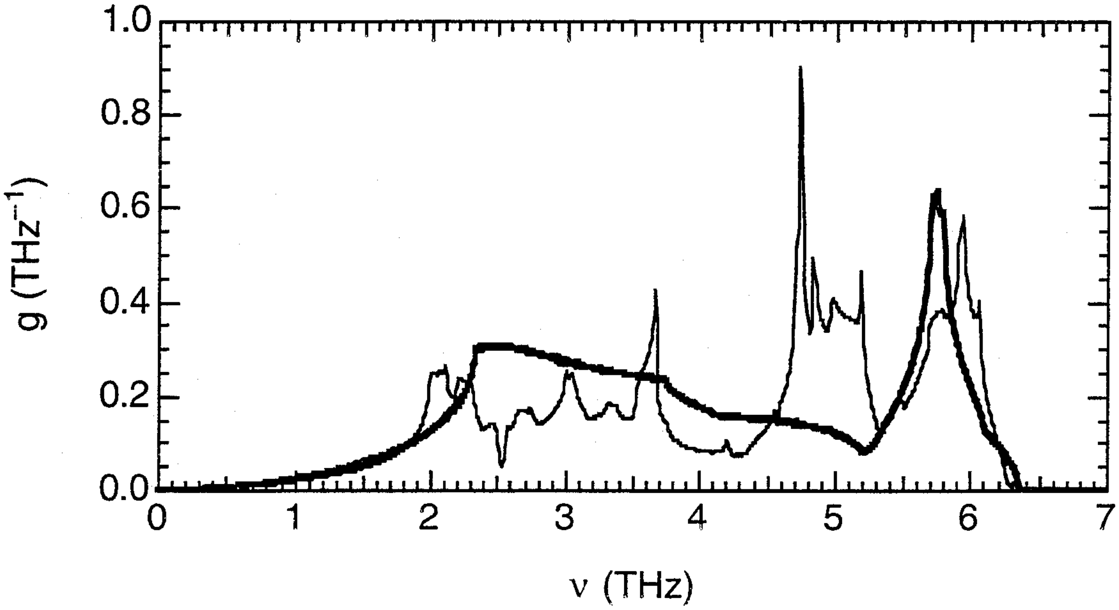

Figure 6.3 Phonon DOS of Cu_3Au with the $L1_2$ ordered structure (thin line) and as a disordered fcc solid solution (thick line), calculated with the Born-von Karman model using the force constants of [15].

In Figure 6.2, the thin line is the calculated curve for $\Delta C_V(T)$, which is the lattice heat capacity within the harmonic approximation. We believe the harmonic approximation to be mostly reliable. (If ΔS_{vib} were affected by anharmonic contributions, the measured $\Delta C_p(T)$ would deviate from zero at high temperatures, and our experimental data show that it does not. Furthermore, Touloukian [18] reports only a modest difference in the thermal expansion coefficients of ordered and disordered Cu_3Au.) Using the calculated curve for $\Delta C_V(T)$ gives ΔS_{vib} = 0.232 k_B/atom in the high temperature limit. The calculated $\Delta C_V(T)$ seems too large, however. We believe this overestimation originates with the use by [15] of a virtual crystal model for fitting the phonon dispersion curves of the disordered alloy. By scaling the calculated curve for $\Delta C_V(T)$ downwards by a factor of 0.6, we obtained the best fit to our experimental data of $\Delta C_p(T)$ when all data points were weighted equally (this is the thick curve in Figure 6.2). This scaled $\Delta C_V(T)$ provides ΔS_{vib} = 0.14 k_B/atom in the high temperature limit. Owing to our uncertainties in the modeling and fitting, we conservatively assign error bars to our result for ΔS_{vib} of ± 0.05 k_B/atom. This error is about three times larger than expected from the run-to-run variations of our calorimetry measurements.

The salient difference between the phonon DOS curves of ordered and disordered Cu_3Au is the appearance of a strong peak at 5 THz in the phonon DOS of the ordered alloy. This peak accounts for about 1/4 of the phonon modes. With this intensity at 5 THz in the ordered alloy, with respect to the disordered alloy there is a corresponding loss of intensity in the phonon DOS over the frequency range from 2.5 to 4.5 THz. If we approximate this change as a change in frequency of 1/4 of the phonon modes from 3.5 to 5 THz, we can use Equation 6.1. to obtain $\Delta S_{vib} = 3\ k_B \frac{1}{4}\ \ln(5\ \text{THz}/3.5\ \text{THz}) = 0.26$ k_B/atom. This compares well to the 0.232 k_B/atom calculated with the phonon DOS curves. These estimates of ΔS_{vib} are much larger than are obtained from the elastic constant measurements of [7], and from the calorimetry measurements by Rayne [19] at temperatures below 4.2 K. These previous low temperature results would not be sensitive to differences in the high frequency vibrational modes of the disordered and ordered alloys, however.

By examining the eigenvectors of the dynamical matrix at the high symmetry points in the Brillouin zone, we obtained the following picture of the different vibrational modes in the $L1_2$ structure. The highest frequency modes above 6 THz involved the motions of Cu atoms, primarily in the plane of their cube faces, with opposing movements of Au atoms. These motions are controlled by the largest first nearest neighbor (1nn) force constants. Although Cu atoms have 1nn Cu atoms, few of the highest frequency modes near 6 THz involved exclusively the motions of Cu atoms against 1nn Cu atoms. These Cu-Cu motions were instead found primarily in the modes around 5 THz. The phonon partial DOS curves of Figure 6.4 show that for the modes at 5 THz in the ordered alloy, the kinetic energy is almost entirely in the motion of Cu atoms. To seek relationships between the phonon modes and the structure of the ordered alloy, we perturbed the force constants of [15] and recalculated the phonon DOS curves. We found that the force constants involving the more distant pairs of atoms had little effect on the higher frequency phonons. The strongest effects on the 5 THz peak in the phonon DOS were obtained by perturbing the force constants involving 1nn pairs of atoms, especially $C^{\text{Cu-Cu}}_{1zz}$, $C^{\text{Au-Cu}}_{1xx}$ and $C^{\text{Cu-Cu}}_{1xx}$. We noticed that perturbations in the weak force constant $C^{\text{Cu-Cu}}_{1zz}$ affected strongly the peak in the phonon DOS at 5 THz, whereas the peak at 6 THz was largely unaffected.

Examining the force constants of [15], we note that the condition for axially-symmetric 1nn force constants, $C_{1xx} - C_{1xy} = C_{1zz}$, is reasonably well satisfied for both Au-Cu pairs and Cu-Cu pairs in the ordered alloy, and for 1nn pairs in the disordered alloy [14, 15]. Furthermore, the components $C^{\text{Au-Cu}}_{1zz}$ are rather small, indicating that the dominant forces between Au-Cu 1nn pairs are radial. This suggests the following intuitive picture of the lattice dynamics involving the metallic radii of stiff spheres. A unit cell of the $L1_2$ structure is shown in the inset in Figure 6.4. Upon ordering, the larger Au atoms serve to separate the more abundant, but smaller Cu atoms. Figure 6.4. shows that there are rigid contacts between the 1nn Au-Cu pairs. The large force constants $C^{\text{Au-Cu}}_{1xx}$ and $C^{\text{Au-Cu}}_{1xy}$ are consistent with this stiff sphere picture. The highest frequency modes at 6 THz involve opposing movements of 1nn Au-Cu pairs, which are controlled by these large force constants. On the other hand, Figure 6.4. shows that the 1nn Cu-Cu pairs are not in rigid contact, being separated by the larger Au atoms. It is therefore not surprising that the 1nn Cu-Cu force constants are weaker. We find the vibrations involving opposing movements of only 1nn Cu-Cu pairs primarily in the band at 5 THz. We know little about the vibrational polarizations of the individual atoms in the disordered alloy at high frequencies, but we suggest that on the average they are more isotropic than in the ordered alloy. We suggest that with the development of $L1_2$ order, the directions of movement of both Cu and Au atoms are constrained and generally increased in frequency, owing to the stiff sphere contact between Au and Cu neighbors.

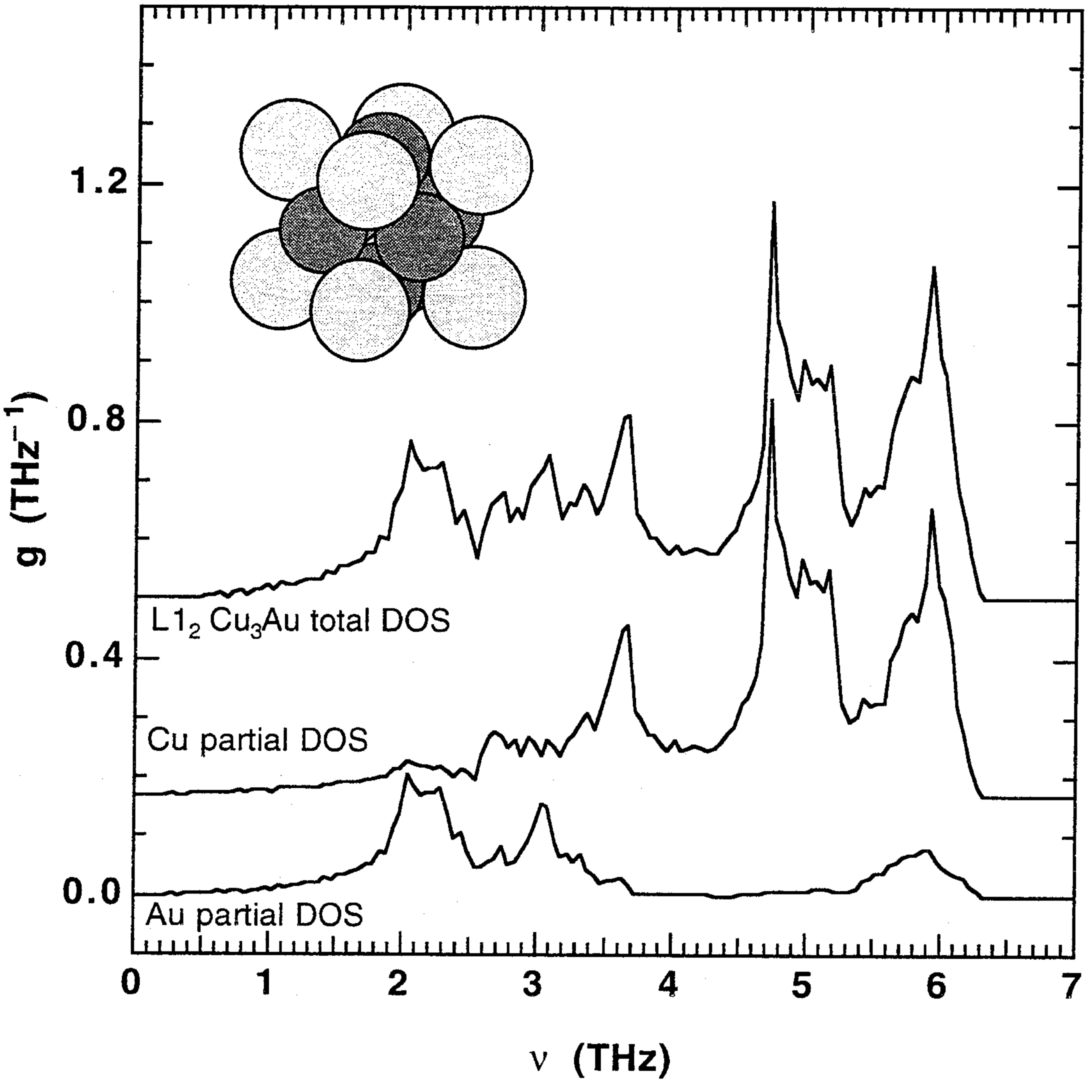

Figure 6.4 Phonon partial DOS calculations for Cu and Au in Cu$_3$Au, using force constants of [15]: partial DOS for Au atoms, obtained by weighting the amplitude of each vibrational mode by the quantity $|\varepsilon_{Au}|^2$, where ε_{Au} is the polarization vector of the Au atom in the eigenvector of the dynamical matrix; partial DOS for Cu atoms obtained in the same way; total DOS obtained by summing the two partial DOS curves. The inset shows a hard-sphere model drawn with metallic radii of 1.28 Å for Cu and 1.44 Å for Au.

6.4 Conclusions

We measured the difference in heat capacity of fcc-disordered and $L1_2$-ordered Cu_3Au over the temperature range from 70 K – 400 K. We could account semiquantitatively for the measured difference in heat capacity with a harmonic lattice heat capacity, calculated with a Born–von Kármán model using force constants from inelastic neutron scattering experiments by [15]. The calculated results were larger than the experimental results, but by scaling the calculated results to fit the measured $\Delta C_p(T)$, we obtain a difference in vibrational entropy of disordered and ordered Cu_3Au at high temperatures of (0.14 ± 0.05) k_B/atom.

The phonon DOS in the harmonic approximation is able to account semiquantitatively for the difference in vibrational entropy of disordered and ordered Cu_3Au. It is possible that the large difference in metallic radii of Cu and Au atoms influences strongly the lattice dynamics of $L1_2$ Cu_3Au by causing strong force constants for 1nn Au-Cu pairs, and weaker force constants for 1nn Cu-Cu pairs.

6.5 Acknowledgments

We are grateful to Prof. J. B. Cohen for the use of his Cu_3Au material. This work was supported by the U. S. Department of Energy under contract DE-FG03-86ER45270.

References

[1] C. M. Van Baal, Physica (Utrecht) **64**, 571 (1973).

[2] D. de Fontaine, Solid State Physics **34**, 73 (1979).

[3] T. Mohri, Acta Metall. **38**, 2455 (1990).

[4] M. Asta, G. Ceder, and D. de Fontaine, Phys. Rev. Lett. **66**, 1798 (1991).

[5] D. B. Bowen, Acta Met. **2**, 573 (1954).

[6] O. Kubaschewski and J. A. Catterall, Thermochemical Data of Alloys (Pergamon: London, 1956), p. 63.

[7] P. A. Flinn, G. M. McManus, and J. A. Rayne, J. Phys. Chem. Solids **15**, 189 (1960).

[8] A. G. Fox, Phil. Mag. B **50**, 477 (1984).

[9] C. G. Shirley and R. M. Fisher, Phil. Mag. A **39**, 91 (1979).

[10] B. Borie, Acta Cryst. **10**, 89 (1957).

[11] L. H. Schwartz and J. B. Cohen, J. Appl. Phys. **36**, 598 (1965).

[12] P. C. Gehlen and J. B. Cohen, J. Appl. Phys. **40**, 5193 (1969).

[13] P. Bardahn and J. B. Cohen, Acta Cryst. **A32**, 597 (1976).

[14] E. D. Hallman, Can. J. Phys. **52**, 2235 (1974).

[15] S. Katano, M. Iizumi, and Y. Noda, J. Phys. F: Met. Phys. **18**, 2195 (1988).

[16] F. Cleri and V. Rosato, Phil. Mag. Lett. **67**, 369 (1993).

[17] R. Hultgren, P. D. Desai, D. T. Hawkins, M. Gleiser, and K. K. Kelley, Selected Values of the Thermodynamic Properties of Binary Alloys, (ASM: Metals Park, Ohio, 1973), p. 258.

[18] Y. S. Touloukian, editor, Thermophysical Properties of Matter Vol. 12 (IFI/Plenum: New York, Thermophysical Properties Research Center, Purdue Univ., 1979), p. 520.

[19] J. A. Rayne, Phys. Rev. **108**, 649 (1957).

Chapter Seven Ni3V

7.1 Introduction

The next system I chose to examine was Ni_3V, which has an equilibrium $D0_{22}$ structure (shown in Figure 7.1). The phase diagram for the Ni-V system is shown in Figure 7.2. In the present work we used differential scanning calorimetry to measure $\Delta C_p(T)$ for two states of Ni_3V. The material was quenched from high temperature to provide a state of partial disorder, which we confirmed to have strong chemical order, but none of the tetragonality of the equilibrium $D0_{22}$ structure [1, 2]. The second state of the material was the $D0_{22}$ equilibrium structure, obtained by annealing the alloy.

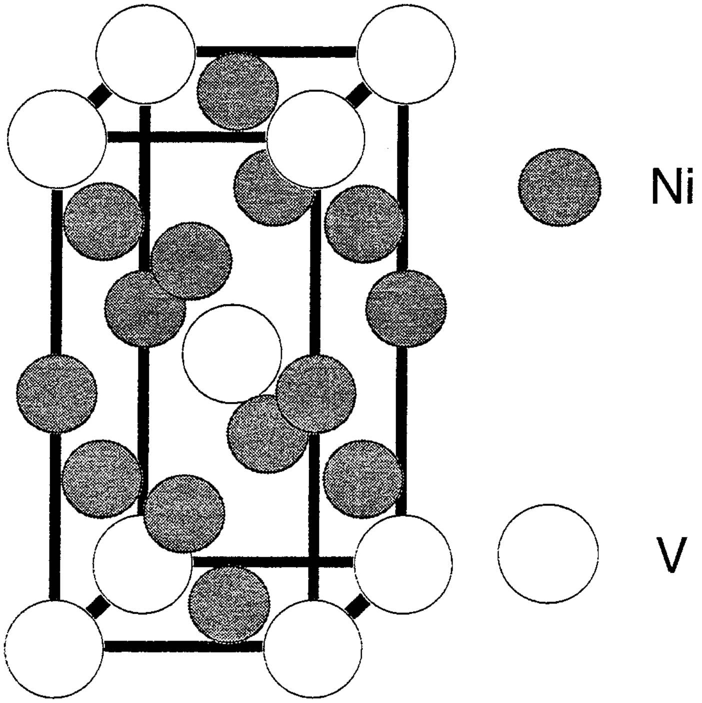

Figure 7.1 The equilibrium $D0_{22}$ structure of Ni_3V.

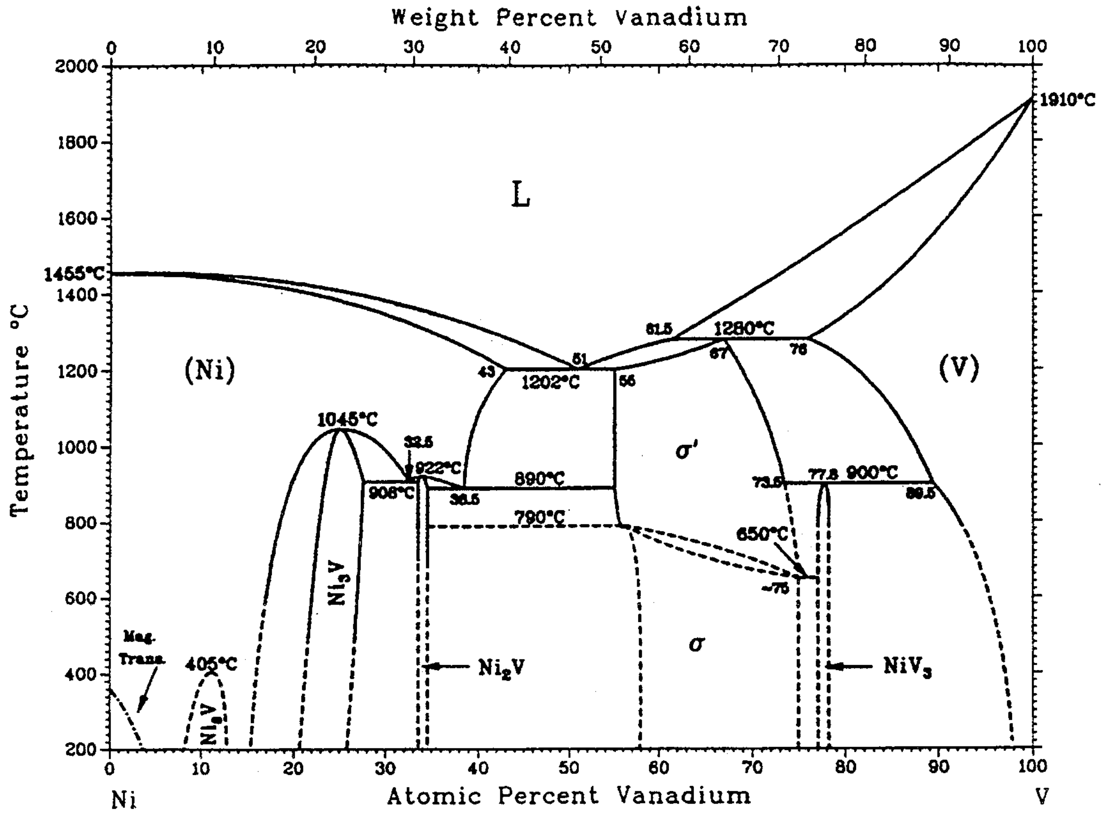

Figure 7.2 The phase diagram for the Ni-V system. Taken from T. B. Massalski, editor-in-chief, <u>Binary Alloy Phase Diagrams</u>, 2nd ed. (Materials Park, Ohio: ASM International, 1990).

In this work we have measured the phonon DOS by a more direct inelastic neutron scattering experiment, recording energy loss spectra at various values of momentum transfer, Q, to measure incoherent inelastic scattering and coherent inelastic scattering. The alloy Ni_3V proved convenient for this study, since the incoherent scattering cross sections of Ni and V are nearly identical, and the lattice dynamics of fcc Ni are well known. We obtained approximate phonon DOS curves from inelastic neutron scattering spectra measured at 11 and 300 K. The phonon DOS curves accounted for the low temperature part of the $\Delta C_p(T)$ measured by calorimetry. However, the phonon DOS curves could not account for the anharmonic part of $\Delta C_p(T)$ found at higher temperatures.

We describe a microstructural mechanism to account for the anharmonic heat capacity of ordered Ni_3V. Anisotropic thermal contractions cause elastic energy to be stored in the microstructure of the ordered alloy at low temperatures. With an increase in temperature, some of this stored elastic energy is relaxed and converted into heat, thus lowering the heat capacity of the ordered alloy. To estimate the size of this anharmonic behavior, we performed ancillary measurements of the linear coefficients of thermal expansion and Young's moduli. After correcting the measured heat capacity for this effect of microstructural storage of elastic energy, the difference in vibrational entropy of the partially-disordered and ordered Ni_3V is estimated to be: $S^{pdis} - S^{ord} = (+0.037 \pm 0.015)\ k_B/\text{atom}$ at high temperatures.

7.2 Experiment

7.2.1 Samples

Ingots of Ni_3V were prepared by the induction melting of pieces of elemental Ni (99.99+%) and V (99.9%) in an argon atmosphere. The ingots were sealed in evacuated quartz ampoules and homogenized at 1150 °C for 2 hours and cooled in the furnace. The brittle homogenized ingots were cold-rolled to break them into pieces of about 1 gram mass. These small pieces were annealed in evacuated quartz ampoules at 1150 °C, and quenched by breaking the hot ampoule in iced brine. In what follows, we refer to these materials as "partially-disordered." To form the equilibrium DO_{22} structure, some of these partially-disordered pieces were annealed at 850 °C for 2 hours and cooled in the furnace; we refer to these materials as "ordered." Samples of both materials were heated to 400 °C and analyzed for evolved hydrogen, oxygen, and nitrogen with a Hewlett-Packard 5890 gas chromatograph equipped with a thermal conductivity detector. None of these gases were detected, and detectability limits were 0.0032 wt.% for hydrogen, 0.078 wt.% for oxygen, and 0.22 wt.% for nitrogen. Chemical compositions and chemical homogeneities were measured with a JEOL Superprobe 733 electron microprobe. Averages of the composition measurements gave 25.44 at.% V for the partially-disordered alloy, and 25.39 at.% V for the ordered alloy. Composition variations within each sample were no more than about 0.1 at.%. X-ray diffractometry was performed with an Inel CPS–120 diffractometer using Co Kα radiation. An Al filter was used in front of the large-angle position-sensitive detector to suppress V Kα fluorescence.

7.2.2 Calorimetry

Low-temperature heat capacity measurements employed a Perkin-Elmer DSC-4 differential scanning calorimeter (DSC) that had been modified by installing its sample head in a liquid helium dewar. Masses (about 300 mg) of the partially-disordered and ordered alloys were matched to 0.1 mg accuracy and placed in the two sample pans of the DSC. Heat capacity measurements comprised pairs of runs, with the two samples interchanged in their sample pans between runs. The difference in heat capacities of the two samples was obtained from the difference of these two sets of runs. To test reproducibility, we obtained nine matched pairs of runs with liquid nitrogen, and two matched pairs with liquid helium as the cryogen. To counteract instrumental drift, runs comprised two pairs of scans over temperature intervals of 30 K, which typically overlapped by 10 K. Scans were performed at 10 and 20 K min^{-1}. A measurement was also performed with the ordered sample alone to determine approximately its Debye temperature. Thermal expansion measurements were performed over a temperature range from 50 °C to 275 °C using a Perkin-Elmer TMA7.

7.2.3 Ultrasonic Wave Velocity Measurements

Efforts were made to measure ultrasonically the longitudinal and shear wave velocities in the partially-disordered and ordered states of Ni_3V. We used a Panametrics 10 MHz ultrasonic longitudinal wave transducer and a Panametrics 5 MHz ultrasonic shear wave transducer, whose outputs were passed through a Panametrics Model 5052UA ultrasonic analyzer to a Hewlett Packard 54510A oscilloscope sampling at 1 GHz. Two sets of samples were used; one set of cylinders was 7 mm diameter and 1 mm in height, while the second set of cylinders was 7 mm diameter and 4 mm in height. The top and bottom faces of the cylinders were accurately cut parallel and then polished. Successful measurements of the longitudinal and shear wave speeds in Cu_3Au were made using similar samples from previous calorimetry measurements [3]. We deduced bulk moduli at room temperature of 18.88×10^{10} Pa for $L1_2$-ordered Cu_3Au, and 18.70×10^{10} Pa for chemically-disordered fcc Cu_3Au, in good agreement with previous results [4]. However, none of the Ni_3V samples showed a pulse-echo pattern, so measurements were impossible. The samples of Ni_3V evidently showed a strong ultrasonic attenuation, perhaps because inhomogeneous internal stresses caused scattering of the ultrasonic waves.

7.2.4 Compression Testing

To measure Young's moduli, compression tests were performed using an Instron Model 4204 load frame. A cylindrical sample of 0.55 cm diameter and 1.9 cm height was machined from an induction-melted ingot of Ni_3V, and was heat-treated to produce the partially-disordered state. After compression testing, the same sample was annealed for 2 hours at 850 °C and cooled in the furnace in order to achieve the ordered state, and the compression tests were repeated. The crosshead speed was 0.05 cm/min, and the extension of the sample was measured using a strain-gauge extensometer. We attempted to perform the compression tests in the elastic regime of the material. The yield stress at room temperature for ordered Ni_3V has been reported to be 900 MPa [2]. Our samples were loaded to only 270 MPa, and we ensured that there was no reduction in slope of the stress-strain curves at the highest loads. Several load-unload cycles were performed on each sample. We also performed compression tests on a similar sample of mild steel to confirm that we obtained a reasonable Young's modulus and no hysteresis in its stress-strain curve.

7.2.5 Neutron Scattering and Diffraction

Samples of the partially-disordered and ordered alloys, each about 50 grams, were placed in thin-walled aluminum cans and mounted in a closed-cycle helium refrigerator on the goniometer of the HB2 triple axis spectrometer at the High Flux Isotope Reactor at the Oak Ridge National Laboratory. Measurements on our two materials were performed at both 11 K and 300 K. The spectrometer was operated in constant-Q mode with the fixed final energy, E_f, of 14.8 meV. The energy loss spectra were made by scanning the incident energy from 14.8 meV to 74.8 meV. The neutron flux from the monochromator was monitored with a fission detector, which was used to control the counting time for each data point. The incident beam on the pyrolytic graphite monochromator crystal had a collimation of 110′, and 40′ Soller slits were used between the monochromator and the sample. Pyrolytic graphite filters placed after the sample were used to attenuate the 1/2 and 1/3 contamination. The filtered beam passed through 40′ slits before the pyrolytic graphite analyzer crystal. Following the analyzer, 70′ Soller slits were used before the ^{3}He detector. With this arrangement, the energy resolution varied between 0.9 and 2 meV, depending on the energy transfer and the slope of the phonon dispersion surface. Spectra from each specimen were obtained at four values of Q: 3.48, 3.73, 3.98 and 4.23 Å^{-1}.

7.3 Results

7.3.1 Structure

Very weak, if any, superlattice diffraction lines were observed in the Co Ka x-ray diffraction patterns (Figure 7.3) from any samples, but the x-ray form factors are not strongly different for Ni and V atoms. On the other hand, neutron diffraction (Figure 7.3) showed strong superlattice diffraction peaks from both the quenched sample and the annealed sample (e.g., the (002), (101), (110) peaks at q = 1.74, 1.98, 2.51 Å^{-1}). From calculations of the expected peak

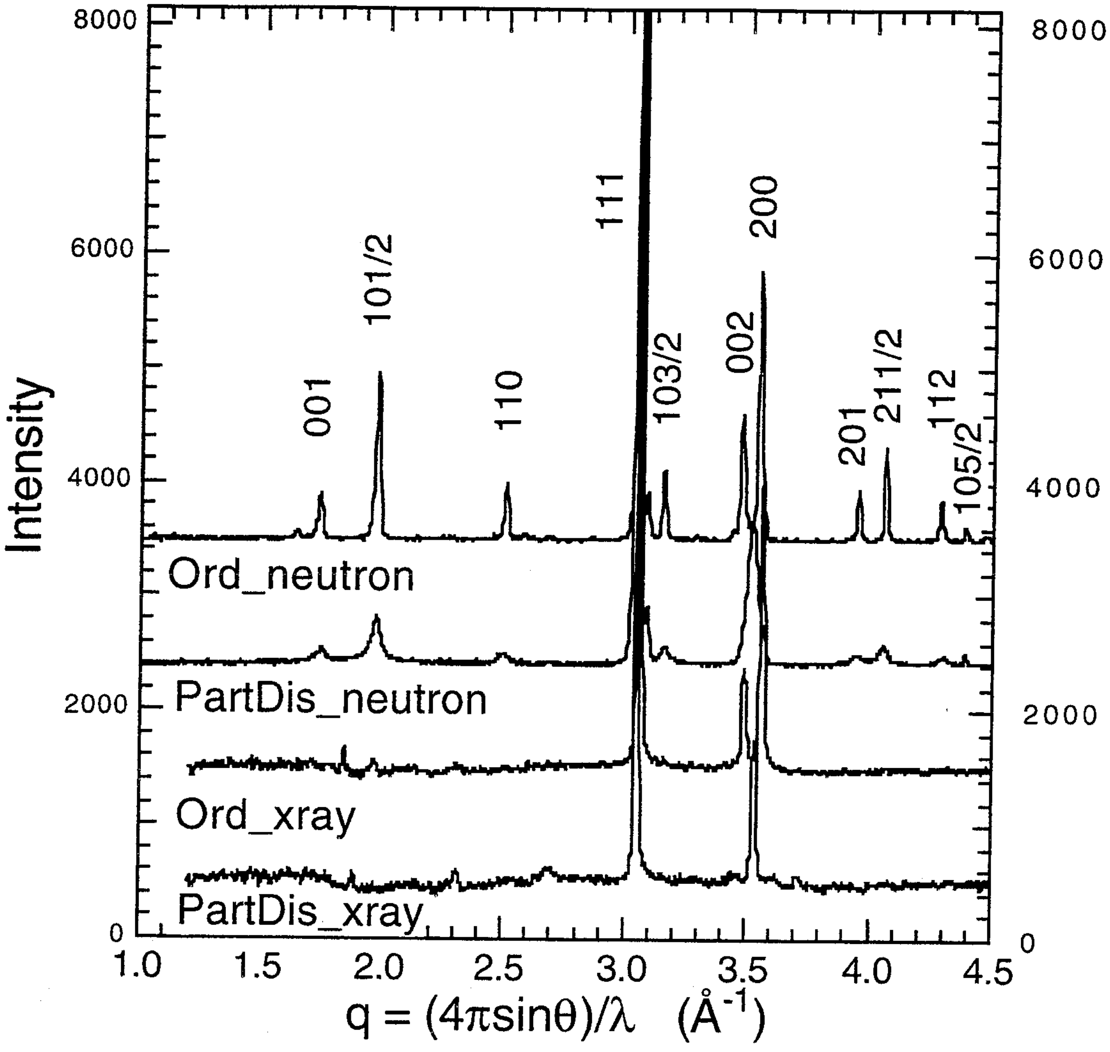

Figure 7.3 X-ray and neutron powder diffraction patterns of the partially-disordered and ordered Ni3V materials. Some weak diffractions from surface oxides are seen in the x-ray diffraction patterns, but not in the neutron data.

intensities [5], we found the superlattice peak intensities from the ordered alloy to be consistent with a long-range order (LRO) parameter close to one. The superlattice peaks from the quenched samples were broadened, but had 85 to 90% of the areas of the superlattice peaks from the annealed sample. The Bragg-Williams LRO parameter of the quenched alloy was between 0.90 and 0.95. X-ray and neutron powder diffractometry showed tetragonality in the annealed specimen that was characteristic of the $D0_{22}$ structure. Figure 7.3 shows that the ratio of the intensities of the (004) and (200), (020) diffractions (at $q = 3.48$ and 3.55 Å^{-1}) are 1:2, as expected for the powder-averaged intensities of these diffractions. The as-quenched specimens showed no tetragonality, and their reasonably sharp diffraction peaks were characteristic of an fcc structure. This is consistent with previous results of transmission electron microscopy studies that showed a "tweed" microstructure of quenched Ni_3V, as shown in Figure 7.4, characterized by internal strains, but no regions that are distinctly tetragonal [1, 6, 7]. Since the quenched sample had a high degree of the chemical order of the $D0_{22}$ structure, but none of the long-range tetragonality, we call it "partially-disordered."

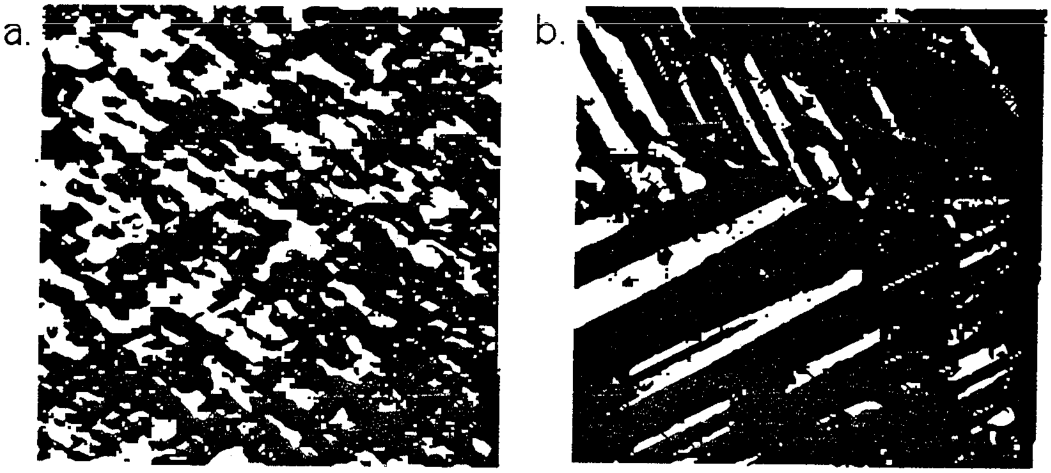

Figure 7.4 The "tweed" microstructure of Ni3V is shown in a., while the twinned tetragonal structure is shown in b. In a., the scale is 1.5 cm is 0.3 μm, while in b., 1.0 cm is 0.3 μm. These micrographs came from L. E. Tanner, Phys. Stat. Sol. **30**, 685 (1968).

7.3.2 Calorimetry

Averaged results from the differential calorimetry measurements are presented in Figure 7.5. The sign of the data is positive, showing that Ni_3V has a larger heat capacity in the partially-disordered state than in the ordered state. The heat capacity was also measured with an ordered sample alone.

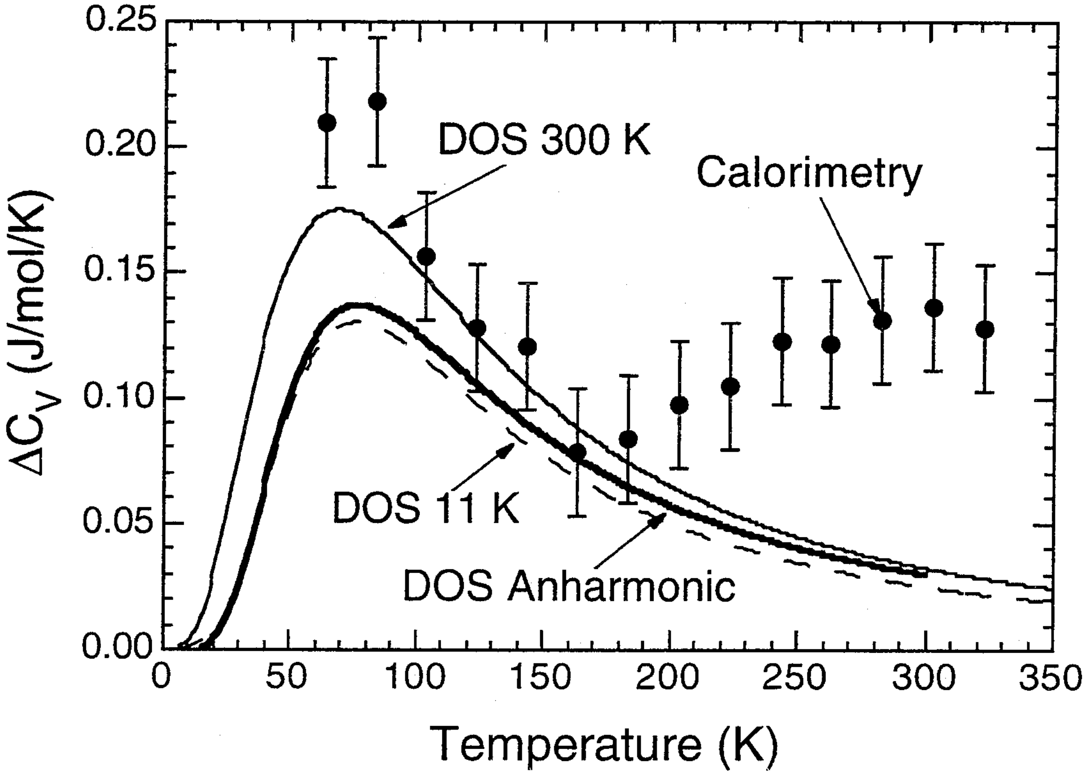

Figure 7.5 Differential heat capacities. Points: averages of scans with differential calorimetry of the difference in heat capacity of partially-disordered and ordered Ni_3V materials (sign is partially-disordered minus ordered). Error bars indicate variations between different runs. Lines: calculations as described in the text.

From this experiment the Debye temperature was determined to be approximately 365 K. (This could be inaccurate, since data were not obtained much below 100 K, but it showed reasonable agreement with the heat capacity calculated with the phonon DOS curves as described below, and should be adequate for our need to account for the low temperature part of $\Delta C_p(T)$ for use in Equation 3.1.) Using this Debye temperature of 365 K for the ordered sample, the data of Figure 7.5 could be best fit at temperatures below 160 K with a Debye temperature of 360 K for the partially-disordered sample. At high temperatures, these Debye temperatures provide a larger vibrational entropy for the partially-disordered than the ordered alloy, ΔS_{vib}, of:

$$\Delta S_{vib} = 3 k_B \ln\left(\frac{365}{360}\right) = 0.041\ k_B/\text{atom} \quad . \qquad 7.1$$

7.3.3 Elastic Moduli, Thermal Expansion Coefficients, Grüneisen Constants

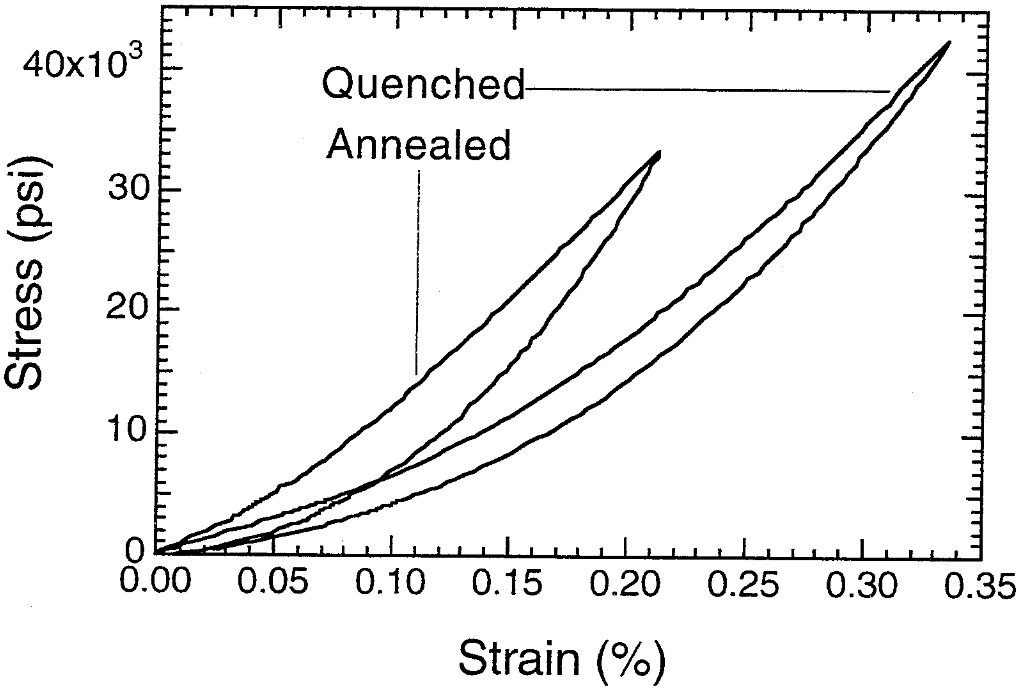

Figure 7.6 Engineering stress-strain curves from compression tests of partially-disordered and ordered Ni_3V. These curves were the fifth load-unload cycles of the materials.

The stress-strain curves of Figure 7.6 show considerable hysteresis. For determining the Young's modulus, we used the unloading curve at stresses slightly below the peak stress of the test. We expect this slope to be least affected by internal processes contributing to hysteresis, and more representative of the elastic response. In support of this expectation, we found that the unloading curve was more reproducible than the loading curve, and we found that the Young's modulus of the ordered material was in good agreement with that of François et al. [2]. Young's moduli are presented in Table 7.1, together with linear coefficients of thermal expansion.

Table 7.1. Measured physical properties of partially-disordered and ordered Ni_3V.

State of Ni_3V	Young's modulus	α (350 K)	γ (Eq. 7.2.)	γ (DOS)
partially-disordered	12.4×10^{10} Pa	10.6×10^{-6} K^{-1}	1.15	4.9
DO_{22} ordered	17.2×10^{10} Pa	10.2×10^{-6} K^{-1}	1.53	3.2

Grüneisen constants were obtained from the temperature dependence of the phonon DOS (described in Section 7.4). For the ordered alloy, for example, we rescaled in energy the 300 K phonon DOS curve by 0.95% to achieve a best match with the 11 K curve. The 300 K curve for the partially-disordered alloy matched best with the 11 K curve for a rescaling by 1.5%. Using the linear coefficients of thermal expansion in Table 7.1 with the 289 K difference between 11 and 300 K, we obtain the Grüneisen constants, γ, of 4.9 for the partially-disordered alloy and 3.2 for the ordered alloy. These values seem large, perhaps because the measured thermal contraction is an average of anisotropic constants involving different crystallographic directions. On the other hand, using the relationship:

$$\gamma = \frac{3BV\alpha}{C_V} \quad , \qquad 7.2$$

we obtain Grüneisen constants of 1.15 for the partially-disordered material and 1.53 for the ordered material. Not only are these Grüneisen constants smaller that those obtained from the phonon DOS, but their relative sizes are reversed for the two materials. The inconsistency in these Grüneisen constants may be related to the crystallographic anisotropy of Ni_3V.

7.3.4 Inelastic Neutron Scattering

The 16 inelastic scattering spectra from the two samples (partially-disordered and ordered), at two temperatures (11 K and 300 K), and four values of Q (3.48, 3.73, 3.98, 4.23 $Å^{-1}$), are presented in Figure 7.7. The strong elastic peak is seen at energies below 2 meV. At higher energy losses, the inelastic scattering shows features of the phonon DOS of the material, such as the peak from the longitudinal branch at 33 meV. In each of these spectra, the phonon DOS is significantly modified by a thermal factor and the Q-dependence of the coherent inelastic scattering. Since all spectra were obtained with the same total incident beam flux, the thermal factor is evident from the stronger scattering at 300 K than at 11 K. The Q-dependence of the coherent inelastic scattering is seen through differences in the shapes of the four spectra in each of the four graphs of Figure 7.7. Overlays of these raw data show that the inelastic loss spectra of the ordered alloy are at slightly higher energies than are spectra of the disordered alloy, and the inelastic loss spectra of both materials show some thermal softening. The next section describes our analysis of these data to extract four phonon DOS curves for the two samples, partially-disordered and ordered, at two temperatures, 11 K and 300 K.

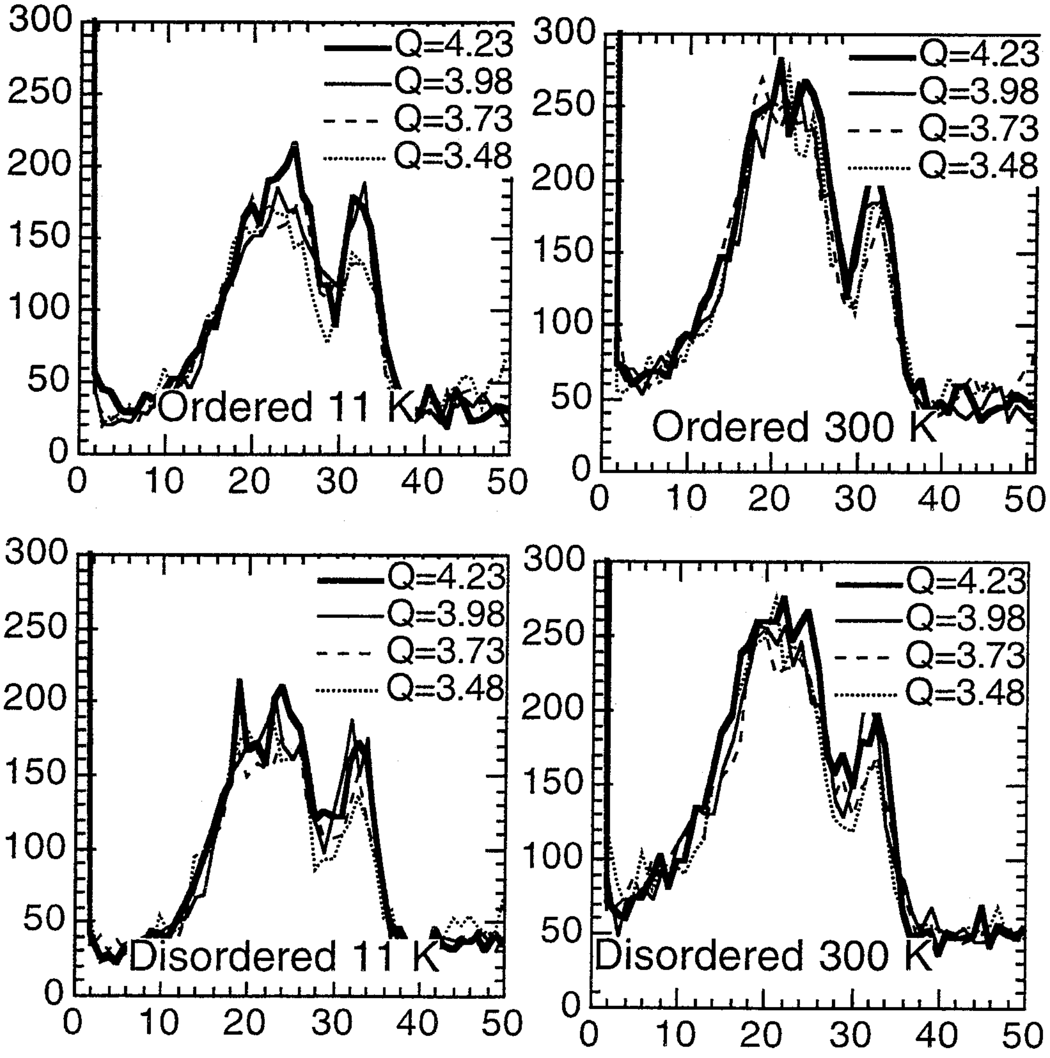

Figure 7.7 Raw neutron energy loss spectra for the partially-disordered and ordered Ni_3V powders, obtained at four values of Q and two temperatures as indicated.

7.4 Analysis of Inelastic Neutron Scattering Spectra

This section describes our method for obtaining approximate phonon DOS curves for the partially-disordered and ordered materials at temperatures of 11 and 300 K. Our method has similarities to approaches used previously [8-11]. First, a background was stripped from each spectrum. For our choices of Q and E, the background for the HB2 spectrometer is approximately constant in Q and E. We subtracted the same constant background from all eight spectra obtained at 11 K. As shown in Figure 7.7, however, the background around 40 meV was higher for the 300 K data, and we attribute this excess background to neutrons that had undergone two scatterings in the sample. The sample was taller than it was wide, so a second scattering is most likely if the first deflection of the neutron was along the vertical axis. The Φ angle of scattering from the specimen was nearly 90 degrees for energy losses around 40 meV, but only 40 degrees for the low energy part of the spectrum. The two-phonon background in our data is therefore expected to be weakest at low energies. The background for the 300 K data was approximated as a linear function that was the same at low energies as the 11 K data, but was about 50% larger at 40 meV. We calculated the inelastic incoherent scattering using the conventional multiphonon expansion [12-14]. The calculation was performed for 300 K with the phonon DOS curve of fcc Ni [8, 15, 16]. The results showed that at the relatively low values of Q and temperature of the present experiments, the inelastic scattering is strongly dominated by one-phonon processes, but the small background enhancement of the 300 K data with respect to the 11 K data was approximately consistent with the calculated two phonon scattering. Second, each spectrum was corrected by the one-phonon thermal factor, f(T), of:

$$f(T) = \varepsilon\left(1 - \exp(-\varepsilon/kT)\right) \quad . \tag{7.3}$$

All spectra were then normalized to unit area. Finally, for each specimen at each temperature, we summed all four spectra for the different values of Q. For the incoherent inelastic part of the scattering, this data processing procedure should provide the total phonon DOS, since the incoherent scattering from both Ni and V atoms are the same. The coherent inelastic scattering from Ni atoms contributes significantly to the spectra, however.

It is usually not possible to obtain an accurate phonon DOS from coherent inelastic scattering spectra of polycrystals without prior knowledge of the lattice dynamics of the material [17], and there is little such knowledge for Ni_3V. One problem occurs because Ni and V atoms have different coherent scattering cross sections. In particular, we were concerned initially that the negligible coherent scattering from V atoms will de-emphasize groups of vibrational modes having polarization eigenvectors with large components for V atoms. If such modes dominate a significant energy range, the deduced phonon DOS would be distorted in this range. High frequency optical modes should be particularly susceptible to this problem. However, were there significant differences between samples in vibrational modes involving the motion of primarily V atoms, we should be able to detect them through changes in the incoherent inelastic scattering. Furthermore, most optical modes involve some motion of Ni atoms that are neighbors of the V atoms, so these modes should also contribute to the coherent inelastic scattering. We examined carefully the spectra in Figure 7.7 and the final DOS curves of Figure 7.8 over the energy range of 25-50 meV. We found no distinct differences in the features of curves for the four sets of data. The processed phonon DOS are very similar to each other, and to the phonon DOS curve for fcc Ni [8].

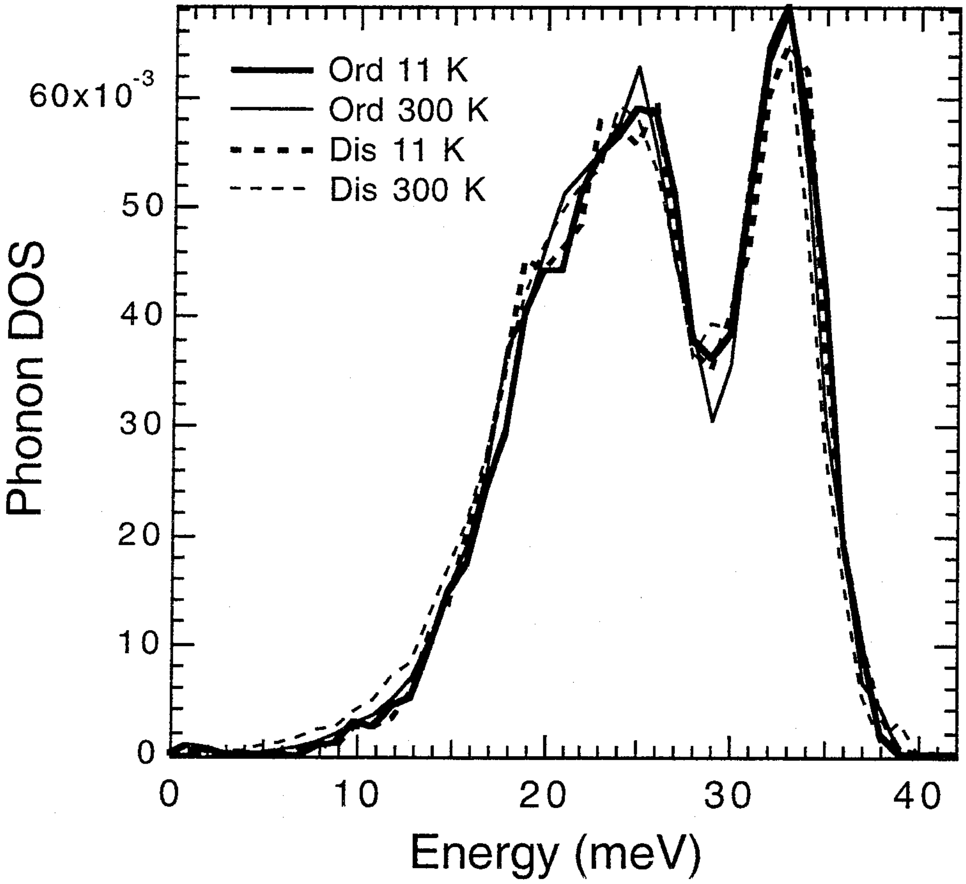

Figure 7.8 Phonon DOS obtained from the experimental data of Figure 7.7 as described in the text.

The phonon dispersion curves of fcc Ni are well-known [15, 16]. In our previous work [8], a Born - von Kármán model was used with interatomic force constants of fcc Ni to calculate the eigenfrequencies and eigenvectors of the dynamical matrix. With this information for each phonon in the first Brillouin zone, the coherent inelastic scattering was calculated by performing a crystallographic average of the dynamical structure factor intensity at explicit values of **Q** with respect to the crystallographic axes. It was shown that for fcc Ni, summing the dynamical structure factors for the four values of Q (3.48, 3.73, 3.98, 4.23 $Å^{-1}$) provides a good approximation to the phonon DOS [8]. More significantly, systematic errors in the analysis are not too important for our purposes, since our need is to identify differences in the phonon DOS curves for the different states of the material.

The phonon DOS curves presented in Figure 7.8 show no major qualitative differences, and are in fact quite similar to the curve for fcc Ni with comparable experimental resolution (Figure 3b in [8]). Owing to the excellent 0.01 meV energy accuracy and stability of the HB2 spectrometer, small energy shifts in the phonon DOS curves can be measured reliably. It is seen in Figure 7.8 that the curve for the ordered alloy at 11 K is shifted to the highest energy, and the lowest curve is for the disordered alloy at 300 K. Differences in the partially-disordered and ordered DOS curves at the same temperature are indicative of the harmonic contribution to the difference in vibrational entropy between the two materials, and the changes of these differences with temperature are indicative of anharmonic effects on the difference in vibrational entropy.

7.5 Discussion

7.5.1 Anharmonicity and Phonon DOS

Unfortunately, the temperature dependence of our g(v) is only qualitatively consistent with the Grüneisen approximation. This could be caused by errors in either our measurements or in the approximation itself. Our approach to calculating $C_p(T)$ is instead to linearly interpolate the phonon DOS curves of 11 K and 300 K, including the zero-point contribution:

$$C_p(T) = C_V(T) + \frac{3T}{T_2-T_1}\int_0^\infty [g_{T_2}(\varepsilon) - g_{T_1}(e)]\frac{\varepsilon^2}{kT^2}\frac{e^{\varepsilon/kT}}{(e^{\varepsilon/kT}-1)^2}\,d\varepsilon \qquad 7.4$$

$$+ \frac{3T}{T_2-T_1}\int_0^\infty [g_{T_2}(\varepsilon) - g_{T_1}(\varepsilon)]\frac{\varepsilon}{2}\,d\varepsilon \quad ,$$

and the temperatures are $T_2 = 300$ K and $T_1 = 11$ K. The phonon DOS at 11 K is assumed to be the same as that of zero temperature.

With Equation 1.9, we calculated the harmonic differential heat capacity, $\Delta C_V(T) \equiv C_V^{PD}(T) - C_V^{O}(T)$, from the differences in phonon DOS of the partially-disordered (PD) and ordered (O) samples. The calculation of $\Delta C_V(T)$ with the 11 K phonon DOS curves is presented as a thin dashed curve in Figure 7.5, and the calculation of $\Delta C_V(T)$ from the 300 K phonon DOS curves is presented as a thin solid curve. We believe that the differential heat capacity, $\Delta C_p(T)$, at temperatures below 160 K is described semi-quantitatively by calculations with a harmonic model using either pair of phonon DOS curves (11 K or 300 K). At temperatures greater than 160 K, however, the calculated curves are qualitatively incorrect. The $\Delta C_p(T)$ measured by calorimetry did not asymptotically approach zero, as expected in a harmonic model where the heat capacities of both states of the material approach the same Dulong-Petit limit of $3\,k_B$/atom.

With Equations 1.9 and 7.4 we calculated $C_P(T)$ for both the partially-disordered and ordered alloys, using the phonon DOS curves shown in Figure 7.8. The result for $\Delta C_P(T)$ is presented as a dark curve in Figure 7.5. At low temperatures, this $\Delta C_P(T)$ curve is much like the $\Delta C_V(T)$ curve from the 11 K phonon DOS, and near 300 K the $\Delta C_P(T)$ curve approaches the $\Delta C_V(T)$ curve from the 300 K phonon DOS. At 300 K, the anharmonic $\Delta C_P(T)$ curve lies below the harmonic $\Delta C_V(T)$ curve from the 300 K phonon DOS, however, owing to the reduction of zero point energy accompanying the softening of the phonon DOS.

Figure 7.5 shows that for temperatures greater than 160 K, there is poor agreement between the calculated anharmonic $\Delta C_P(T)$ curve and the data measured by calorimetry. Since the energy scale for the HB2 spectrometer is reliable, the heat capacities calculated with Equations 1.9 and 7.4 should be accurate, since they are integral quantities over the phonon DOS. Modifications of Equation 7.4 that started the transition from the low temperature DOS to the high temperature DOS at 160 K, for example, were also incapable of providing the large anharmonic behavior in $\Delta C_P(T)$ measured by calorimetry. We conclude that the thermal softening of the phonon DOS is not sufficiently different for the partially-disordered and ordered alloys to account for the strong anharmonic behavior of $\Delta C_P(T)$ measured by calorimetry at temperatures greater than 160 K.

7.5.2 Anharmonicity and Microstructure — Elastic Energy

A microstructural mechanism for elastic energy storage is expected in polycrystalline Ni_3V with the $D0_{22}$ structure. This mechanism, based on the tetragonal anisotropy of the thermal expansion of the ordered alloy, should provide an anharmonic contribution to $\Delta C_p(T)$. For Ni_3V with $D0_{22}$ order, it is known that the microstructure within each prior fcc crystallite consists of lenticular packets comprising lamellae of ordered domains. The domains are mutually arranged in a microtwin-type microstructure (see Figure 7.4.b) to minimize the elastic energy [1, 2, 6, 7]. Such a microstructure can be optimized to minimize elastic energy at only one temperature, however. With changes in temperature, the ordered domains expand or contract anisotropically, generating internal elastic energy owing to geometrical mismatch between the lenticular packets. The ordered domains were originally formed during the annealing and cooling from 850 °C, so we expect the microstructure was optimized for minimizing elastic energy at high temperatures. Anisotropic thermal contraction upon cooling will provide internal stresses at room temperature. Tanner showed that the tetragonality of ordered Ni_3V can vary from about 1 to 2%, depending on the thermal processing [1]. (Our ordered alloy had a tetragonality of 1.7%.) Nonequilibrium tetragonalities require the presence of internal stresses. In Tanner's work, significant strain contrast was found in transmission electron micrographs of ordered Ni_3V at room temperature, and others have reported large strain effects around Ni_3V precipitates in Ni-V alloys [6, 7]. In comparison, crystals of the disordered alloy, which have little or no tetragonality, will contract more isotropically upon cooling, so will have less internal elastic energy. We expect a difference in the heat capacities of the partially-disordered and ordered alloys owing to this microstructural difference.

We also expect this microstructural mechanism for elastic energy storage in the polycrystalline ordered alloy to affect the elastic moduli measured in tests on macroscopic specimens. We expect the measured bulk modulus, $B \equiv V\, \partial^2 E / \partial V^2$, to depend in the usual way on the energy of the crystal originating directly from the interatomic potential, E_{xtl}, but we expect an additional contribution from the elastic energy stored in the microstructure, $E_{\mu str}$:

$$B = V\left(\frac{\partial^2 E_{xtl}}{\partial V^2} + \frac{\partial^2 E_{\mu str}}{\partial V^2}\right) = B' + B'' \qquad 7.5$$

The second contribution, B", is positive at low temperatures, since by loading in compression further elastic energy is added to a microstructure that has already stored some energy during thermal contraction.

With three assumptions we can use Equation 7.5 to calculate the microstructural contribution to the heat capacity. First, because the more isotropic partially-disordered Ni_3V has nearly the same chemical order as the ordered alloy, we assume that B' is equal to the bulk modulus of the partially-disordered alloy. We also assume that the Young's modulus is the same as the bulk modulus. This is valid for isotropic materials having a Poisson's ratio of 1/3. The Poisson's ratio of microtwinned Ni_3V is reported to be 0.354 [2]. Finally, we assume that the microstructural mechanism for storage of elastic energy operates in the same way in an uniaxial compression test as in unconstrained thermal expansion. This last assumption is probably a poor one, limiting our results to an estimate of the magnitude of the microstructural heat capacity. With these assumptions, the microstructural storage of elastic energy at a temperature T will be proportional to the amount of thermal contraction from T_H where the microstructure was formed:

$$E_{\mu str} = \frac{B''V}{2}\left(\int_{T}^{T_H} 3\alpha(T')\,dT'\right)^2 \quad . \qquad 7.6$$

The heat capacity associated with this microstructural energy, $\Delta C_{p\mu str}(T)$, is:

$$\Delta C_{p\mu str}(T) = \left.\frac{\partial E_{\mu str}}{\partial T}\right)_p \quad . \qquad 7.7$$

When α is independent of temperature, we obtain:

$$\Delta C_{p\mu str}(T) = 9\,B''\,V\,\alpha\,(\,T - T_H\,) \quad . \qquad 7.8$$

The sign of $\Delta C_{p\mu str}(T)$ is negative for $T < T_H$, which is the range of all our measurements. Assuming that T_H = 1123 K, at T = 300 K we obtain $\Delta C_{p\mu str}(T)$ = 0.27 J/mol/K. This microstructural contribution to the heat capacity seems about twice as large as needed to account for the difference in the calorimetry data and calculated curves of Figure 7.5, but it does show that a large microstructural contribution to the heat capacity is plausible. The discrepancy suggests that the microstructural mechanism for storage of elastic energy operates more effectively during uniaxial compression than in thermal expansion.

Although the prefactors in Equations 7.6 and 7.8 are unreliable, we can still estimate the temperature dependence of $\Delta C_{p\mu str}(T)$. Using Equation 7.2

to provide the temperature dependence for $\alpha(T)$ through the temperature dependence of $C_V(T)$, we obtain from Equations 7.6 and 7.8:

$$\Delta C_{p\mu str}(T) = \frac{B''\gamma^2}{B'^2 V} C_V(T) \left(E_{ph}(T) - E_{ph}(T_H)\right) \quad . \tag{7.9}$$

To evaluate the temperature dependence of Equation 7.9, we used the phonon DOS of the ordered alloy, measured at 300 K, to provide C_V (Equation 1.9) and E_{ph} (Equation 1.5). Using the temperature dependence of Equation 7.9, we scaled the prefactor of $\Delta C_{p\mu str}(T)$ to account for the difference at 300 K

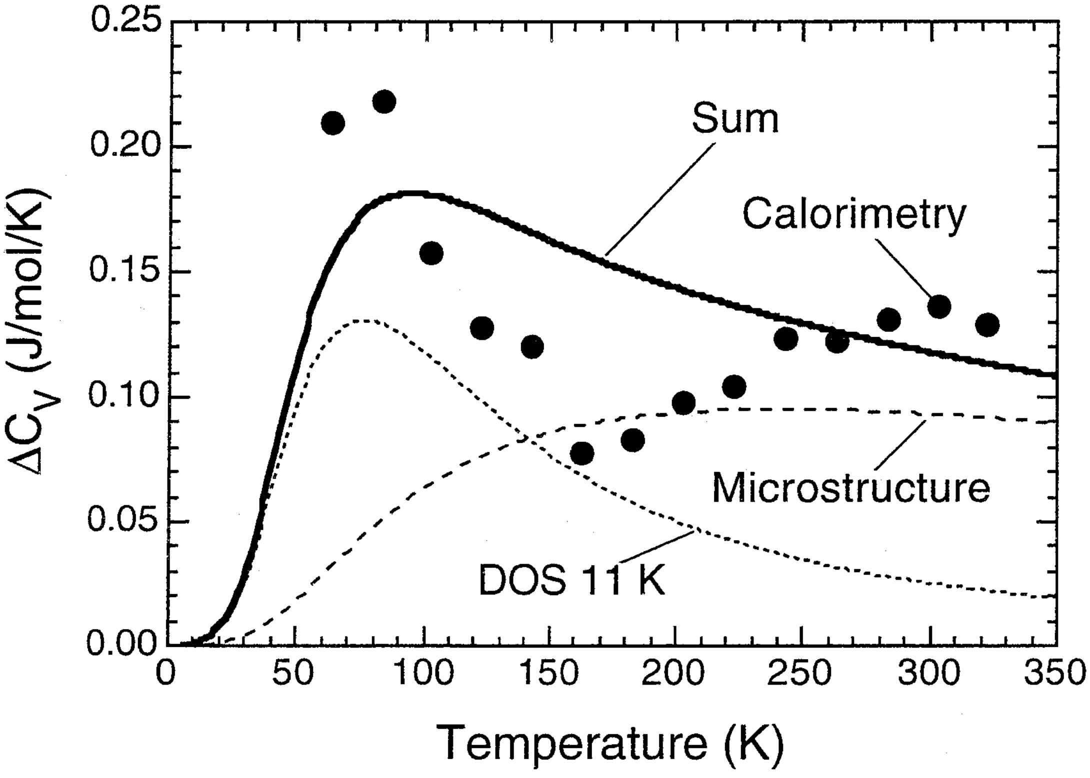

Figure 7.9 Differential heat capacities. Curve "DOS 11 K" and points "Calorimetry" are as presented in Figure 7.5. Curve "Microstructure" is calculated with Equation 7.9 in the text. Curve "Sum" is the sum of curves "DOS 11 K" and "Microstructure."

of the heat capacity data of Figure 7.5 labeled "Calorimetry" and the curve "DOS Anh." (This is equivalent to setting $\gamma = 1.06$, which is probably low because the microstructural mechanism for energy storage is more effective in an uniaxial compression test than in thermal expansion.) The full temperature dependence of $\Delta C_{p\mu str}(T)$ is presented in Figure 7.9 as the curve labeled "Microstructure." The integral of $\Delta C_{p\mu str}(T)$ from 0 to 1123 K is 60 J/mole, which is our estimate of the elastic energy stored in the microstructure of the ordered alloy at low temperatures. Adding this $\Delta C_{p\mu str}(T)$ to the $\Delta C_V(T)$ from the phonon DOS curves measured at 11 K provides the thick solid curve in Figure 7.9 labeled "Sum." The agreement with the heat capacity data measured by calorimetry is much better than calculated with the phonon DOS alone, improving the fit at both low and high temperatures. The largest deficiencies are at temperatures around 160 K. We cannot be sure if this deficiency is caused by the simplicity of our model, deficiencies in the calorimetry data, plastic relaxations in the sample, or some combination of these reasons.

7.5.3 Anharmonicity and Microstructure — Plastic Deformation

The ordered Ni_3V does not have ideally elastic behavior, as shown by the mechanical hysteresis of Figure 7.6. We are still investigating this mechanical behavior, but some results are clear. The area of the loop is largest for the first few cycles, but the loop remains relatively constant after the fifth cycle shown in Figure 7.6. The area of the loop increases strongly with the maximum strain. We are confident that the data of Figure 7.6 show the hysteretic loss of mechanical energy in the ordered alloy is greater than that in the partially-disordered alloy (for which the maximum strain was larger, but the area of the loop is smaller). In a cyclic process the mechanical deformation of the ordered alloy should be more strongly converted into heat. The area of the particular hysteresis loop shown for the ordered alloy in Figure 7.6 corresponds to 0.6 J/mole, which seems too small to account for the large anharmonic effects in Figure 7.5. However, there are complex microstructural considerations that prevent direct application of the hysteresis loop in a compression test to the calculation of the mechanical hysteresis during the thermal expansion of the alloy.

We are still investigating the origin of the large mechanical hysteresis in the ordered Ni_3V. The hysteretic behavior of the ordered alloy could be promoted by the internal stresses from thermal contraction, which may be nearly large enough to drive plastic deformation at some locations in the microstructure. It is also possible that the axes of tetragonality of the $D0_{22}$ structure may change to accommodate the applied stress. Such a process could be hysteretic if the elastic energy of one ordered region were not transferred efficiently to another region during transformations between variants of the $D0_{22}$ structure. We have performed preliminary measurements of x-ray diffraction patterns when the sample was under a compressive strain of about 0.2%. We found no evidence of transformations between variants of the $D0_{22}$ structure at this strain, however.

7.5.4 Entropy

Using the curve labeled "DOS Anh" in Figure 7.5 or 7.9, we calculated the difference in vibrational entropy of the partially-disordered and ordered

Ni_3V to be 0.025 k_B/atom at 300 K, with the partially-disordered material having the higher entropy. It is risky to extrapolate this heat capacity curve to higher temperatures, but the high temperature limit seems to be about 0.03 k_B/atom. Better agreement with the heat capacities measured by calorimetry requires an upwards scaling of this curve calculated from the phonon DOS. If we ignore the microstructural contribution to the heat capacity, our estimate of the high temperature limit of the vibrational entropy is 0.044 k_B/atom.

We believe, however, that a more accurate estimate of the difference in entropy of the partially-disordered and ordered Ni_3V should consider the microstructural contribution to the heat capacity. If the elastic energy stored in the microstructure is converted into heat as shown by the heat capacity curve labeled "Microstructure" in Figure 7.9, we can use Equation 3.1 to obtain an equivalent entropy difference of 0.025 k_B/atom at 1123 K, again with the partially-disordered material having the higher entropy. Accounting for the microstructural contribution to the heat capacity, our best estimate of the difference in vibrational entropy is (0.037±0.015) k_B/atom. This difference in vibrational entropy between the partially-disordered and ordered states of Ni_3V is smaller than results we have reported for other alloys in this thesis. We expect the reason is that our partially-disordered Ni_3V had nearly the same chemical long-range order as did our ordered Ni_3V.

7.6 Conclusions

We performed a comparative study of two states of Ni_3V, a state of partial disorder obtained by rapid quenching, and the state of equilibrium $D0_{22}$ order obtained by annealing. The heat capacity of the partially-disordered alloy was consistently larger than that of the ordered alloy in the temperature range of our calorimetry measurements, 60 - 325 K. Inelastic neutron scattering was used to obtain approximate phonon density of states curves for the two alloys at 11 K and 300 K. The phonon energies were larger for the ordered alloy than the disordered alloy, as expected from their difference in heat capacities. The $C_V(T)$ calculated from the phonon DOS curves measured at 11 K could account for most of the difference in heat capacities of the two materials at temperatures below 160 K.

The phonon DOS curves showed thermal softening between 11 K and 300 K. Although the phonon DOS of the partially-disordered alloy showed more thermal softening than the ordered alloy, this difference was an order of magnitude too small to account for the large difference in anharmonic heat capacities of the two states of Ni_3V at temperatures greater than 160 K. We propose a novel microstructural contribution to the anharmonic heat capacity. When the alloy is cooled from the high temperature where the ordered domains are formed, anisotropic thermal contractions cause the buildup of elastic energy in the ordered alloy. With increasing temperature, this elastic energy is relieved and converted into heat, suppressing the heat capacity of the ordered alloy. We estimated the differential anharmonic heat capacity by making additional measurements of the linear coefficients of thermal expansion and the Young's moduli of the two alloys. There is sufficient storage of elastic energy in the microstructure to account for the anharmonic behavior measured in the heat capacity, and the predicted temperature dependence is qualitatively correct. There may be another microstructural contribution to the anharmonic heat capacity originating with the hysteretic mechanical behavior of ordered Ni_3V, but this hysteresis seems small.

We calculated the vibrational heat capacity by use of the phonon DOS curves. We modeled the temperature dependence of the microstructural heat capacity, and used it to account for the high temperature part of the experimental $\Delta C_p(T)$. For the partially-disordered and ordered materials at 1123 K, we estimate the difference in vibrational entropy to be $S^{pdis} - S^{ord} = (+0.037 \pm 0.015)\ k_B$/atom. The elastic energy in the microstructure is about 60 J/mole at low temperatures, and makes a contribution to the heat capacity that is equivalent to a difference in entropy of 0.025 k_B/atom.

7.7 Acknowledgments

We thank M. Walter and G. Ravichandran for providing the ultrasonic facilities for the attempted sound velocity measurements, and R. D. Conner for help with the mechanical testing. L. Preister and I. Wong performed much of the sample preparation. We thank L. Anthony for valuable discussions. The Oak Ridge National Laboratory is managed for the Department of Energy by Lockheed Martin Energy Research, Oak Ridge, TN, under contract DE-AC05-96OR22464. This work was supported by the U. S. Department of Energy under contract DE–FG03–86ER45270.

References

[1] L. E. Tanner, Phys. Stat. Solidi **30**, 685 (1968).

[2] A. François, G. Hug, and P. Veyssière, Philos. Mag. A **66**, 269 (1992).

[3] L. J. Nagel, L. Anthony, and B. Fultz, Philos. Mag. Lett. **72**, 421 (1995).

[4] P. A. Flinn, G. M. McManus, and J. A. Rayne, J. Phys. Chem. Solids. **15**, 189 (1960).

[5] F. J. Rotella,"*User Manual for Rietveld Analysis of Time-of-Flight Neutron Powder Diffraction Data at IPNS*," 1983. R. B. Von Dreele, J. D. Jorgensen, and C. G. Windsor, J. Appl. Crystallogr. **15**, 581 (1982).

[6] H. A. Moreen, R. Taggart, and D. H. Polonis, Metall. Trans. A **5**, 79 (1974).

[7] M. J. Pfeifer, P. W. Voorhees, and F. S. Biancaniello, Scripta Metall. Mater. **30**, 743 (1994).

[8] B. Fultz, L. Anthony, L. J. Nagel, R. M. Nicklow, and S. Spooner, Phys. Rev. B **52**, 3315 (1995).

[9] J. Chevrier, J. B. Suck, M. Perroux, and J. J. Caponi, Phys. Rev. Lett. **61**, 554 (1988).

[10] C.-K. Loong, P. Vashishta, R. K. Kalia, W. Jin, M. H. Degani, D. G. Hinks, D. L. Price, J. D. Jorgensen, B. Dabrowski, A. W. Mitchell, D. R. Richards, and Y. Zheng, Phys. Rev. B **45**, 8052 (1992).

[11] J. Chevrier, J. B. Suck, J. C. Lasjanunias, M. Perroux, and J. J. Caponi, Phys. Rev. B **49**, 961 (1994).

[12] V. F. Sears, Phys. Rev. A **7**, 340 (1973).

[13] J.-B. Suck and H. Rudin in Glassy Metals II, H. Beck and H.-J. Güntherodt (Springer-Verlag: Berlin 1983), Chapter 7.

[14] D. D. Klug, E. Whalley, E. C. Svensson, J. H. Root, and V. F. Sears, Phys. Rev. B **44**, 841 (1991).

[15] K.-H. Hellwege (editor in chief), Landolt-Börnstein: Numerical Data and Functional Relationships in Science and Technology, (Springer-Verlag: Berlin, 1981), Volume III/13a.

[16] G. A. de Wit and B. N. Brockhouse, J. Appl. Phys. **39**, 451 (1968).

[17] F. W. de Wette and A. Rahman, Phys. Rev. 176, 784 (1968).

Chapter Eight Co_3V

8.1 Introduction

The final system I have studied is Co_3V, which has an ordered hexagonal structure (shown in Figure 8.2) at temperatures below 1025 °C. According to the Co-V phase diagram in Figure 8.1, there is an $L1_2$ ordered phase from 1025 °C to 1070 °C and a disordered fcc solid solution above 1070 °C. We used differential scanning calorimetry to measure the difference in heat capacity between the fcc disordered and hexagonal ordered phases of Co_3V. We collected neutron diffraction patterns over a wide range of elevated temperatures to determine what phases were present in the material. Although these diffraction measurements were a precursor to our inelastic neutron scattering measurements, they proved interesting in their own right. The inelastic neutron scattering data will not be discussed here but will be published in the near future.

8.2 Experiment

8.2.1 Low-temperature Calorimetry

Ingots of Co_3V were prepared by arc melting pieces of elemental Co and V in an argon atmosphere. The ingots were then cut into 1 mm slices, from which two 6 mm diameter disks were formed by grinding away the excess material. The disks were then sealed in an evacuated quartz ampoule and quenched from 1150 °C into iced brine. This heat treatment froze in the fcc disordered phase. One of the disks was then quenched from 1050 °C to form the equilibrium hexagonal structure. Chemical compositions and chemical homogeneities were measured with a JEOL Superprobe 733 electron

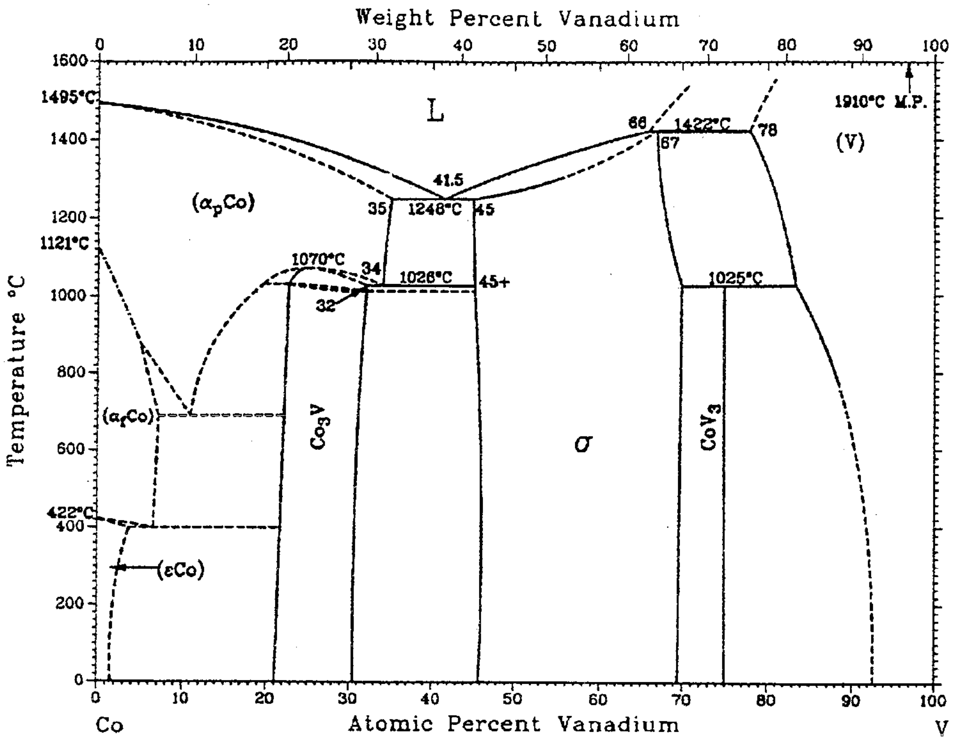

Figure 8.1 Phase diagram for the Co-V alloy system. From T. B. Massalski, editor-in-chief, Binary Alloy Phase Diagrams, 2nd ed. (Materials Park, OH: ASM International, 1990).

microprobe. Averages of the composition measurements gave 24.56 at.% V for the fcc disordered alloy, and 24.29 at.% V for the hexagonal alloy. Composition variations within each sample were no more than about 0.1 at.%. X-ray diffractometry (patterns shown in Figure 8.3) was performed with an Inel CPS–120 diffractometer using Co Kα radiation. An Al filter was used in front of the large-angle position-sensitive detector to suppress V Kα fluorescence.

Low-temperature heat capacity measurements employed a Perkin-Elmer DSC-4 differential scanning calorimeter that had been modified by installing its sample head in a liquid helium dewar. Masses (about 300 mg) of the disordered and ordered alloys were matched to 0.1 mg accuracy and placed in the two sample pans of the DSC. Heat capacity measurements comprised pairs of runs, with the two samples interchanged in their sample pans between runs. The difference in heat capacities of the two samples was

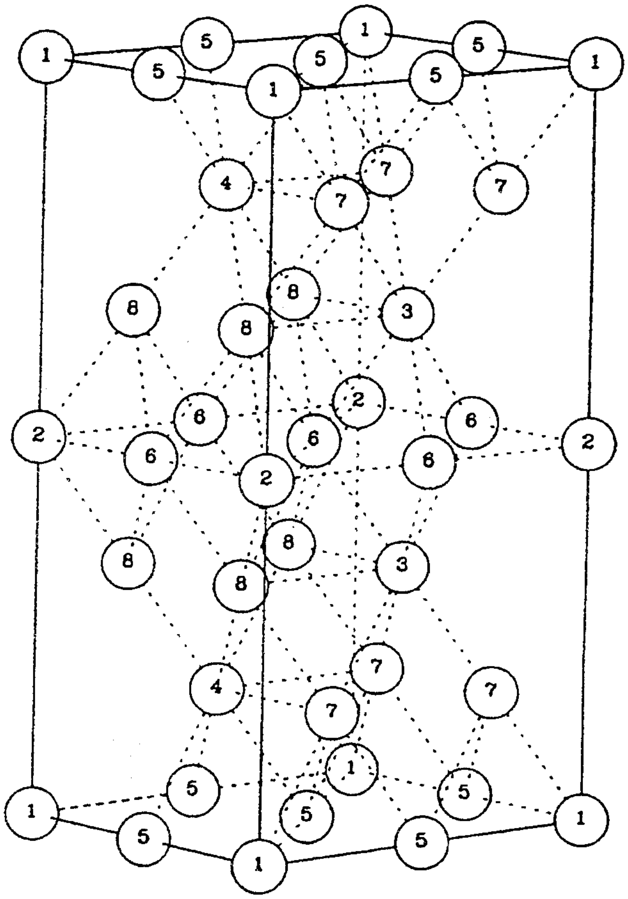

Figure 8.2 The ordered hexagonal structure of Co_3V. The atoms labeled 1-4 are V, while the atoms labeled 5-8 are Co. From J. L. C. Daams et al., Atlas of Crystal Structure Types for Intermetallic Phases, (Materials Park, OH: ASM International, 1991) Volume 3, p. 5286.

obtained from the difference of these two sets of runs. To test reproducibility, we obtained eight matched pairs of runs with liquid nitrogen, and two matched pairs with liquid helium as the cryogen. To counteract instrumental drift, runs comprised two pairs of scans over temperature intervals of 30 K, which typically overlapped by 10 K. Scans were performed at a heating rate of 20 K min^{-1}.

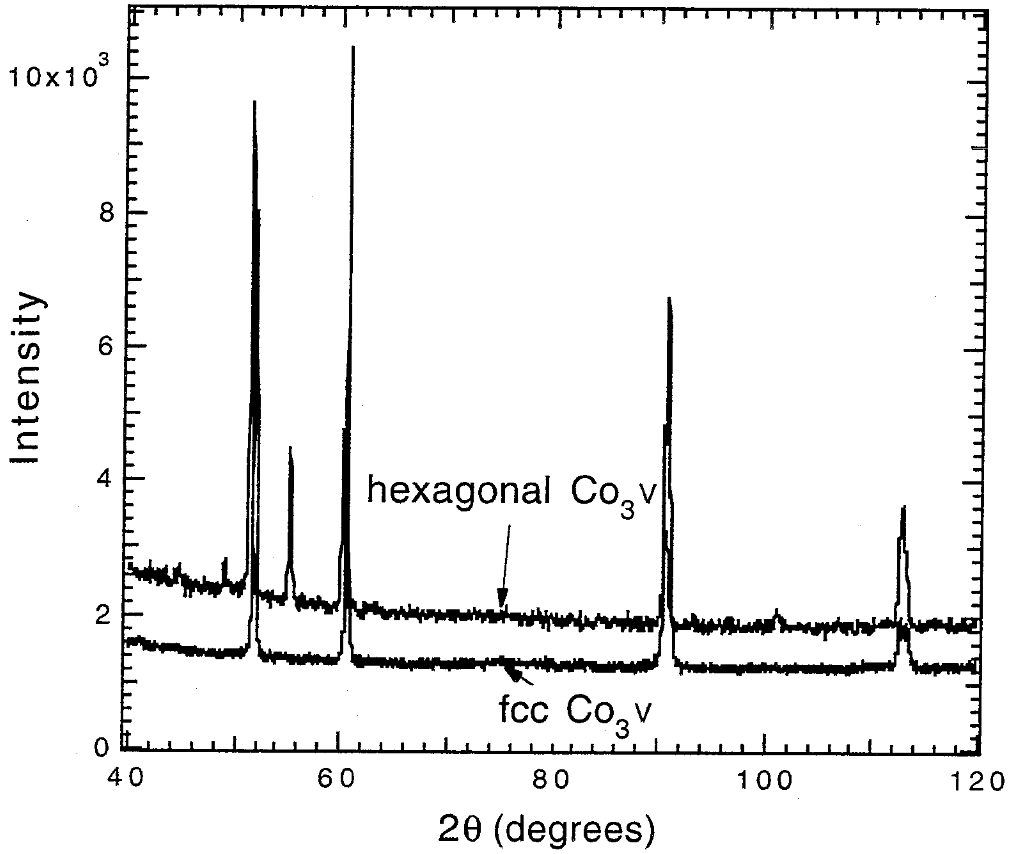

Figure 8.3 X-ray diffraction patterns for Co3V.

8.2.2 Neutron Diffraction

The Co3V samples used in our neutron work were prepared by the Ames Laboratory. Approximately 550 grams of Co3V were melted in a magnesia-stabilized zirconia melting system, heated to 1600 °C, and atomized on a yttria-stabilized zirconia atomization disk spinning at 11,950 rpm. The material was quenched in Dow 200 polydimethyl siloxane fluid which was removed with heptane and ethyl alcohol; then the material was dried under vacuum. The particles produced by this method ranged from a few tenths of a millimeter in size to a few millimeters in size.

Chemical compositions and chemical homogeneities were measured with a JEOL Superprobe 733 electron microprobe. These analyses showed the Co_3V granules to be of stoichiometric composition and homogeneous within the accuracy of the equipment. The external 10 μm of the granules showed evidence of Si from the quenching liquid, but not enough to cause any concern. A Hewlett-Packard 5890 gas chromatograph equipped with a thermal conductivity detector was utilized in order to detect and quantify evolved hydrogen gas, which could affect the neutron scattering results. No hydrogen was detected by this system; detectability limits were 0.0032 wt.% for hydrogen.

Neutron-diffraction data were collected using the HB4 high-resolution powder diffractometer at the High-Flux Isotope Reactor at ORNL. This instrument has a Ge (115) monochromator which, when 2-theta = 87°, selects an incident neutron wavelength of 1.5 Å. Soller slit collimators of 12' and 20' are positioned before and after the monochromator crystal, respectively. An array of 32 equally spaced (2.7°) ^{3}He detectors, each with a 6' mylar foil collimator, can be step-scanned over a range of up to 40° for scattering angles between 11° and 135°.

The samples were placed in vanadium cans (9 mm inner diameter by 6 cm in length) for data collection at temperatures from 295 K to 1358 K (22°C to 1085°C) over the 2-theta range of 11° to 135° in steps of 0.05°. Thin Gd spacer disks were placed in the can in an effort to suppress multiple scattering. The sample cans were then placed in a high-temperature furnace which was kept under high vacuum throughout the experiment. Our chosen temperature range allowed us to examine several phases of the material, as is evident from the phase diagram in Figure 8.1. For these data collections, the detector array was scanned in two segments to overlap up to eight detectors in the middle of the pattern. Overlapping detectors for a given step serves to average the counting efficiency and the 2-theta zero-point shift for each detector.

8.3 Results

8.3.1 Low-temperature Calorimetry

Averaged results from the differential calorimetry measurements are presented in Figure 8.4. The sign of the data is positive, showing that Co_3V has a larger heat capacity in the disordered state than in the ordered state. The data of Figure 8.4 could be best fit with a difference of two Debye heat capacities with Debye temperatures of 320 K for the disordered state and 332 K for the ordered phase. Using Equation 7.1, the difference in vibrational entropy between the two states of the material is 0.11 ± 0.02 k_B/atom.

8.3.2 Neutron diffraction

The neutron diffraction patterns are presented in Figure 8.5. The program Lazy Pulverix (see Appendix C) was used to index these patterns. The first data set was collected at room temperature and was indexed as $L1_2$. It seems quite reasonable that the process used to produce these samples might have quenched in $L1_2$ order from the small region on the phase diagram in Figure 8.1. As we increased the temperature, several diffraction patterns were collected over the range 200-660 °C; these data were added together and also

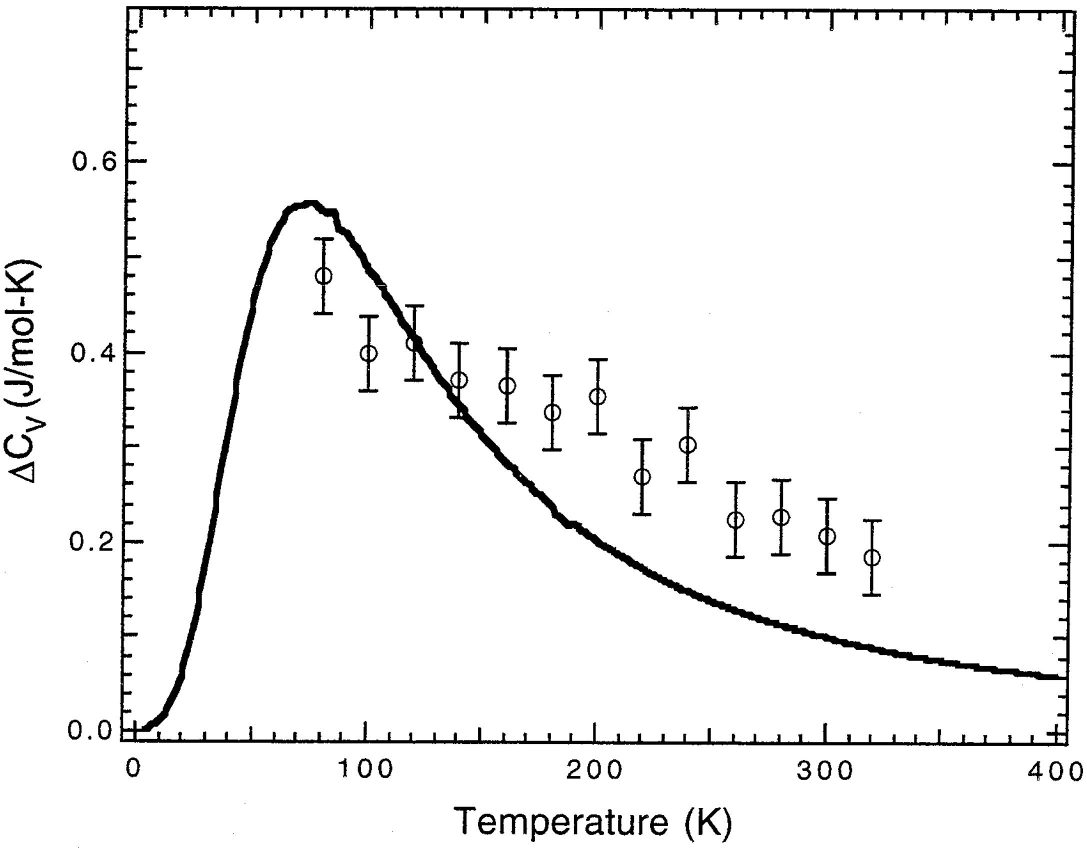

Figure 8.4 Differential heat capacities. Points: averages of scans with differential calorimetry of the difference in heat capacity of fcc and hexagonal Co_3V materials (sign is fcc minus hcp). Error bars indicate variations between different runs. The solid line represents the difference of two Debye heat capacities for Debye temperatures of 320 K and 332 K.

indexed as $L1_2$. However, by 950 °C, the equilibrium ordered hexagonal phase (shown in Figure 8.2) has emerged. As we heat the material past 1025 °C, we expect to find a region of $L1_2$ order; however, that is not the case. We find the fcc disordered spectra beginning to form by 1038 °C as the intensity of the ordered hexagonal peaks begins to decrease. By 1085 °C the hexagonal phase is

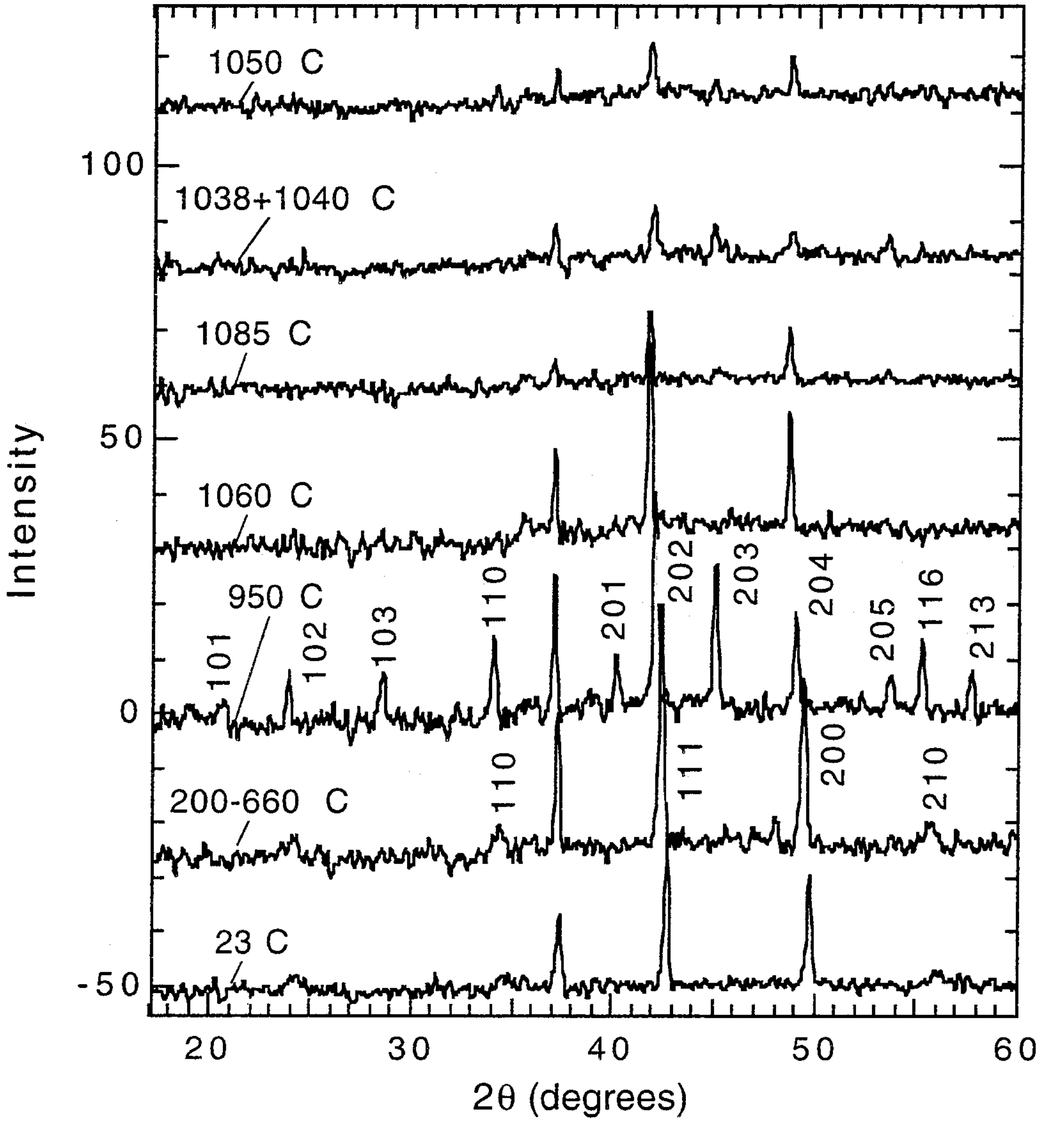

Figure 8.5 Neutron diffraction patterns for Co_3V. The data have been vertically offset for clarity. The unlabeled peak at 37° is from the Nb window in the furnace.

completely gone. Note that the overall intensity of the peaks has been decreased. We later attributed this loss of intensity to an unfortunate diffusion of Gd from the spacer disks in the sample cans.

The existence of the high temperature $L1_2$ phase had been documented by several others [1-6], but all their measurements were performed on quenched samples. The fact that our in-situ neutron diffraction experiments did not reveal this phase suggests that $L1_2$ order is a nonequilibrium phase. We suspect it forms at low temperatures when the quenched material has an fcc rather than hexagonal lattice. In this case it may be energetically favorable for the alloy to develop some $L1_2$ chemical order, even though a transformation to a hexagonal lattice is suppressed kinetically. We note that the ordered hexagonal phase is closely related to a faulted form of the $L1_2$ structure.

8.4 Conclusions

We have performed low-temperature calorimetry on two phases of Co_3V, an fcc disordered phase and a hexagonal phase. The disordered phase has the larger heat capacity, and the difference in vibrational entropy between the two phases is 0.11 ± 0.03 k_B/atom. We also performed in-situ neutron diffraction experiments over a wide range of temperatures. These experiments showed that the $L1_2$ region of the phase diagram does not exist. We believe the observed $L1_2$ phase is a state that can be obtained in quenched alloys.

References

[1] W. Koster and H. Schmid, Z. Metallkd. **46**, 195 (1955).

[2] E. T. Peters and L. E. Tanner, Trans. Metall. Soc. of AIME **233**, 2126 (1965).

[3] G. Inden, Scripta Metall. **15**, 669 (1981).

[4] Y. Aoki, Y. Obi, and H. Komatsu, Z. Metallkd. **70**, 436 (1976).

[5] S. Saito, Acta Cryst. **12**, 500 (1959).

[6] Y. Aoki, K. Asami, and M. Yamamoto, Phys. Stat. Sol. A **23**, K167 (1974).

Chapter Nine Nanophase Fe

9.1 Introduction

There has been strong recent interest in nanocrystalline materials, generally defined as materials with microstructural features of 100 nm or less. The interesting microstructure-properties relationships of nanostructured materials are often classified as "confinement effects" and "interface effects." An example of a "confinement effect" is the shift in frequency of optical absorption that occurs in semiconductors when the crystallite size is comparable to the size of the electron-hole exciton [1]. An example of an "interface effect" is the surprisingly high ductility of nanocrystalline ceramic TiO_2, which has been attributed to atom movements within its copious grain boundaries [2]. A high density of grain boundaries is certainly a distinguishing feature of nanocrystalline materials, but there were also reports that nanocrystalline grain boundary structures are more disordered than grain boundaries in large-grained materials [3]. Although some of these early claims have been shown to be overstated [4,5], in the present work we show evidence of nanocrystalline vibrations that involve the motion of stiff crystallites separated by weak inter-crystallite forces.

There were early reports that the heat capacity of nanocrystalline materials is significantly larger than that of large-grained materials [6]. Unfortunately, contamination by interstitial helium may have vitiated these early observations [7]. Some measurements of Debye-Waller factors have indicated that atoms in nanocrystals have larger thermal mean-square displacements than in large-grained materials [8-11]. More recently, Suzuki and Sumiyama measured neutron inelastic scattering spectra on nanocrystalline Ta prepared by mechanical attrition [12]. These authors reported a smoothing of features in the phonon density of states (DOS) of the nanocrystalline Ta (10 nm crystallite size), but no general softening of the vibrational spectrum. On the other hand, in a recent inelastic neutron scattering study on nanocrystalline Ni3Al with a 7 nm crystallite size [13], a large enhancement of the phonon DOS at low energies was reported, although it was suggested that this could have been caused by quasielastic scattering by hydrogen in the material. The present work was undertaken to measure the phonon DOS in nanocrystalline Fe, which is not expected to absorb a significant amount of hydrogen. For nanocrystalline Fe we report some enhancement of the phonon DOS at low energies, together with a smoothing of the longitudinal peak.

9.2 Experiment

Iron powders were made by mechanical attrition of pieces of Fe of 99.995% purity. The material was milled for 12 hours in a Spex 8000 mixer/mill with hardened steel vials and balls and a ball-to-powder weight ratio of 5:1. For comparison, a second sample was prepared from some of this same powder by annealing at 500 °C in an evacuated quartz ampoule for 0.5 hours, and then followed by cooling at the rate of 50 °C/h. X-ray diffractometry was performed with an Inel CPS–120 diffractometer using Co Ka radiation. A few grams of the powders were heated to 400 °C and analyzed for evolved hydrogen, oxygen, and nitrogen by a Hewlett-Packard 5890 gas chromatograph equipped with a thermal conductivity detector.

Samples of the as-milled and the annealed powders, each about 50 grams, were placed in thin-walled aluminum cans and mounted at room temperature on the goniometer of the HB2 triple axis spectrometer at the High Flux Isotope Reactor at the Oak Ridge National Laboratory. The spectrometer was operated in constant-Q mode with the fixed final energy, E_f, of 14.8 meV. The energy loss spectra were made by scanning the incident energy from 14.8 meV to 74.8 meV. The neutron flux from the monochromator was monitored with a fission detector, which was used to control the counting time for each data point. The incident beam on the pyrolytic graphite monochromator crystal had a collimation of 110′, and 40′ Soller slits were used between the monochromator and the sample. Pyrolytic graphite filters placed after the sample were used to attenuate the 1/2 and 1/3 contamination. The filtered beam passed through 40′ slits before the pyrolytic graphite analyzer crystal. Following the analyzer, 70′ Soller slits were used before the ^{3}He detector. With this arrangement, the energy resolution varied between 0.9 and 2 meV, depending on the energy transfer and the slope of the phonon dispersion surface. Spectra from each specimen were obtained at two values of Q , 3.98 and 4.60 $Å^{-1}$.

9.3 Results

Figure 9.1 presents x-ray diffraction patterns from the as-milled powder and from the same powder after annealing. Grain sizes and distributions of internal strains were obtained by the method of Williamson and Hall [14], after correcting the peak shapes for the characteristic broadening of the x-ray diffractometer. In this method the widths of the diffraction peaks in k-space were plotted against the k-vectors of the diffraction peaks. The slopes of these

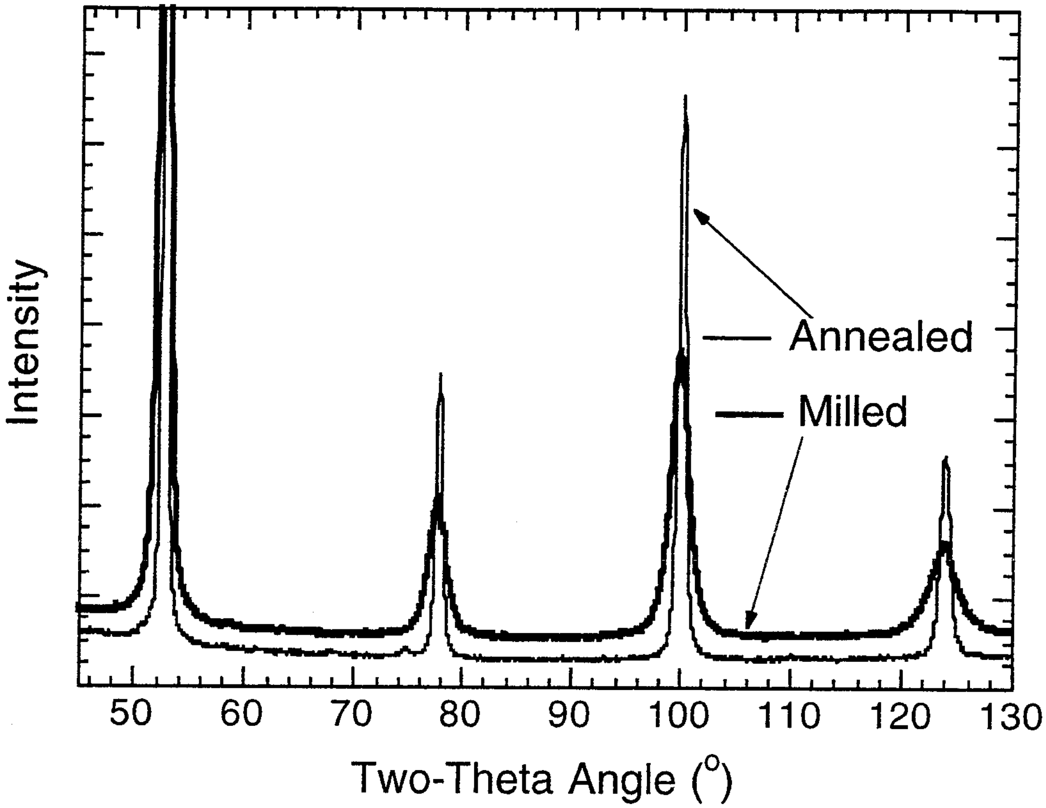

Figure 9.1 X-ray powder diffraction patterns of the as-milled (nanocrystalline) and annealed (larger-grained) Fe powders. The as-milled data are offset vertically for clarity.

plots then provide the mean-squared strain, and the y-intercepts provide the characteristic crystallite size. We also used the Scherrer method to determine a crystallite size [14]. Mean crystallite sizes were 12 nm for the as-milled Fe powder and 28 nm for the annealed powder. The mean squared strains were 0.4 % in the as-milled, and 0.1 % in the annealed powders. Gas chromatography showed that the as-milled and annealed samples of Fe powder had, respectively, hydrogen contents of <0.004 and 0.006 wt.%, oxygen contents of 0.236 and 0.262 wt.%, and nitrogen contents of 0.748 and 0.849 wt.%. Some of these gases, especially oxygen and nitrogen, may have been adsorbed on the surfaces of the powders and not absorbed interstitially. The as-milled and annealed samples of Ni_3Al had, respectively, hydrogen contents of 0.0083 and 0.0128 wt.%, oxygen contents of 0.0695 and 0.0502 wt.%, and nitrogen contents of 0.232 and 0.188 wt.%. We do not expect any significant quasielastic neutron scattering from these trace amounts of hydrogen.

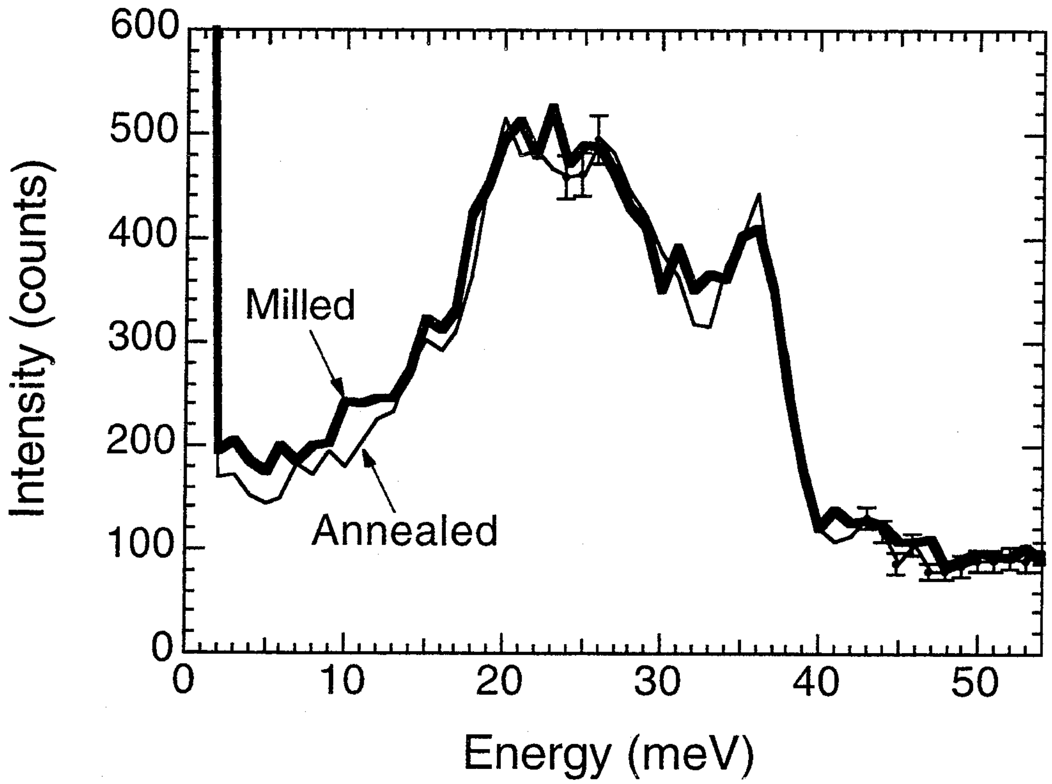

Figure 9.2 Sum of neutron energy loss spectra at Q = 3.98 and 4.60 Å^{-1} for the nanocrystalline and larger-grained powders.

The individual energy loss spectra from the Fe powders show a modest dependence on the momentum transfer, Q, as is generally expected for coherent inelastic scattering from polycrystalline alloys [15]. Figure 9.2 presents the sum of the spectra for both values of Q, 3.98 and 4.60 Å^{-1}. In these summed data, as in the individual pairs of spectra, two differences are seen. First, in the low energy regions below 15 meV, there is stronger scattering from the as-milled Fe than the annealed Fe. The second difference is that the spectra from the annealed powder have sharper longitudinal peaks (near 36 meV) than do the spectra from the as-milled powder. This is seen most prominently for the peak of the longitudinal branch at an energy of about 36 meV.

9.4 Analysis of Phonon DOS

The analysis of the scattering data was helped considerably by the availability of interatomic force constants obtained from previous work with single crystals of bcc Fe. Using the force constants of bulk Fe from Reference [16], the dynamical matrix of the Born – von Kármán model, $\mathbf{D}(\mathbf{q})$ [17], was diagonalized for approximately 10^5 values of $\mathbf{k}$ distributed uniformly over the first Brillouin zone. Histogram binning of the resulting eigenfrequencies provided the calculated phonon DOS. For comparison with our experimental data, this calculated phonon DOS was convoluted with a gaussian function of full-width-at-half-maximum of 3.9 meV.

The experimental energy loss spectra include coherent and incoherent scattering. The incoherent scattering has the shape of the phonon DOS weighted by a thermal factor, but the coherent scattering contribution has a shape that is sensitive to the momentum transfer Q. In particular, the coherent inelastic scattering at low energies is expected to be relatively weak for our choices of Q. This is because the sum over $\mathbf{q}$ for the dynamical structure factor includes a factor of $\delta(\mathbf{Q}-\mathbf{q}-\tau)$, where τ is a reciprocal lattice vector, **q** is the phonon wavevector, and **Q** is the momentum transfer. To obtain the strongest coherent inelastic scattering from phonons with small q, the value of Q should be nearly a reciprocal lattice vector. This is not the case for our choices of 3.98 and 4.60 $Å^{-1}$. We devised a correction procedure, described below, to convert the neutron energy loss spectrum of the nanocrystalline powder to a phonon DOS, using the calculated and experimental results from the larger-grained Fe as a reference.

The features of the inelastic scattering described in the previous section led us to the following procedure for obtaining an approximate phonon DOS from the experimental data. Our data analysis procedure has some similarities to methods used previously [13, 18-22]. The individual spectra for both Q = 3.98 and 4.60 $Å^{-1}$ were first summed (see Figure 9.2). The same constant background was then subtracted from the summed spectra — a constant background is a good approximation for data from the HB2 spectrometer. To understand the thermal factor, the incoherent inelastic scattering was calculated for bcc Fe using the conventional multiphonon expansion [18, 20, 23]. We found that at the relatively low values of Q and temperature of the present experiments, multiphonon corrections would have made little difference to the resultant phonon DOS. We therefore divided each background-corrected spectrum by the one-phonon correction factor, $(n(\nu) - 1)/\nu$ [24]:

$$\frac{n(\nu) - 1}{\nu} = \frac{1}{\nu\,[1 - \exp(-h\nu/kT)]} \quad . \qquad 9.1$$

To accommodate the Q-dependence of the coherent inelastic scattering, we compared these intermediate results to the calculated phonon DOS of Fe. We obtained a correction function by dividing this calculated DOS by the intermediate result from the annealed Fe powder. When the intermediate result for the annealed bcc Fe was multiplied by this correction function, the calculated curve was of course recovered, and this curve is shown at the bottom of Figure 9.3. On the other hand, when the intermediate result from

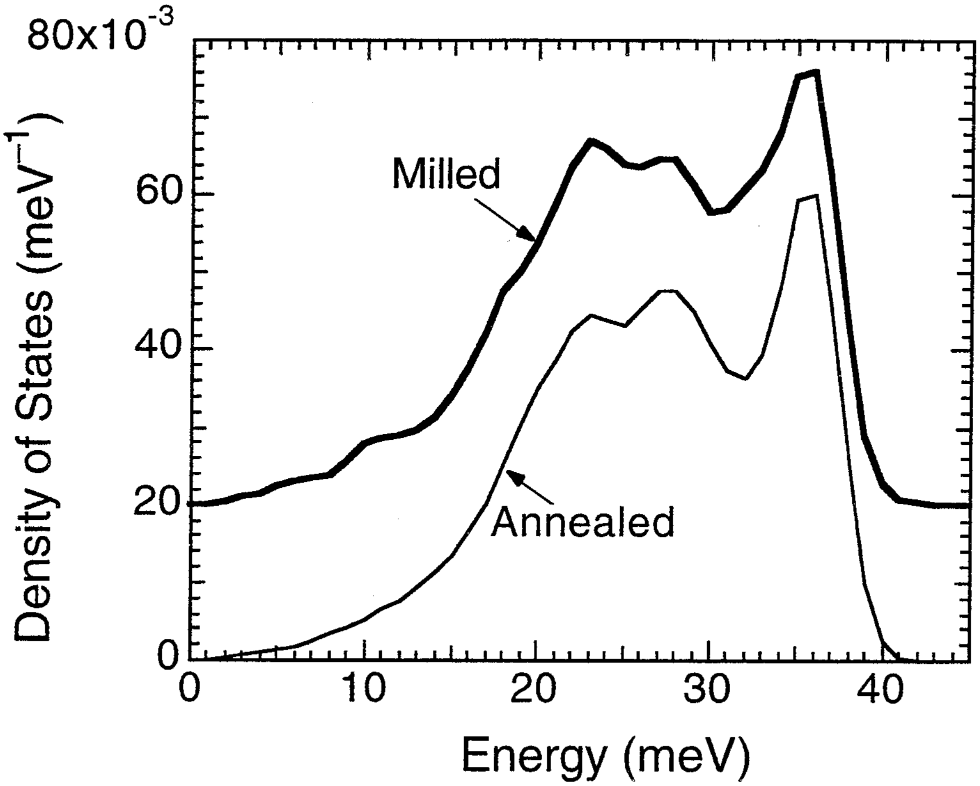

Figure 9.3 Phonon DOS curves obtained from the experimental data of Figure 9.2, using the calculated phonon DOS to generate a correction factor for converting the annealed Fe spectrum into the Fe phonon DOS. The "instrumentally-broadened" phonon DOS from Fe, equal to the corrected phonon DOS of the annealed specimen, is shown as "Annealed." The data from the as-milled sample are offset vertically by 0.02.

the nanocrystalline, as-milled Fe was multiplied by this correction function, we obtained the phonon DOS for the nanocrystalline Fe at the top of Figure 9.3. Finally, we normalized the areas of the phonon DOS curves. (The normalization correction was small, about 3%, and likely caused by differences in the powder packing in the two sample cans.)

9.5 Discussion

9.5.1 High Energy Regime

Figure 9.3 shows that the "longitudinal peak" at 36 meV is broadened in the as-milled material in comparison to the peak in the annealed material. Much of the broadening may have been caused by short phonon lifetimes in nanophase material — a "confinement effect." A phonon wavepacket is expected to travel a distance, $l \sim 12$ nm, characteristic of the crystallite size, before scattering. The characteristic number of cycles for the phonon lifetime, y, is:

$$y = \frac{\nu\, l}{v} \qquad 9.2$$

where v is the sound velocity and ν is the phonon frequency. For the longitudinal peaks in Fe, Equation 9.2 gives $y \sim 20$, suggesting a lifetime broadening of 5 to 10% in energy. This is a significant effect that can account for the observed broadening. The lifetime broadening should be approximately symmetrical about the mean energy, however, and the longitudinal peak in the experimental spectra is broadened more asymmetrically than expected for a damped harmonic oscillator. There is a distinct shift of some longitudinal frequencies towards lower energies in the nanophase Fe. A lower effective stiffness, presumably caused by crystalline defects, could be responsible for this shift.

9.5.2 Low Energy Regime

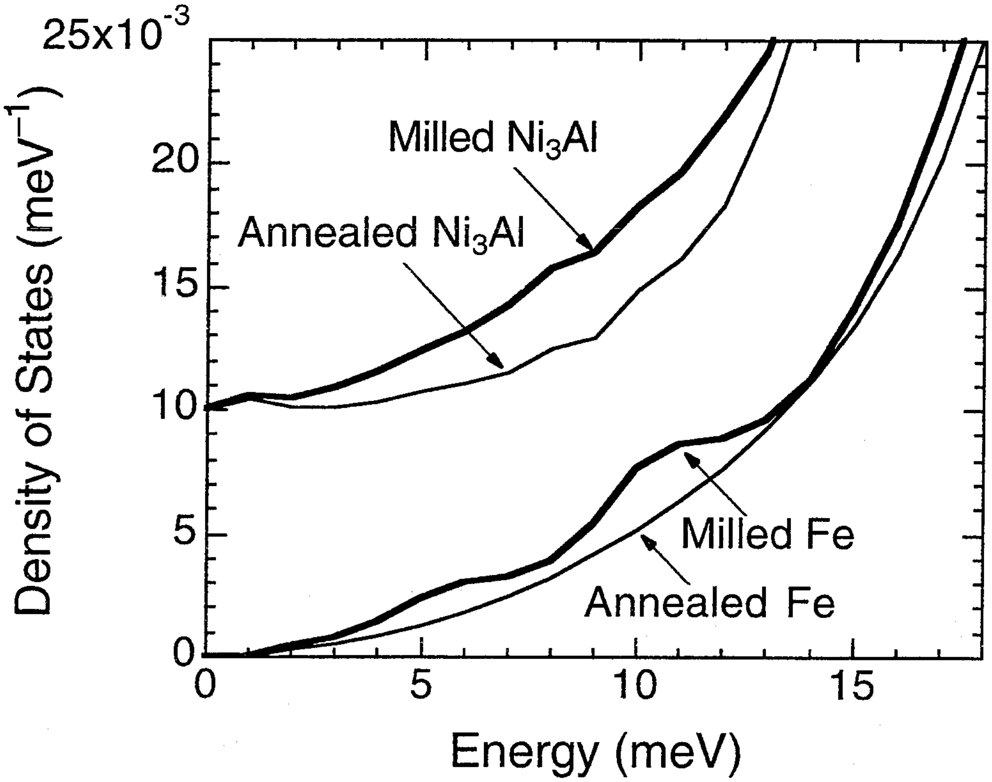

Figure 9.4 Enlargement of the data of Figure 9.3, together with an enlargement of the phonon DOS for Ni3Al (see Chapter Five).

The second feature of the phonon DOS of the nanophase material that differs observably from that of the annealed Fe is an enhancement of vibrational modes at low energies. The phonon DOS at low energies is presented in Figure 9.4, together with an enlargement of the results from as-milled and annealed powders of Ni3Al (see Chapter Five). The effects are qualitatively similar, but larger for Ni3Al than for Fe. Although we suggested previously that this enhancement of the Ni3Al phonon DOS in the low energy regime could have been caused by quasielastic scattering from hydrogen [13], the present measurements of hydrogen in the Ni3Al powders showed that the as-milled powder actually has less hydrogen than the annealed powder. Recent measurements of the phonon DOS of nanophase and large-grained Ni by Trampenau, et al., [25] gave results similar those in Figure 9.4 for Ni3Al.

Fecht [26] and Wagner [27] proposed a two-phase model for atomic vibrations in nanocrystalline materials, in which the "grain boundary phase" has vibrations of lower frequency than the "crystalline phase." Perhaps some of the softening of the high frequency modes described in Section 9.1.5.1 can be understood as atom vibrations within the grain boundary region. It is harder to understand our observed enhancements in the low energy regime with a two-phase model, however. It is unlikely that long wavelength phonons can exist within a grain boundary. It is also unlikely that the short wavelength phonons within a grain boundary can be suppressed in energy from 30 meV to around 3 meV, since this implies a softening of the effective interatomic force constants by a factor of 100.

We suggest that some enhancement of the phonon DOS at low energies could originate from inter-crystallite vibrations of the nanocrystalline microstructure. It is important to ask what condition is required for the low energy DOS of a nanocrystalline microstructure to be comparable or larger than the phonon DOS of a crystal of individual atoms.

In the Debye model, or for phonons at low q characterized by a constant velocity of sound, we have a density of states, g(ν) :

$$g(\nu) = \frac{9\,N}{\nu_D^3}\nu^2 \quad . \qquad 9.3$$

The Debye frequency is:

$$\nu_D \propto \sqrt{\frac{k}{m}} \quad , \qquad 9.4$$

where k is an averaged inter-atomic force constant and m is an atomic mass. In lumping n atomic masses into a nanocrystal, we have a new DOS for the nanocrystalline microstructure, g'(ν) :

$$g'(\nu) = \frac{9\,N}{n\,\nu_D'^3}\nu^2 \quad , \qquad 9.5$$

where the Debye frequency for the nanocrystalline microstructure, ν_D', is:

$$\nu_D' \propto \sqrt{\frac{k'}{n\,m}} \quad , \qquad 9.6$$

and k' is an average inter-crystallite force constant. To obtain a high density of states in the nanocrystalline microstructure, we seek the condition: g'(ν) > g(ν). We formulate this condition with Equations 9.3, 9.4, and 9.5, 9.6:

$$\frac{9\,N}{n}\left(\frac{n\,m}{k'}\right)^{3/2}\nu^2 > 9N\left(\frac{m}{k}\right)^{3/2}\nu^2 \quad , \qquad 9.7$$

$$n^{1/3}\,k > k' \quad . \qquad 9.8$$

For a nanocrystalline microstructure to have an enhancement in its density of states at low energies that is comparable to the density of states itself, Equation 9.8 requires that the intercrystallite force constant must increase more slowly than the linear dimension of the crystallite, l. For a two-dimensional grain boundary between crystallites, whose area scales as l^2, this demands that the average interatomic bond across the grain boundary decreases in strength inversely with l. The stiffness of grain boundaries in nanocrystalline materials is largely unknown, but we do expect that the interatomic force constants across a grain boundary are weaker than in regions of good crystalline material. The inter-crystallite force constants are probably sensitive to the particular material and its processing. It therefore seems plausible that there could be a significant difference in the inter-crystallite force constants of our nanocrystalline Fe and nanocrystalline Ni_3Al. Since the nanocrystalline Ni_3Al had a crystallite size of 7 nm, versus 10 and 12 nm for the nanocrystalline Ta [12] and Fe, it is also possible that the requirement of Equation 9.8 may be better satisfied by nanocrystalline Ni_3Al than nanocrystalline Fe or Ta, giving a larger enhancement of the phonon DOS of Ni_3Al at low energies. In addition to our uncertainty of the inter-crystallite force constants, however, we have important uncertainties about the lattice dynamics of an irregular nanocrystalline microstructure, such as the coupling between inter- and intra-crystallite vibrations.

9.5.3 Vibrational Entropy

We define $\Delta S_{vib} \equiv S^{nan}_{vib} - S^{lg}_{vib}$ as the difference in vibrational entropy of two states of a material, nanocrystalline and larger-grained, at high temperatures. This difference in vibrational entropy depends in a straightforward way on the difference in the phonon DOS of the two phases, $g^{nan}(\nu) - g^{lg}(\nu)$ [13]:

$$\Delta S_{vib} = -3k_B \int_0^\infty \left(g^{nan}(\nu) - g^{lg}(\nu)\right) \ln(\nu)\ d\nu \quad , \qquad 9.9$$

where the difference avoids problems with the dimensions of the argument of the logarithm. Using the phonon DOS shown in Figure 9.3, we find ΔS_{vib} = 0.019 k_B/atom for the difference in vibrational entropy between the as-milled nanophase Fe and the annealed larger-grained Fe. This difference in vibrational entropy contributes only a small amount to the thermodynamic stability of the nanophase microstructure, giving a $-T \cdot \Delta S_{vib}$ term in the free energy of −48 J/mole at 300 K. In comparison, the excess enthalpy of nanophase materials is a few kJ/mole [28]. Although we do not find a large entropy for nanocrystalline Fe as suggested previously [26, 27], it is possible that ΔS_{vib} may be larger for nanocrystalline materials having weaker inter-crystallite force constants and crystallite sizes smaller than 12 nm.

9.6 Conclusions

We performed inelastic neutron scattering experiments on Fe powders in two microstructural states: as nanocrystals prepared by high energy ball milling and as larger crystallites prepared by annealing. For each sample, neutron energy loss spectra were collected at two values of Q. A Born-von Kármán analysis was performed with the force constants of bcc Fe, and the results from this analysis provided a correction factor for converting our experimental results from the larger-grained, annealed material to a phonon DOS of bcc Fe. The spectra from the as-milled nanocrystalline powder were also analyzed with this method, so that differences in the phonon DOS could be identified.

We found two differences in the phonon DOS of the nanocrystalline and larger-grained Fe powders. At high energy we found a broadening of the longitudinal peak in the nanocrystalline powder. This could be caused primarily by lifetime broadening. It also seems that in the nanocrystalline material, the longitudinal modes are shifted downwards in energy. A second difference in the phonon DOS occurred in the low energy regime below about 15 meV, where the phonon DOS of the nanocrystalline material was enhanced over that of the larger-grained material. We attribute this enhancement of the phonon DOS to inter-crystallite vibrational modes of the nanocrystalline microstructure. These measured changes in phonon DOS should have only a small effect on the vibrational entropy of nanocrystalline Fe prepared by high energy ball milling.

References

[1] S. Schuppler, S. L. Friedman, M. A. Marcus, D. L. Adler, Y. H. Yie, F. M. Ross, T. D. Harris, W. L. Brown, Y. J. Chabal, et al., Phys. Rev. Lett. **72**, 2648 (1994).

[2] H. Karch, R. Birringer, and H. Gleiter, Nature **330**, 556 (1987).

[3] X. Zhu, R. Birringer, U. Herr, and H. Gleiter, Phys. Rev. B **35**, 9085 (1987). T. Haubold, R. Birringer, B. Lengeler, and H. Gleiter, Phys. Lett. A **135**, 461 (1989).

[4] M. R. Fitzsimmons, J. A. Eastman, M. Müller-Stach, and G. Wallner, Phys. Rev. B **44**, 2452 (1991).

[5] B. Fultz, H. Kuwano, and H. Ouyang, J. Appl. Phys. **76**, 5961 (1994).

[6] H. Gleiter, Prog. Mater. Sci. **33**, 223 (1989).

[7] A. Tschöpe and R. Birringer, Acta Metall. Mater. **41**, 2791 (1993).

[8] G. Von Eynatten, J. Horst, K. Dransfeld, and H. E. Bömmel, Hyperfine Interact. **29**, 1311 (1986).

[9] J. A. Eastman and M. R. Fitzsimmons, J. Appl. Phys. **77**, 522 (1995).

[10] M. Hayashi, E. Gerkema, A. M. van der Kraan, and I. Tamura, Phys. Rev. B **42**, 9771 (1990).

[11] L. B. Hong, C. C. Ahn, and B. Fultz, J. Mater. Res. **10**, 2408 (1995).

[12] K. Suzuki and K. Sumiyama, Mater. Trans. JIM **36**, 188 (1995).

[13] B. Fultz, L. Anthony, L. J. Nagel, R. M. Nicklow, and S. Spooner, Phys. Rev. B **52**, 3315 (1995).

[14] H. P. Klug and L. E. Alexander, X-Ray Diffraction Procedures (Wiley-Interscience: New York, 1974), p. 656 and 664.

[15] F. W. de Wette and A. Rahman, Phys. Rev. **176**, 784 (1968).

[16] V. J. Minkiewicz, G. Shirane, and R. Nathans, Phys. Rev. **162**, 528 (1967).

[17] G. Venkataraman, L. A. Feldkamp, and V. C. Sahni, Dynamics of Perfect Crystals (MIT Press: Cambridge, 1975), Chapter 2.

[18] J.-B. Suck and H. Rudin in Glassy Metals II, H. Beck and H.-J. Güntherodt (Springer-Verlag: Berlin 1983), Chapter 7.

[19] J. Chevrier, J.-B. Suck, M. Perroux, and J. J. Caponi, Phys. Rev. Lett. **61**, 554 (1988).

[20] D. D. Klug, E. Whalley, E. C. Svensson, J. H. Root, and V. F. Sears, Phys. Rev. B **44**, 841 (1991).

[21] C.-K. Loong, P. Vashishta, R. K. Kalia, W. Jin, M. H. Degani, D. G. Hinks, D. L. Price, J. D. Jorgensen, B. Dabrowski, A. W. Mitchell, D. R. Richards, and Y. Zheng, Phys. Rev. B **45**, 8052 (1992).

[22] J. Chevrier, J.-B. Suck, J. C. Lasjanunias, M. Perroux, and J. J. Caponi, Phys. Rev. B **49**, 961 (1994).

[23] V. F. Sears, Phys. Rev. A **7**, 340 (1973).

[24] G. Kostorz and S. W. Lovesey in Treatise on Materials Science and Technology Vol. 15 Neutron Scattering, G. Kostorz, ed. (Academic Press: New York, 1979), p. 1.

[25] J. Trampenau, K. Bauszuz, W. Petry, and U. Herr, Nanostructured Mater. **6**, 551 (1995).

[26] H. J. Fecht, Phys. Rev. Lett. **65**, 610 (1990).

[27] M. Wagner, Acta Metall. Mater. **40**, 957 (1992).

[28] H. J. Fecht, E. Hellstern, Z. Fu, and W. L. Johnson, Adv. Powder Metallurgy **1-3**, 111 (1989).

Chapter Ten Summary

10.1 Summary of Experimental Results

The results I have measured for the difference in vibrational entropy between two states of a material are presented in Table 10.1.

Table 10.1 Difference in vibrational entropy between two states of a material.

Material	State 1	State 2	ΔS_{vib} (k_B/atom)
Fe_3Al	bcc	$D0_3$	0.1 ± 0.03
Ni_3Al	fcc	$L1_2$	0.2 ± 0.1
Cu_3Au	fcc	$L1_2$	0.14 ± 0.05
Ni_3V	fcc	$D0_{22}$	0.037 ± 0.015
Co_3V	fcc	hexagonal	0.11 ± 0.03
Fe	nanophase	larger grained	0.019

10.2 Conclusions

The magnitude of the difference in vibrational entropy between two states of a material can vary by an order of magnitude for two different materials depending on the structures and the degree of order. However, these results can be measured accurately and give us a great deal of information about the transformation between two states of a material. In most of the cases I have examined, the difference in vibrational entropy has a magnitude comparable to the maximum possible difference in configurational entropy for a 3:1 atomic ratio, 0.56 k_B/atom.

Although to be completely accurate, the difference in vibrational entropy between two states of a material must be measured at the critical point, the results I have measured at low temperatures should still give a reasonably good idea of what is taking place in the transformation. The research community is beginning to recognize the impact that studies incorporating vibrational entropy can have on the field of alloy thermodynamics. The implications for prediction of phase diagrams are great, considering that accounting for vibrational entropy in a model can shift the critical temperature by a factor of two. Recent work on the Fe-Cr system has shown that the composition dependence of the configurational entropy differs from the composition dependence of the vibrational entropy [1]. Also, studies of the phase diagrams for V-H and V-D have shown that different phases exist in the two systems [2]. Since this cannot be a chemical effect, it must result from vibrational entropy differences.

10.3 Directions for Future Work

Although I have examined differences in vibrational entropy in several different alloy systems in my thesis work, there are obviously many systems which have not been studied. Now that it has been proven that vibrational entropy can make a contribution to the thermodynamics of an order–disorder transformation, the next stage of this research should embrace a more systematic approach to discovering trends based on the alloys and crystal structures involved. It would be informative to examine alloy systems which have the $D0_3$, $L1_2$, and $D0_{22}$ structures in order to place our present results in context. I believe it will be particularly informative to examine other $D0_{22}$ structures, such as Pd_3V and Pt_3V, so that we may discover if the microstructural energy effects found in Ni_3V are present in other anisotropic structures.

The phase diagrams for Pt-V and Pd-V are shown in Figure 10.1; at higher temperatures, both Pd_3V and Pt_3V have a disordered fcc solution from which a $D0_{22}$–ordered structure forms at lower temperatures. Pd_3V is a particularly suitable candidate for examination because it has been the subject of recent attention from both experimentalists and theorists [3-7].

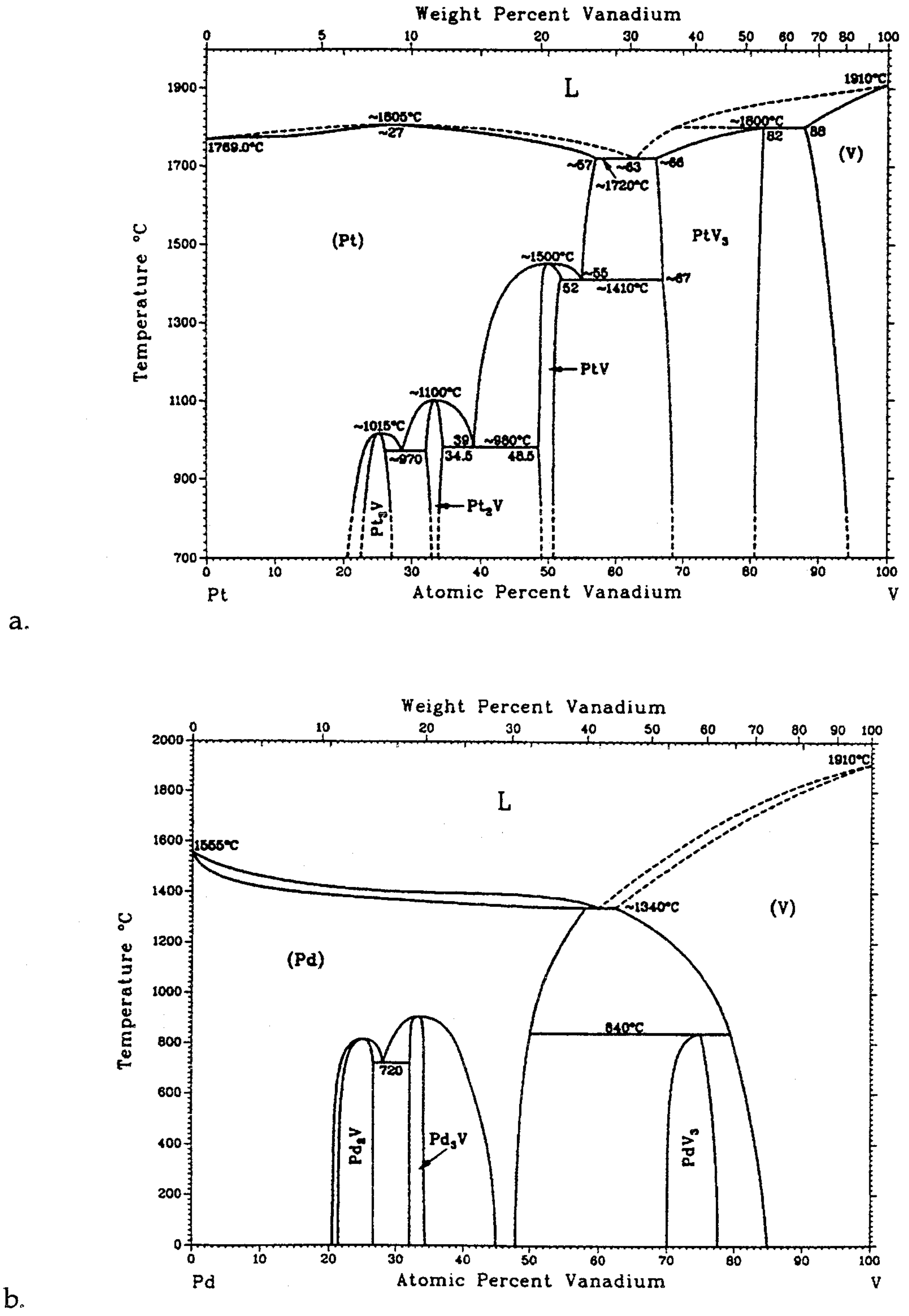

Figure 10.1 The phase diagram for Pt-V is shown in a., and the phase diagram for Pd-V is shown in b. Both diagrams are from Phase Diagrams of Binary Vanadium Alloys (ASM: Metals Park, OH, 1986).

References

[1] B. Fultz, L. Anthony, J. L. Robertson, R. M. Nicklow, S. Spooner and M. Mostoller, Phys. Rev. B Cond. Matter **52**, 3280 (1995).

[2] M. W. Pershing, G. Bambakidis, J. F. Thomas, Jr., and R. C. Bowman, Jr., J. Less-Common Metals **75**, 207 (1980).

[3] A. W. Sheikh and G. Williams, Phys. Rev. B **28**, 5307 (1983).

[4] F. Solal, R. Caudron, F. Ducastelle, A. Finel, and A. Loiseau, Phys. Rev. Lett. **58**, 2245 (1987).

[5] F. Solal, R. Caudron, and A. Finel, Physica B **156-57**, 75 (1989).

[6] C. Wolverton, A. Zunger, and Z.-W. Lu, Phys. Rev. B **49**, 16058 (1994).

[7] G. D. Garbulsky and G. Ceder, Phys. Rev. B **51**, 67 (1995).

Appendix A Detailed Experimental Procedure for Low-temperature Calorimetry

A.1 Maintenance

1. The vacuum jacket of the cryostat should be pumped out every two to three months. This should be done every time that liquid helium is used. Also, the liquid helium transfer line should be pumped out before use. This will prevent freezing of the transfer line and improve the insulating capabilities of the dewar.

2. The large O-ring at the top of the dewar should be checked regularly (twice a week during steady use) for dust and dryness and should be lubricated lightly with vacuum grease as necessary.

3. Electrical tape has been placed around the bottom of the DSC4 head to prevent it from coming into electrical contact with the side of the dewar. As a result of the extreme temperatures to which it is subjected, the tape will deteriorate over time and thus will need to be replaced every few months.

A.2 Operation with liquid nitrogen

1. In order to load the samples, the DSC4 head must first be raised from within the cryostat. First, remove all eight bolts that connect the top plate to the flange. Next, attach the three hoist connections to the three rings on the top plate of the cryostat. While raising the DSC4 assembly, be very careful to keep it vertical; try to keep it from bumping the dewar walls. Set the head on the wooden platform surrounding the cryostat and remove the

cover plate. Place the guide plate around the sample pans; this will prevent small items from falling into the wells around the sample pans. (If you should drop something into one of these wells, be very careful retrieving it--there are delicate wires leading into the bottom of the sample pan.) Carefully remove the sample pan lids with jeweler's tweezers and set aside; place the samples inside and replace the lids in their original orientation. Remove the guide plate; replace the cover plate and bolt it down. Lower the DSC4 head into the cryostat, being very careful not to jostle the samples. Replace and tighten the screws securing the top plate to the flange.

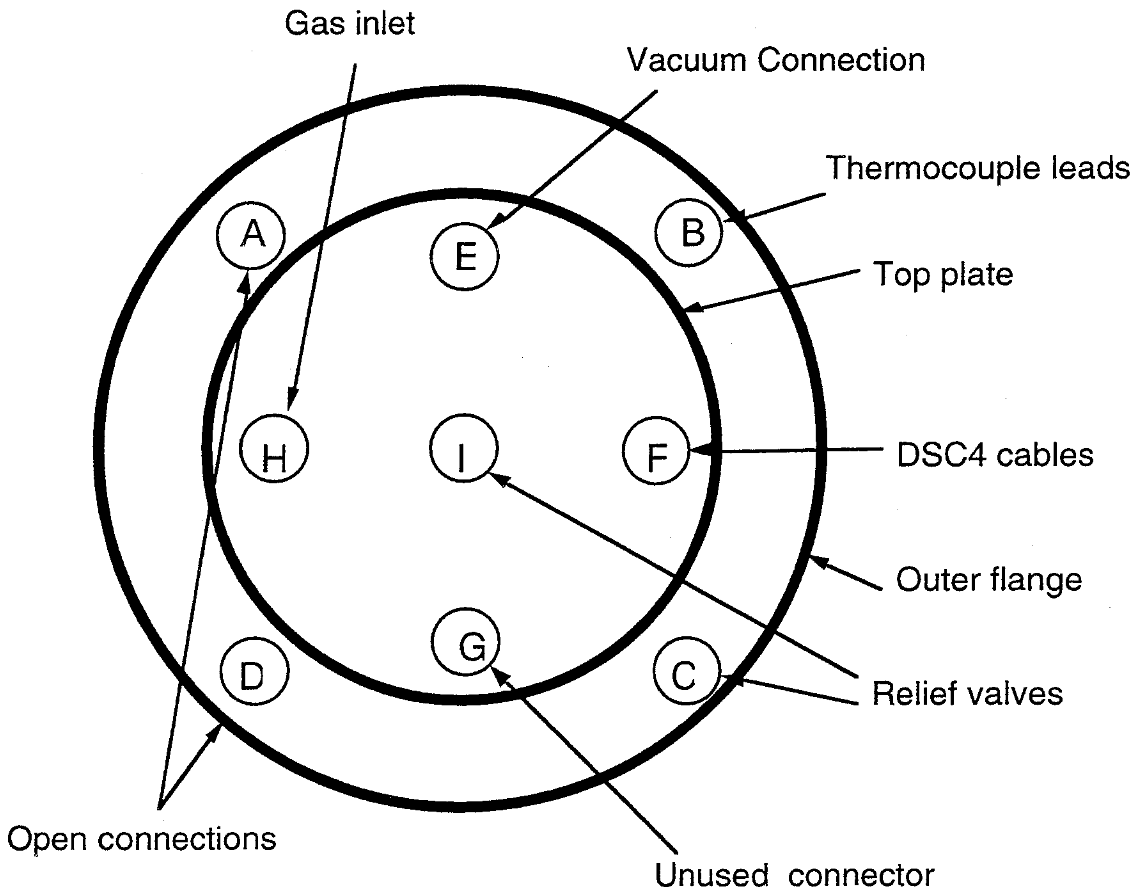

Figure A.1 Schematic of liquid helium cryostat connections.

2. After the samples have been loaded, it is necessary to purge the central chamber of the cryostat a few times with UHP helium gas in order to ensure that there are no contaminants (e.g., water) in the chamber. Connect the mechanical pump to the valve labeled "E" on Figure A.1 above. Pump until the gauge on the valve reads approximately 26. Close off the vacuum pump and open the UHP He gas flow until the gauge reads a pressure of approximately 3-5 psi. The relief valve is set for a pressure of 6 psi. Repeat this process two or three times. Leave the gas pressure set at 3 psi.

3. Connect the liquid nitrogen dewar to the inlet labeled "A" with the copper connector and start the flow of liquid nitrogen. The level of liquid nitrogen in the dewar can be roughly monitored using the thermocouples mounted inside the dewar walls. Thermocouple 1/2 is near the bottom of the dewar, thermocouple 3/4 is approximately halfway between the bottom and the lowest baffle, and thermocouple 5/6 is just below the lowest baffle. Because the handheld monitor is not calibrated correctly, the readout will display - 270 ^{o}F when the thermocouple is under liquid nitrogen. I usually let the liquid nitrogen run approximately 5 minutes after the top thermocouple reads - 270 ^{o}F. While filling the dewar with liquid nitrogen, it will be necessary to monitor the UHP He pressure in the sample chamber; try to keep it at approximately 3 psi. After transferring the liquid nitrogen, the UHP He pressure should be monitored for half an hour. The set temperature on the DSC4 controller should be set to the desired temperature (usually -180 K). Then the system should be left to equilibrate for 8 to 12 hours. During data collection, the UHP He pressure should be checked every half hour and adjusted between runs if necessary.

4. After data collection is completed, the long end of the curved copper tube should be inserted into inlet "A" and regular purity helium gas

should be used to pressurize the cryogen chamber via "D," thus driving the liquid nitrogen out the copper tube and into the small dewar which you have placed appropriately. After all the liquid has been removed, "D" should be connected to the air supply in the wall. This will warm the cryostat up to room temperature faster and also prevent condensation of liquid on the cold cryostat. Wait until the cryostat has reached room temperature (as measured by the thermocouples) before opening the sample chamber.

A.3 Operation with liquid helium

1. As discussed in A.1, the outer vacuum jackets of the cryostat and the transfer line should be pumped out before every set of experiments using liquid helium.

2. The samples should be loaded and the chamber purged in the same way as described above for liquid nitrogen work. Both the inner and outer reservoirs of the cryostat should be filled with liquid nitrogen, the set temperature should be set to -180 K, and the system should be left to equilibrate for 8 to 12 hours. If desired, you may collect a set of data with the liquid nitrogen before transferring the liquid helium.

3. Transfer the liquid nitrogen in the inner reservoir to the outer reservoir using the method described above. If there is excess liquid nitrogen after the outer reservoir is filled, transfer it to the small dewar. Force regular purity helium gas through the inner reservoir until all liquid is gone. Place a metal stopper in "A" and turn on the large roof pump. Carefully evacuate the inner reservoir, then purge with helium. Repeat this two or three times--this process should ensure that all gases (nitrogen, oxygen, etc.) except helium have been removed. Remember to turn off and purge the roof pump when

you have finished this step. Remove the line for helium gas from "D" and place a metal stopper in "D." You are now ready to transfer the liquid helium.

4. Transferring liquid helium for this arrangement is a two-person job; at certain times a third person is helpful. Attach the regular purity helium line to the pressurizing port on the liquid helium dewar. Slowly lower one end of the transfer line into the dewar; apply small amounts of pressure with the helium gas until liquid helium just starts to flow out the other end of the transfer line. At this point, the third person should quickly remove both the stoppers from "A" and "D" and the transfer line should be inserted into "A." The liquid helium level detector, which is connected to "C," can be used to tell approximately how much liquid is in the cryostat at a given time. The liquid helium should be allowed to flow until several inches are present in the reservoir, then the pressurizing gas should be turned off. After a few minutes, the liquid helium will have boiled off. Repeat this procedure three or four times, or until you are sure that the system is adequately cold. As with liquid nitrogen, you will have to monitor the UHP helium gas pressure. During the liquid helium transfer, the pressure will be very low; keep the gas flowing until after the liquid transfer is complete. After the transfer is complete, the system will start to warm up and the gas will expand; then it will be necessary to release the excess pressure at the relief valve "I." Check to make sure that this valve does not freeze during the transfer procedure. Because of the large mass of the system, you will not be able to maintain liquid helium for more than several minutes. However, by the above procedure, you can get the system sufficiently cold to collect data at -220 K. Allow the system to equilibrate for two to three hours before collecting data. I found it useful to start at as low a temperature as possible

and collect data for a few temperature intervals. Usually this data was not very good, but it seemed to "settle" the system. I then would cool it to the lowest possible temperature and collect data over the full temperature range--the second set of data would be of much higher quality.

5. After data collection is complete, the air supply in the wall should be connected to "D" and opened until the cryostat has reached room temperature. The sample chamber may then be opened.

Appendix B Crystallographic Data

All crystallographic data presented in this appendix is taken from J. L. C. Daams et al., Atlas of Crystal Structure Types for Intermetallic Phases, (Materials Park, OH: ASM International, 1991).

B.1 D0_3 Structure for Fe_3Al, p. 6814

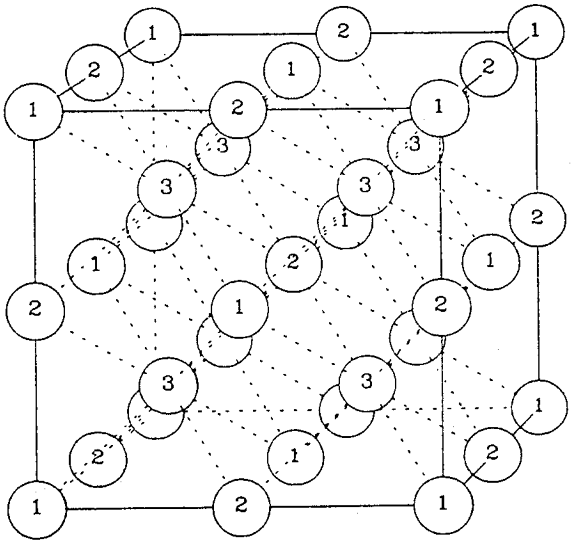

Pearson symbol	Structure type	Space group	Space group number
*cF*16	BiF_3	$Fm\bar{3}m$	225

a = .5853 nm

Number	Atom	Multiplicity Wyckoff letter		x	y	z	Occupancy
1	Bi	4	*a*	0	0	0	1
2	F1	4	*b*	1/2	1/2	1/2	1
3	F2	8	*c*	1/4	1/4	1/4	1

Reference
F. Hund et al. ZEITSCHRIFT FUER ANORGANISCHE UND ALLGEMEINE CHEMIE 1949 **258** *p198*

Remarks
Authors gave structure in space group No. 215, it should be space group No. 225

B.2 L1$_2$ Structure for Ni$_3$Al and Cu$_3$Au, p. 6402

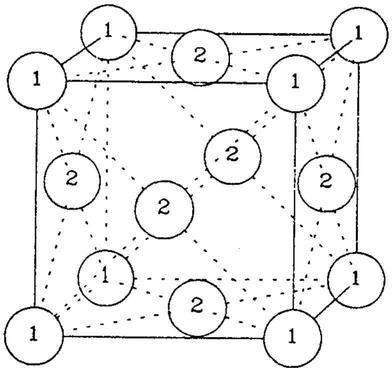

Pearson symbol	Structure type	Space group	Space group number
*cP*4	$AuCu_3$	$Pm\bar{3}m$	221

a = .3744 nm

Number	Atom	Multiplicity Wyckoff letter	x	y	z	Occupancy
1	Au	1 *a*	0	0	0	1
2	Cu	3 *c*	0	1/2	1/2	1

Reference
W. Betteridge JOURNAL OF THE INSTITUTE OF METALS 1949 **75** *p559*

B.3 D0_{22} Structure for Ni_3V, p. 4055

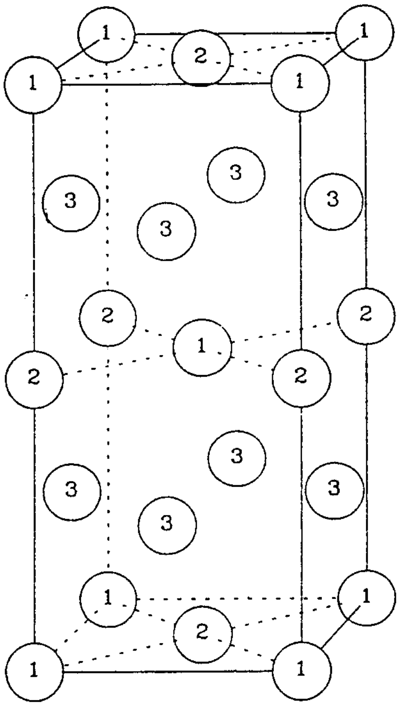

Pearson symbol	Structure type	Space group	Space group number
tI8	Al_3Ti	*I4/mmm*	139

a = .3836 nm *c* = .8579 nm

Number	Atom	Multiplicity Wyckoff letter		x	y	z	Occupancy
1	Ti	2	*a*	0	0	0	1
2	Al1	2	*b*	0	0	1/2	1
3	Al2	4	*d*	0	1/2	1/4	1

Reference
G. Brauer ZEITSCHRIFT FUER ANORGANISCHE UND ALLGEMEINE CHEMIE 1939 **242** *p1*

B.4 Ordered Hexagonal Structure for Co_3V, p. 5286

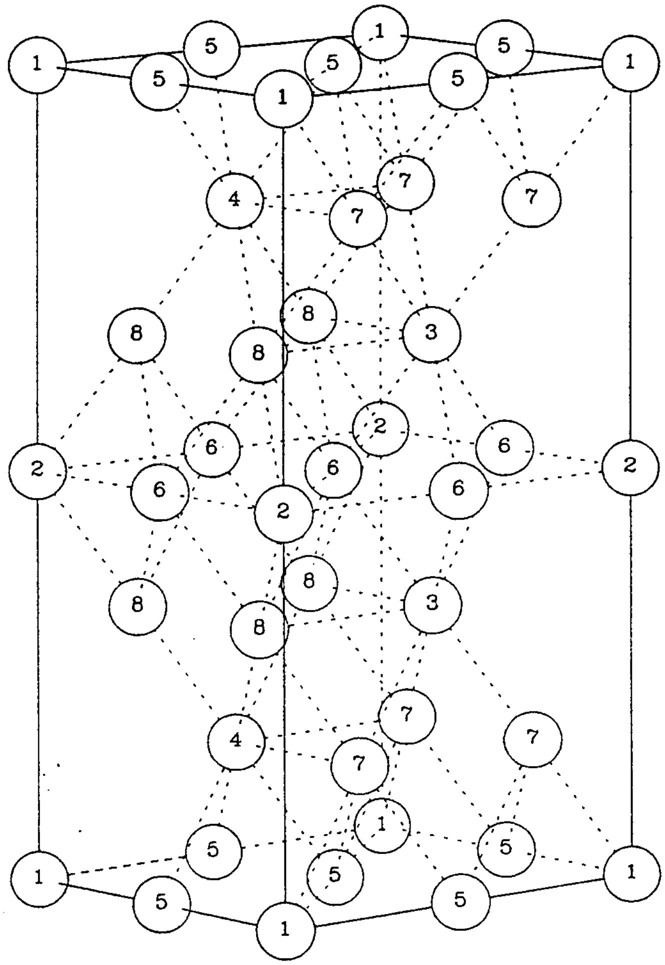

Pearson symbol	Structure type	Space group	Space group number
*hP*24	Co_3V	$P\bar{6}m2$	187

a = .5032 nm *c* = 1.2270 nm

Number	Atom	Multiplicity Wyckoff letter		x	y	z	Occupancy
1	V1	1	*a*	0	0	0	1
2	V2	1	*b*	0	0	1/2	1
3	V3	2	*h*	1/3	2/3	.333	1
4	V4	2	*i*	2/3	1/3	.167	1
5	Co1	3	*j*	.500	.500	0	1
6	Co2	3	*k*	.500	.500	1/2	1
7	Co3	6	*n*	.167	.833	.167	1
8	Co4	6	*n*	.833	.167	.333	1

Reference
S. Saito ACTA CRYSTALLOGRAPHICA 1959 **12** *p500*

Appendix C Lazy Pulverix

Lazy Pulverix is a software package which can be used to calculate both x-ray and neutron diffraction patterns. I have used it to calculate neutron diffraction patterns for Ni_3V and Co_3V. Presented below are the input and output files for the ordered states of Ni_3V and Co_3V. The crystallographic data presented in Appendix B were used to create the input files, which require information about the lattice parameters of the unit cell and the locations of all the atoms in the unit cell. Other parameters are the wavelength of the radiation and the desired range of θ angle. For more information on this method, please see F. J. Rotella,"*User Manual for Rietveld Analysis of Time-of-Flight Neutron Powder Diffraction Data at IPNS*," 1983, and R. B. Von Dreele, J. D. Jorgensen, and C. G. Windsor, J. Appl. Crystallogr. **15**, 581 (1982).

Input for Ni3V

```
TITLE Ni3V D022 order, a = 3.543A,c=7.221A Co radiation
CONDIT         1.4170  5.0 60.0 A  NE   0 1
CELL          3.543000        7.221000
SPCGRP I 4/M M M
ATOM   V   2a0        0        0             1.000
ATOM   NI  2b0        0        1/2           1.000
ATOM   NI  4d0        1/2      1/4           1.000
END
FINISH
```

Output for Ni3V

```
 INTENSITY CALCULATION FOR Ni3V D022 order, a = 3.543A,c=7.221A Co radiat

 TETRAGONAL STRUCTURE
 A=  3.54300
 C=  7.22100
 WL= 1.41700

 CALCULATION BETWEEN TL =  5.0 AND TH =  60.0 DEGREES THETA
 DIFFRACTION GEOMETRY = NEUTRON DIFFRACTION
 SPACE GROUP     GIVEN ON SPCGRP-CARD  I 4/M M M

 EQUIVALENT POINT POSITIONS

 HIGH LAUE SYMMETRY
 THERE IS  A SYMMETRY CENTRE AT THE ORIGIN
 BODY CENTRED BRAVAIS LATTICE
 CONDITIONS LIMITING POSSIBLE REFLECTIONS
 HKL WITH H+K+L=2N ONLY

 NUMBER OF ATOMS IN UNIT CELL
 ELEMENT NUMBER*  OCCUP=  NTOTAL
  V   2a     2.0*  1.000=   2.000
  NI  2b     2.0*  1.000=   2.000
  NI  4d     4.0*  1.000=   4.000
 SCATTERING FACTOR  COEFFICIENTS
 V       F=-0.041 CM-12
 NI      F= 1.030 CM-12
 NO CORRECTION FOR ANOMALOUS DISPERSION WILL BE MADE
 ATOM  POSITIONS
 ELEMENT   X/A      Y/B      Z/C     FMULT   OCCUP   BTEMP
 V   2a 0.000000 0.000000 0.000000 0.0625  1.0000  0.000
 NI  2b 0.000000 0.000000 0.500000 0.0625  1.0000  0.000
 NI  4d 0.000000 0.500000 0.250000 0.1250  1.0000  0.000
 -------------------------------------------------
 - T A B U L A R  L I S T  OF INTENSITIES FOLLOWS -
 -------------------------------------------------
 THE COLUMNS CONTAIN
 MILLER INDICES (HKL) BRAGG ANGLE (THETA) ANGLE (2THETA) OR THE DISTANCE
 D-VALUE AND/OR 1/D**2
 SQUARE OF SINE (THETA)  MULTIPLIED BY 1000 (SIN2*1000)
 INTENSITY OF A POWDER LINE, SCALED TO 1000 OR UNSCALED   (INTENSITY OR I
```

```
THE EXACT NUMBER OF COLUMNS DEPENDS ON THE INPUT VARIABLES SYMLP,NORM,I
IN THE CASE OF ANOMALOUS DISPERSION THE STRUCTURE FACTORS AND PHASE AND
FOR THE ANTIREFLECTIONS (/F+(HKL)/,/F-(HKL)/,A+(HKL),A-(HKL),B+(HKL),B-

1 H  K  L     THETA  SIN2*1000 INT.SCALED    INTENSITY UNSCALED

  0  0  2     11.32     38.51       90.9                  243.0
  1  0  1     12.87     49.62      283.8                  758.9
  1  1  0     16.43     79.98       89.5                  239.2
  1  1  2     20.13    118.48     1000.0                 2674.2
  1  0  3     20.85    126.63      116.0                  310.2
  0  0  4     23.11    154.03      196.3                  525.0
  2  0  0     23.57    159.95      379.4                 1014.6
  2  0  2     26.45    198.46       77.3                  206.6
  2  1  1     27.24    209.57      147.3                  394.0
  1  1  4     28.93    234.01       67.0                  179.2
  1  0  5     31.99    280.66       57.7                  154.2
  2  1  3     32.37    286.59      113.4                  303.3
  2  0  4     34.08    313.98      427.8                 1143.9
  2  2  0     34.44    319.91      210.8                  563.8
  0  0  6     36.06    346.57       12.2                   32.8
  2  2  2     36.78    358.42       47.8                  127.9
  3  0  1     37.44    369.53       46.8                  125.1
  3  1  0     39.22    399.89       44.3                  118.5
  1  1  6     40.78    426.54      344.4                  921.0
  3  1  2     41.46    438.39      677.2                 1811.0
  2  1  5     41.59    440.62       83.3                  222.8
  3  0  3     41.93    446.54       41.3                  110.5
  2  2  4     43.51    473.94      323.6                  865.4
  2  0  6     45.37    506.52       38.6                  103.2
  1  0  7     45.67    511.71       38.4                  102.7
  3  2  1     46.69    529.48       75.6                  202.1
  3  1  4     48.10    553.92       74.2                  198.4
  3  0  5     50.80    600.57       36.2                   96.7
  3  2  3     51.15    606.50       72.2                  193.0
  0  0  8     51.71    616.12       72.9                  194.8
  4  0  0     53.12    639.82      144.9                  387.4
  2  2  6     54.72    666.48       35.7                   95.4
  2  1  7     55.04    671.66       71.3                  190.7
  4  0  2     55.45    678.33       35.7                   95.4
  4  1  1     56.13    689.44       71.5                  191.1
  1  1  8     56.55    696.10       35.8                   95.7
  3  3  0     58.04    719.80       18.0                   48.2
  3  1  6     59.77    746.45      591.9                 1582.9
```

Input for Co3V

```
TITLE Co3V hex order, a = 5.034A, c = 12.29A neutron
CONDIT         1.5000  5.0 70.0 A  NE   0 3
CELL           5.034000        12.290000
```

```
SPCGRP P -6 M 2
ATOM   V   1a0      0       0             1.000
ATOM   V   1b0      0       1/2           1.000
ATOM   V   2h1/3    2/3     1/3           1.000
ATOM   V   2i2/3    1/3     1/6           1.000
ATOM   CO  3j1/2    1/2     0             1.000
ATOM   CO  3k1/2    1/2     1/2           1.000
ATOM   CO  6n1/6    5/6     1/6           1.000
ATOM   CO  6n5/6    1/6     1/3           1.000
END
FINISH
```

Output for Co3V

```
 INTENSITY CALCULATION FOR Co3V hex order, a = 5.034A, c = 12.29A neutron

 HEXAGONAL STRUCTURE
 A=  5.03400
 C= 12.29000
 WL= 1.50000

 CALCULATION BETWEEN TL =   5.0 AND TH =  70.0 DEGREES THETA
 DIFFRACTION GEOMETRY = NEUTRON DIFFRACTION
 SPACE GROUP     GIVEN ON SPCGRP-CARD  P -6 M 2

 EQUIVALENT POINT POSITIONS

 HIGH LAUE SYMMETRY
 THERE IS NO SYMMETRY CENTRE AT THE ORIGIN
 PRIMITIVE    BRAVAIS LATTICE
 CONDITIONS LIMITING POSSIBLE REFLECTIONS
 HKL  NONE

 NUMBER OF ATOMS IN UNIT CELL
 ELEMENT NUMBER*  OCCUP=  NTOTAL
  V    1a     1.0*  1.000=   1.000
  V    1b     1.0*  1.000=   1.000
  V    2h     2.0*  1.000=   2.000
  V    2i     2.0*  1.000=   2.000
  CO   3j     3.0*  1.000=   3.000
  CO   3k     3.0*  1.000=   3.000
  CO   6n     6.0*  1.000=   6.000
  CO   6n     6.0*  1.000=   6.000
 SCATTERING FACTOR  COEFFICIENTS
 V      F=-0.041 CM-12
 CO     F= 0.278 CM-12
 NO CORRECTION FOR ANOMALOUS DISPERSION WILL BE MADE
 ATOM  POSITIONS
 ELEMENT   X/A       Y/B       Z/C     FMULT   OCCUP   BTEMP
 V   1a 0.000000 0.000000 0.000000 0.0833  1.0000  0.000
 V   1b 0.000000 0.000000 0.500000 0.0833  1.0000  0.000
 V   2h 0.333333 0.666667 0.333333 0.1667  1.0000  0.000
 V   2i 0.666667 0.333333 0.166667 0.1667  1.0000  0.000
 CO  3j 0.500000 0.500000 0.000000 0.2500  1.0000  0.000
 CO  3k 0.500000 0.500000 0.500000 0.2500  1.0000  0.000
 CO  6n 0.166667 0.833333 0.166667 0.5000  1.0000  0.000
```

```
CO   6n 0.833333 0.166667 0.333333 0.5000  1.0000  0.000
--------------------------------------------------
- T A B U L A R   L I S T  OF INTENSITIES FOLLOWS -
--------------------------------------------------
THE COLUMNS CONTAIN
MILLER INDICES (HKL) BRAGG ANGLE (THETA) ANGLE (2THETA) OR THE DISTAN
D-VALUE AND/OR 1/D**2
SQUARE OF SINE (THETA)  MULTIPLIED BY 1000 (SIN2*1000)
INTENSITY OF A POWDER LINE, SCALED TO 1000 OR UNSCALED    (INTENSITY O
STRUCTURE FACTOR  (/F(HKL)/)
REAL AND IMAGINARY PART OF STRUCTURE FACTOR (A(HKL),B(HKL))
PHASE ANGLE (PHA.ANG.)
MULTIPLICITY OF THE POWDER LINE (MULT)
LORENTZ-POLARISATION FACTOR FOR X RAY DIFFRACTION, OR LORENTZ FACTOR

THE EXACT NUMBER OF COLUMNS DEPENDS ON THE INPUT VARIABLES SYMLP,NORM
IN THE CASE OF ANOMALOUS DISPERSION THE STRUCTURE FACTORS AND PHASE A
FOR THE ANTIREFLECTIONS (/F+(HKL)/,/F-(HKL)/,A+(HKL),A-(HKL),B+(HKL),:

1 H  K  L     THETA  SIN2*1000 INT.SCALED   INTENSITY UNSCALED

  0  0  2      7.01     14.90      0.0                  0.0
  1  0  0      9.91     29.60      0.0                  0.0
  1  0  1     10.52     33.32    143.9                111.8
  0  0  3     10.55     33.52      0.0                  0.0
  1  0  2     12.18     44.49    325.2                252.7
  0  0  4     14.13     59.59      0.0                  0.0
  1  0  3     14.55     63.11    308.7                239.9
  1  1  0     17.34     88.79    333.8                259.3
  1  0  4     17.38     89.18    166.2                129.1
  1  1  1     17.71     92.51      0.0                  0.0
  0  0  5     17.77     93.10      0.0                  0.0
  1  1  2     18.78    103.68      0.0                  0.0
  2  0  0     20.13    118.38      0.0                  0.0
  2  0  1     20.45    122.11    254.7                197.9
  1  1  3     20.47    122.31      0.0                  0.0
  1  0  5     20.50    122.70     41.0                 31.9
  2  0  2     21.41    133.28    704.5                547.3
  0  0  6     21.48    134.07    467.1                362.9
  1  1  4     22.66    148.37      0.0                  0.0
  2  0  3     22.94    151.90    833.1                647.3
  1  0  6     23.86    163.66      0.0                  0.0
  2  0  4     24.95    177.97    541.7                420.9
  1  1  5     25.24    181.89      0.0                  0.0
  0  0  7     25.29    182.48      0.0                  0.0
  2  1  0     27.08    207.17      0.0                  0.0
  2  1  1     27.34    210.90     50.3                 39.1
  2  0  5     27.38    211.49    155.2                120.5
  1  0  7     27.42    212.08     25.0                 19.5
  2  1  2     28.11    222.07    144.4                112.2
  1  1  6     28.17    222.86    288.0                223.8
  0  0  8     29.22    238.34      0.0                  0.0
  2  1  3     29.38    240.69    179.8                139.7
  2  0  6     30.16    252.45      0.0                  0.0
  3  0  0     31.07    266.37    124.0                 96.3
  2  1  4     31.10    266.76    123.8                 96.2
```

```
  1  0  8      31.17     267.94      61.7                    47.9
  3  0  1      31.31     270.09       0.0                     0.0
  1  1  7      31.39     271.27       0.0                     0.0
  3  0  2      32.03     281.26       0.0                     0.0
  3  0  3      33.20     299.88       0.0                     0.0
  2  1  5      33.23     300.27      37.5                    29.2
  2  0  7      33.26     300.86     115.8                    90.0
  0  0  9      33.31     301.65       0.0                     0.0
  3  0  4      34.81     325.95       0.0                     0.0
  1  1  8      34.89     327.13       0.0                     0.0
  1  0  9      35.14     331.25      69.6                    54.1
  2  1  6      35.74     341.24       0.0                     0.0
  2  2  0      36.58     355.15     613.0                   476.3
  2  0  8      36.67     356.73     305.5                   237.4
  2  2  1      36.80     358.88       0.0                     0.0
  3  0  5      36.84     359.47       0.0                     0.0
  2  2  2      37.47     370.05       0.0                     0.0
  0  0 10      37.61     372.41       0.0                     0.0
  3  1  0      38.34     384.75       0.0                     0.0
  3  1  1      38.56     388.47      31.0                    24.1
  2  2  3      38.57     388.67       0.0                     0.0
  2  1  7      38.63     389.65      31.0                    24.1

1 H  K  L      THETA   SIN2*1000 INT.SCALED   INTENSITY UNSCALED

  1  1  9      38.67     390.44       0.0                     0.0
  3  1  2      39.21     399.65      91.4                    71.0
  3  0  6      39.26     400.43     182.5                   141.8
  1  0 10      39.35     402.00      45.5                    35.4
  2  2  4      40.09     414.74       0.0                     0.0
  3  1  3      40.30     418.27     118.2                    91.9
  2  0  9      40.40     420.03     364.3                   283.1
  3  1  4      41.80     444.33      85.4                    66.4
  2  1  8      41.87     445.51      85.3                    66.3
  2  2  5      42.03     448.26       0.0                     0.0
  3  0  7      42.06     448.84       0.0                     0.0
  0  0 11      42.17     450.61       0.0                     0.0
  1  1 10      42.77     461.20       0.0                     0.0
  4  0  0      43.48     473.54       0.0                     0.0
  4  0  1      43.70     477.26      84.4                    65.6
  3  1  5      43.73     477.85      27.3                    21.2
  1  0 11      43.87     480.21      13.6                    10.6
  4  0  2      44.34     488.43     250.2                   194.4
  2  2  6      44.38     489.22    1000.0                   777.0
  2  0 10      44.47     490.79     249.6                   193.9
  3  0  8      45.27     504.71       0.0                     0.0
  4  0  3      45.40     507.05     327.4                   254.4
  2  1  9      45.51     508.82     105.8                    82.2
  3  1  6      46.08     518.82       0.0                     0.0
  4  0  4      46.90     533.12     240.0                   186.4
  0  0 12      47.08     536.27     159.6                   124.0
  2  2  7      47.16     537.63       0.0                     0.0
  1  1 11      47.26     539.40       0.0                     0.0
  3  2  0      48.58     562.33       0.0                     0.0
  1  0 12      48.78     565.86       0.0                     0.0
  3  2  1      48.80     566.05      25.3                    19.6
```

```
   4  0  5     48.83    566.64     78.1              60.7
   3  1  7     48.86    567.23     25.3              19.6
   3  0  9     48.91    568.02      0.0               0.0
   2  0 11     48.97    569.00     78.0              60.6
   3  2  2     49.44    577.22     75.4              58.6
   2  1 10     49.58    579.58     75.3              58.5
   2  2  8     50.39    593.49      0.0               0.0
   3  2  3     50.53    595.84     99.6              77.4
   4  0  6     51.21    607.60      0.0               0.0
   4  1  0     52.03    621.52    148.0             115.0
   3  2  4     52.06    621.91     74.0              57.5
   3  1  8     52.13    623.09     74.0              57.5
   1  1 12     52.24    625.06    147.8             114.9
   4  1  1     52.25    625.24      0.0               0.0
   0  0 13     52.50    629.37      0.0               0.0
   4  1  2     52.92    636.41      0.0               0.0
   3  0 10     53.06    638.77      0.0               0.0
   2  0 12     54.01    654.65      0.0               0.0
   4  1  3     54.03    655.04      0.0               0.0
   3  2  5     54.06    655.43     24.5              19.0
   4  0  7     54.09    656.02     75.7              58.8
   2  2  9     54.14    656.80      0.0               0.0
   2  1 11     54.20    657.79     24.5              19.0
   1  0 13     54.27    658.97     12.3               9.5
   4  1  4     55.62    681.10      0.0               0.0
   3  1  9     55.94    686.40     98.1              76.2

1  H  K  L     THETA   SIN2*1000  INT.SCALED   INTENSITY UNSCALED

   3  2  6     56.56    696.39      0.0               0.0
   4  0  8     57.54    711.88    228.8             177.7
   4  1  5     57.71    714.62      0.0               0.0
   3  0 11     57.86    716.98      0.0               0.0
   1  1 13     57.93    718.16      0.0               0.0
   2  2 10     58.54    727.56      0.0               0.0
   0  0 14     58.69    729.92      0.0               0.0
   5  0  0     59.34    739.90      0.0               0.0
   2  1 12     59.57    743.44      0.0               0.0
   5  0  1     59.58    743.63     12.5               9.7
   3  2  7     59.66    744.81     25.1              19.5
   2  0 13     59.85    747.75     77.6              60.3
   5  0  2     60.32    754.80     37.8              29.4
   4  1  6     60.37    755.59    302.9             235.4
   3  1 10     60.48    757.16     75.8              58.9
   1  0 14     60.63    759.52     38.0              29.5
   5  0  3     61.58    773.42     51.2              39.8
   4  0  9     61.70    775.19    317.1             246.4
   3  3  0     63.37    799.10     79.0              61.4
   5  0  4     63.40    799.49     39.5              30.7
   3  2  8     63.48    800.67     79.1              61.5
   3  0 12     63.62    802.63    158.7             123.3
   3  3  1     63.64    802.82      0.0               0.0
   4  1  7     63.72    804.00      0.0               0.0
   2  2 11     63.85    805.77      0.0               0.0
   3  3  2     64.45    813.99      0.0               0.0
   1  1 14     64.80    818.71      0.0               0.0
```

4	2	0	65.55	828.69	0.0	0.0
4	2	1	65.83	832.42	171.0	132.9
3	3	3	65.85	832.61	0.0	0.0
5	0	5	65.88	833.01	13.9	10.8
3	1	11	66.06	835.36	27.8	21.6
2	1	13	66.15	836.54	27.9	21.7
0	0	15	66.26	837.92	0.0	0.0
4	2	2	66.70	843.59	524.0	407.1
4	0	10	66.89	845.95	263.3	204.5
2	0	14	67.08	848.30	264.6	205.6
3	3	4	67.92	858.68	0.0	0.0
4	1	8	68.02	859.86	0.0	0.0
4	2	3	68.21	862.21	728.3	565.9
3	2	9	68.36	863.98	118.4	92.0
1	0	15	68.65	867.51	59.7	46.4
5	0	6	69.21	873.97	0.0	0.0